Developing a platform for Low Temperature Superconducting Electromechanics

by

Sean R McClure

A thesis submitted in partial fulfillment of the requirements for the degree of

Master of Science

Department of Department of Physics
University of Alberta

Abstract

This thesis lays out the work required to design and create a platform for cryogenically compatible testing of on-chip microwave resonators, intended as a platform for quantum-limited electromechanical torque sensing. We have created a platform with less than 8 dB loss across an operating range of up to 12 GHz, the widest band we can measure with current equipment. We then used this platform to measure on-chip resonators with quality factors greater than $50,000$, competitive with state-of-the-art devices for which the development and fabrication is also described. We also lay out the necessary theory to design high-quality electromechanical sensors and describe a straightforward path to their creation.

Preface

This thesis is an original work by 'Sean McClure'. No part of this thesis has been previously published.

"How is this even science, without the possibility of death?"

-GLaDOS

Acknowledgements

I never would have even begun my master's program without the support and encouragement of John P. Davis, so on his head be it. I also wanted to thank everyone else from the Davis lab including Tommy Clark, Brad Hauer, Hugh Ramp, Clinton Potts, Greg Popowich, James Chaulk, Alex Shook, Emil Varga, Vaisakh Vadakkumbatt, Matt Rudd, Scott Agnew, Myles Ruether, Elham Zohari, Emil Varga's lemon tree, and everyone else I have missed.

I'd also like to extend personal thanks to the staff at the nanoFAB including Aaron Hryciw, Gustavo de Oliveira Luiz, Stephanie Bozic, and Scott Munro. Additional thanks to Rick and Omni Circuit Boards for providing sample boards that proved invaluable in developing this project.

I'd also like to especially thank Nikkita Raun for the poking, prodding, and unceasing support. This would honestly not have been possible without them.

Table of Contents

List of Figures

List of Symbols

Constants

μ_0	Vacuum permeability.	$1.25663706212(19) \times 10^6 \mathrm{H/m}$
c	Speed of light in a vacuum inertial system.	$299,792,458\, m/s$
k_B	Boltzmann's constant.	$1.38064852 \times 10^{-23} \mathrm{m^2 kgs^{-2} K^{-1}}$
h	Planck's Constant	$6.62607015 \times 10^{-34}$ J Hz^1
h	Reduced Planck's Constant	$1.054571817... \times 10^{34}$ J s

Latin

$\bar{S}_{\Phi\Phi}$	Flux spectral density.
$\bar{S}_{V_{\mathrm{in}}V_{\mathrm{in}}}$	Spectral density of input voltage.
γ	Propagation constant of a transmission line.
Γ_m	Mechanical resonator loss rate.
$\hat{a}^\dagger, \hat{a}$	Photon creation and annihilation operators.
$\hat{b}^\dagger, \hat{b}$	Phonon creation and annihilation operators.
κ	Electromagnetic resonator loss rate.
λ_L	London penetration depth of a superconductor.
ω	Angular frequency of the cavity drive.
ω_0	Angular resonance frequency of electromagnetic resonator.
ω_m	Angular resonance frequency of mechanical resonator.

Φ Branch flux of a resonator.

σ_1 The real component of the Mattis-Bardeen Conductivity as seen in eq. (2.107).

σ_2 The imaginary component of the Mattis-Bardeen Conductivity as seen in eq. (2.107).

σ_n Normal conductance of a metal.

$\tilde{K}$ Specified ratio of elliptic integrals of the first kind.

ε_r Dielectric constant of the substrate.

ε_{eff} Effective dielectric constant of a transmission line.

a Width of the center pin of a coplanar waveguide as shown in fig. 2.3.

b Total width of the center pin of a coplanar waveguide as shown in fig. 2.3.

C Capacitance of a circuit.

C_ℓ Per unit length capacitance of a transmission line.

E Elastic Constant (Young's Modulus).

G Conductance of a circuit.

I Current.

K Elliptic integral of the first kind.

k_n, n=1,2,3... Specified constant for elliptic integral.

L Inductance of a circuit.

L_ℓ Per unit length inductance of a transmission line.

n_n/n_s Fraction of normally conducting charge carriers compared to superconducting charge carriers.

Q Quality factor of a resonator.

q Charge.

R Resistance of a circuit.

R_ℓ	Per unit length resistance of a transmission line.	
s	Width of the gap between the center pin and the ground of a coplanar waveguide as shown in fig. 2.3.	
T	Temperature.	
T_C	Critical temperature of a superconductor.	
t_d	Thickness of metal in coplanar waveguide.	Meters.
V	Voltage.	
V_{in}	Input voltage of a system.	
Y_0	Characteristic Admittance of a transmission line.	
z	Distance along a transmission line from input at $z = 0$.	Meters
Z_0	Characteristic Impedance of a transmission line.	
Z_∞	Impedance of a line as seen at infinite distance away.	
t	Time.	Seconds

Abbreviations

BCS Bardeen, Cooper, and Schrieffer.

BOE Buffered Oxide Etch.

CPW Coplanar Waveguide.

DUT Device Under Test.

ENIG Electroless Nickel Immersion Gold.

FEM Finite-Element Modelling.

FESEM Field Emission Scanning Electron Microscope.

HEMT High-Electron-Mobility Transistor.

HF Acid Hydrofluoric Acid.

HFSS High Frequency Simulation Suite.

JPA Josephson Parametric Amplifier.

LC Inductance(L) and Capacitance (C), in reference to a resonator.

MB Mattis-Bardeen.

RF Radio Frequency.

SEM Scanning Electron Microscope.

SOP Standard Operating Procedure.

SQL Standard Quantum Limit.

TL Transmission Line.

Chapter 1

Introduction

1.1 Motivation

Since the turn of the millennium, nanomechanical resonators have been used as increasingly sensitive detectors of small masses [1], forces [2], and motion [3–6]. These devices have approached in sensitivity a proposed fundamental limit of measurement, the "Standard Quantum Limit" (SQL); while several groups using state-of-the-art measurement techniques have approached quantum-limited measurement [7, 8] it remains elusive.

Put simply, the standard quantum limit arises because of the Heisenberg uncertainty principle formulated by Werner Heisenberg in 1927. This states that measurement of an object's momentum and position cannot be arbitrarily precise [9]. The limit on the simultaneous measurement of canonical position x and its conjugate momentum p is

$$\Delta x \Delta p \geq \frac{\hbar}{2}. \tag{1.1}$$

This is the result of the fundamentally wave-like nature of matter and reflects nothing about the measurement itself. Meanwhile, gedankenexperiments such as Heisenberg's microscope [10] or Von Neumann's Doppler meter [11] give rise to physical interactions within measurements that lead to an uncertainty

$$\Delta x_{\text{perturb}}\, \Delta p_{\text{measure}} \geq \frac{\hbar}{2}. \tag{1.2}$$

Despite this uncertainty arising solely from the method of measurement, they take the same form. That both principles take the same form is no accident—they are two sides of the same "quantum" coin. The measurement apparatus theorized is itself subject to the uncertainty relation eq. (1.1), and so consequently cannot measure beyond that limit of eq. (1.2). Meanwhile, if one were to attempt to prepare a state with initial conditions that violate the uncertainty principle in eq. (1.1), one is prevented from doing so by eq. (1.2).

Any kind of microwave interferometer can in theory measure displacement, without momentum, to arbitrary accuracy by encoding the position in the measurement of the phase of the cavity field [12], however, life is not so easy.

If one tries to measure the phase shift of the field cavity using N photons, the fundamental relationship between photon number and phase yields what we call "shot noise", which limits the precision of $\delta\theta = 1/(2\sqrt{N})$. This limit implies that measurement can still be arbitrarily precise by using arbitrarily many photons.

However, when measuring the phase to decode the position $x(t)$, the noisy signal needs to be integrated over many oscillations of the field to "average out" the noise and pinpoint the signal. But we cannot follow the trajectory $x(t)$ without knowing the momentum of x; each photon separately gives a small "kick" of momentum to the measured object growing with $\sqrt{N}$. We can show these will cancel the improvements in shot noise at some crossover value.

In practice, this crossover value occurs for a resonator that oscillates at ω_m when both shot noise (or imprecision noise) and this measurement induced noise (or "backaction") noise contribute $\hbar\omega_m/4$. This total noise energy of $\hbar\omega_m/2$ is the standard quantum limit. As the backaction noise can be reduced by accurately measuring at lower powers, we look to decrease imprecision, or shot noise, within the system. To do this we should design low-mass, high-quality factor mechanical oscillators strongly coupled to high-quality microwave resonators.

Unlike optical resonators which are subject to heating from the higher energy photons

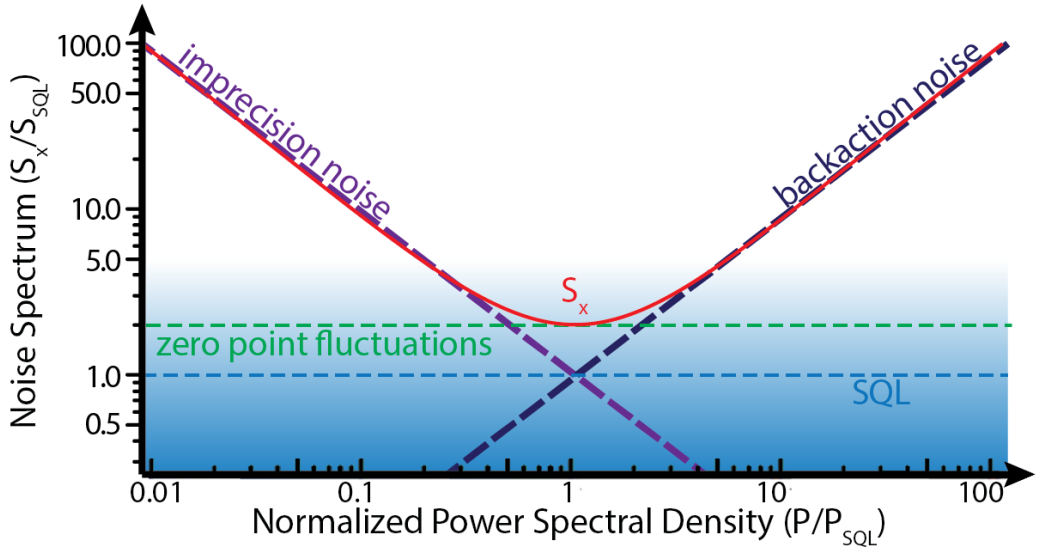

Figure 1.1: The total measured spectral density S_x normalized to S_{SQL}, the standard quantum limit. It is comprised of three contributions, the imprecision noise, backaction noise, and the zero-point fluctuations of the oscillator being measured.

[13, 14], microwave interferometers add minimal heating to the mechanical elements [15, 16]. At cryogenic temperatures, they can leverage superconductivity to decrease heating and increase the quality factor [17, 18]. They can be operated in their thermal ground state [19], and can be operated with quantum-limited amplifiers [12].

Thus microwave electromechanical systems represent a clear path to performing quantum-limited measurement of macroscopic mechanical objects, which present fundamental tests of modern quantum theory [20].

1.2 Thesis Objectives

In this thesis, we have set out to develop the methods and infrastructure to perform quantum-limited measurements using electromechanical resonators. Our lab previously had no experience working with these on-chip devices, and so the bulk of this work is spent developing techniques required to create a microwave circuit of fine enough quality for this application, which is competitive within the field. We have set out a complete framework to take the produced microwave resonators, which have quality factors competitive with modern published work,and integrate them with me-

chanical resonators of which our group has some experience fabricating. This will provide any future students with a turnkey platform for testing.

1.3 Thesis Outline

Chapter 2 discusses how to implement a cavity electromechanical system using a microwave circuit and a nanomechanical resonator. We will discuss both classical and quantum Langevin descriptions of the system. We will then use those formulations to derive the quantum Langevin equations for a cavity electromechanical system. We also discuss how superconducting thin films can be modeled in Finite Element Modelling (FEM) software in the GHz frequency regime.

Chapter 3 will discuss the work done in the design and simulation of the platforms created to house the on-chip devices. These platforms allow them to be mounted onto a dilution refrigerator and electrically accessed. Simulations of the cavity throughput in each platform are created using FEM software such as COMSOL and Ansys HFSS, which in the next chapter will also be used to simulate the electrical response of the on-chip electrical resonators.

Chapter 4 will discuss the design, simulation, and nanofabrication of these on-chip devices.

Chapter 5 will discuss our results and measurements. In this, we will see the evolution of the project, as well as discuss the performance of various tested designs.

Chapter 6 will then discuss our conclusions at the end of the project, as well as the future work that will need to be done to add mechanical elements to the platform designed here, allowing for electromechanical sensing.

Chapter 2

Background: Theory of electromechanical resonators

This chapter explains how we can create electrical circuits which resonate in the microwave regime, as well as how we engineer them to be sensitive to mechanical motion to enable sensing. We first describe the circuits classically as microwave resonators, including the particular geometries used in this work. We also examine the changes when a resonator superconducts, and how this affects the system. We then describe how the mechanical resonator couples to the circuit, and how the mechanical element perturbing the field allows for sensing of mechanical motion. Because these systems are being measured at cryogenic temperatures ($T \approx 60$ mK), below the energy scale of the electrical resonance ($E/\hbar \approx 8$ GHz) we then must attend to how these systems can be quantized to fully describe their behaviour.

We can then explore how these resonators can be treated using the framework of quantum optics and optomechanics to understand how these systems compare to sensitive optomechanical sensors, and what effects govern their operations.

While the experimental component of this work never produced mechanical elements coupled to the produced microwave cavities, it is hoped the inclusion of this theory will provide a robust resource for future students continuing the project.

2.1 Theory of Microwave resonators

When first beginning to describe resonant circuits, the simplest case is that of the LCR circuit. However, as one approaches the microwave (GHz) regime, physical elements of the circuit will begin to extend over an appreciable fraction of the electrical wavelength. When these elements extend along a significant fraction of the electrical wavelength without extending in the transverse plane (are effectively one dimensional) we can approximate the circuit as a series of LCR circuits with electrical properties given by the geometry along an incremental distance of the line. In order to measure these circuits, we must then discuss how one can couple signals into and out of the system using input and output transmission lines. These discussions borrow heavily from the excellent work Microwave Engineering by David Pozar [21], with the discussions on superconductivity supplemented primarily by Circuit Cavity Electromechanics in the Quantum Regime by C. U. Lei [18].

2.1.1 LCR Resonators

The simplest microwave resonator is the LCR resonator, so-called because its properties are determined by its inductance L, its capacitance C, and its resistance R. One can write an equation of motion for the charge on the capacitor, for a case where the currents sum to zero, and all voltages are equal, i.e. a parallel LCR oscillator as shown in fig. 2.1 as [21]

$$\frac{d^2q}{dt^2} - \frac{1}{RC}\frac{dq}{dt} + \frac{q}{LC} = 0, \tag{2.1}$$

where the charge is given by q. Solving this equation gives us

$$q(t) = q_0 \exp\left[i\left(\omega_0 + i\frac{\kappa}{2}\right)t + \Phi\right] \tag{2.2}$$

with oscillation frequency $\omega_0 = 1/\sqrt{LC}$ and a decay rate of $\kappa = 2/RC$. The circuit is resonant when equal amounts of energy are stored in the electric and magnetic field, and thus tuning either the inductance storing the magnetic field or the capacitance

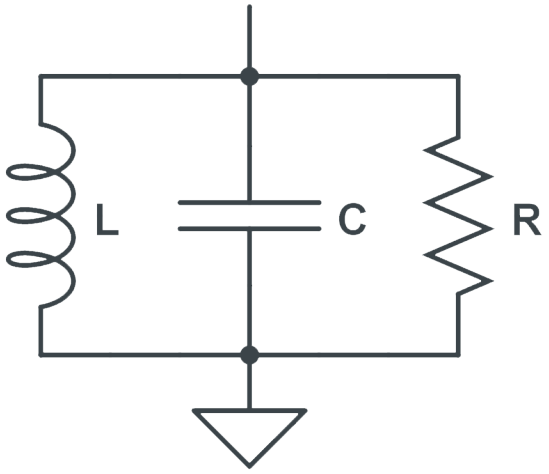

Figure 2.1: Circuit diagram illustrating an LCR resonator with inductance L, capacitance C, and resistance R. In this system, the potential of the capacitor and the current in the inductor are linked, both by Lenz's law and the current drawing charge from the capacitor.

storing the electric field will change the resonant frequency of the circuit.

When describing this system we use what is referred to as impedance, $Z(\omega)$ or the admittance, $Y(\omega) = 1/Z(\omega)$. For the parallel LCR resonator, we have an impedance of

$$Z_{\mathrm{LCR}}(\omega) = \left(i\omega C + \frac{1}{i\omega L} + \frac{1}{R} \right)^{-1}. \tag{2.3}$$

Interestingly, at the resonant frequency the imaginary component of the impedance goes to zero. If we probe at a frequency ω near the resonance frequency ω_0, $\delta\omega = \omega - \omega_0$ and if we expand to first order in $\delta\omega$, taking $\omega^2 - \omega_0^2 \sim 2\omega\,(\omega - \omega_0)$, we find

$$Z_{\mathrm{LCR}}(\omega) = \frac{R}{1 + 2iQ\delta\omega/\omega_0}. \tag{2.4}$$

This introduces a new quantity, the quality factor $Q = \omega_0 RC = \omega_0/\gamma$, which is a dimensionless quantity that tells us the ratio of energy stored in the resonator compared to loss each cycle. Alternatively, Q can be thought of as the number of oscillations over which the excitation in the cavity decays, $2/\kappa = RC$, before the system comes to an equilibrium.

Somewhat counterintuitively, larger resistances lead to higher Q[1]. When you consider the layout of the RLC circuit in fig. 2.1, the resistor and the rest of the system are in parallel; thus higher resistance drives more current through the (ideally) lossless inductor and capacitor as told to us by Ohm's law. Then in the limit $R \to \infty$ gives us the lossless case

$$Z_{\mathrm{LC}}(\omega) = \frac{1}{2iC\,(\omega - \omega_0)}. \tag{2.5}$$

2.1.2 Quantization of Electrical Resonators

In the previous section, the classical formulation of an LCR resonator was shown. However, this system can also be described quantum mechanically using the language of second quantization, with operators given in terms of electrical characteristics. As we will see it is a version of the harmonic oscillator, where energy oscillates from the electric to the magnetic field.

Because the capacitor and inductor are in parallel, they have an equivalent electric potential across them, which can be expressed both in terms of the capacitance C and the inductance L as

$$V = \frac{q}{C} = L\frac{\delta I}{\delta t} \tag{2.6}$$

where q is the charge on the capacitor and $\frac{\delta I}{\delta t}$ is the time derivative of the current through the inductor. Because the positive current direction is chosen as being opposite to the positive voltage direction, we also have that $I = -\frac{\delta Q}{\delta t}$. The total energy stored in such a resonant LC circuit is then the sum of the energies stored in the inductor and capacitor.

The energy stored within the inductor is

$$E_L = \int_{-\infty}^{t} IV(t')dt' = \int_{-\infty}^{t} LI\frac{\delta I}{\delta t}dt' = \frac{LI^2}{2}, \tag{2.7}$$

where the integral uses the condition that at time $t = -\infty$ all currents are zero. We can also consider writing the energy stored in the capacitor in terms of the charges,

[1]This isn't referring to the resistance of the wires in fig. 2.1, those are assumed to be lossless. Rather it is only the resistance of the lumped resistor in the model which has resistance R.

$(1/2)CV^2 = (Q^2/2C)$. We then have that

$$E = \frac{1}{2}LI^2 + \frac{1}{2}CV^2. \tag{2.8}$$

We can then look at defining a Hamiltonian for the system in terms of generalized position q_i and momentum p_i, which are said to be canonical if

$$\frac{\partial H}{\partial q_i} = -\dot{p}_i, \qquad \frac{\partial H}{\partial p_i} = \dot{q}_i. \tag{2.9}$$

We also define a term called the branch flux, $\Phi = LI$. We can then write out our Hamiltonian,

$$H = U_L + U_C = \frac{\Phi^2}{2L} + \frac{q^2}{2C}. \tag{2.10}$$

The reason for writing the Hamiltonian in these terms becomes clear as we find that this branch flux and charge are the canonical position and momentum,

$$\frac{\partial H}{\partial \Phi} = \frac{\Phi}{L} = I = -\dot{q}, \qquad \frac{\partial H}{\partial q} = \frac{q}{C} = L\dot{I} = \dot{\Phi}. \tag{2.11}$$

Because Φ and q are canonically conjugate, we can convert them into quantum mechanical operators $\hat{\Phi}$ and $\hat{q}$ which will obey the commutation relation

$$[\hat{\Phi}, \hat{q}] = i\hbar. \tag{2.12}$$

This Hamiltonian can then be seen as simply a mapping of the quantum harmonic oscillator,

$$H = \frac{\hat{p}^2}{2m} + m\omega^2\hat{x}^2, \tag{2.13}$$

where we consider the mapping $\hat{p} \to \hat{q}$, $\hat{x} \to \hat{\Phi}$, $C \to m$, and $\frac{1}{\sqrt{LC}} \to \omega$.
The harmonic oscillator Hamiltonian can be written in terms of dimensionless creation and annihilation operators

$$H = \hbar\omega(\hat{a}^\dagger\hat{a} + 1/2) \tag{2.14}$$

where the photon annihilation operator for a circuit of characteristic impedance $Z_0 = \sqrt{L/C}$ is given by

$$\hat{a} = \frac{1}{\sqrt{2\hbar Z_0}}\left(\Phi + iZ_0 q\right). \tag{2.15}$$

Similar to the discussion of optical systems in second quantization, evaluating $\langle \hat{a}^\dagger | \hat{a} \rangle$ gives the number of excitations n. This then tells us the system has energy $E = (n + 1/2)\hbar\omega$ as expected.

We can then express charge and flux in terms of the annihilation and creation operators as

$$q = i\sqrt{\frac{\hbar}{2Z_0}}\left(a^\dagger - a\right), \tag{2.16}$$

and

$$\Phi = \sqrt{\frac{\hbar Z_0}{2}}\left(a + a^\dagger\right). \tag{2.17}$$

2.1.3 Transmission Line Theory

Rather than modeling the circuit as one with discrete lumped elements, a transmission line can better be modeled as a series of infinitesimally small lumped elements that have the same impedance as the line. In this formalism, the impedance of a small section of line with resistance R_ℓ, inductance L_ℓ, conductance G_ℓ, and capacitance C_ℓ per unit length is

$$Z_0 = \sqrt{\frac{R_\ell - i\omega L_\ell}{G_\ell - i\omega C_\ell}}. \tag{2.18}$$

One can think of the conductance as the flow of leakage current between the conductors (and the ground). Conductance between the conductors arises because any applied alternating voltage will cause a current flow, or "leakage current", in the dielectric medium due to material imperfections. Similarly, the resistance is generally associated with conductor loss in non-superconducting systems.

Signals travelling along the transmission line act as waves with a propagation coefficient given by

$$\gamma = \sqrt{(R_\ell - i\omega L_\ell)\,(G_\ell - i\omega C_\ell)}, \tag{2.19}$$

with voltage $V(x)$ and current $I(x)$ at a distance x along the line given by

$$V(x) = V_{(+)}e^{-\gamma x} + V_{(-)}e^{+\gamma x}, \tag{2.20}$$

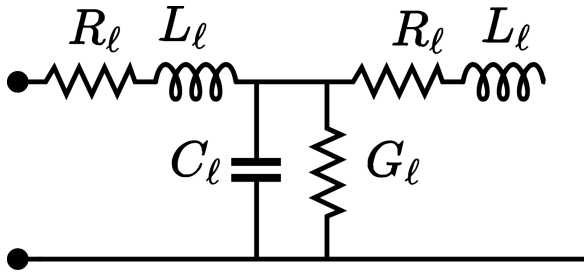

Figure 2.2: Transmission lines can be modeled as an infinite series of resistors with resistance R_ℓ and inductors with inductance L_ℓ, interspersed with parallel capacitors with capacitance C_ℓ and resistors in parallel with resistance G_ℓ.

$$I(x) = \frac{1}{Z_0}\left(V_{(+)}e^{-\gamma x} - V_{(-)}e^{+\gamma x}\right), \tag{2.21}$$

and constants $V_{(\pm)}$ given by boundary conditions. Then the changing phase of the wave is described by $\beta = \mathrm{Im}(\gamma)$, with a signal at frequency ω having phase velocity $v = \omega/\beta$ and the attenuation of the signal along the line being described by $\alpha = \mathrm{Re}(\gamma)$. It is also worth considering the effect of terminating a line with a load impedance $Z_L \neq Z_0$. A termination with a direct electrical connection to the ground is called a short circuit and has $Z_L = 0$. A termination where the line stops but is disconnected from the ground is called an open circuit, which acts as a load impedance $Z_L = \infty$. Because the signal is evolving as it travels down the line we cannot only consider this load impedance to have an effect at its location; the signal as it is transmitted or reflected will interfere with itself, and so any load impedance at any point along the line must be considered at every other point along the line. Any signal entering a line terminated in load Z_L at a distance ℓ through a transmission line with characteristic impedance Z_0 will see an effective input impedance

$$Z_{\mathrm{in}} = Z_0 \frac{Z_{\mathrm{L}} + Z_0 \tanh \gamma\ell}{Z_0 + Z_{\mathrm{L}} \tanh \gamma\ell}. \tag{2.22}$$

For the case of a short or an open, this simplifies to

$$Z_{\mathrm{in}}^{\mathrm{short}} = Z_0 \tanh \gamma\ell, \tag{2.23}$$

$$Z_{\mathrm{in}}^{\mathrm{open}} = -Z_0 \coth \gamma\ell. \tag{2.24}$$

2.1.4 Scattering Parameters

When measuring a microwave resonator, there is difficulty in defining or measuring the voltage or current of a system at the ports. This is due in large part to the fact that when measuring these networks one usually wants to measure both magnitude (as inferred from the power) and the phase of the wave along the line. At this point, the voltages and currents become something of a cumbersome distraction, and the preferred measurement is what is referred to as the scattering matrix. For an N-port system, the scattering matrix is an $N \times N$ matrix that relates the voltage waves incident upon the ports to the waves reflected at the ports. These values can be measured directly with a vector network analyzer (VNA), and it is this data that is recorded for all microwave measurements in this work.

An element of the scattering matrix can be defined as [21]

$$S_{ij} = \left.\frac{V_i^-}{V_j^+}\right|_{V_k^+=0 \text{ for } k\neq j}, \tag{2.25}$$

where S_{ij} is found by driving port j with a voltage wave V_j^+, while measuring the reflected voltage wave V_i^- at port i. All other ports are then terminated with a matched impedance load such that there are no reflections; then all ports except for the jth port have no incident waves. In this way, S_{11} is the reflection when driving on port 1, and S_{21} is the transmission measured at port 2 when driving on port 1. It is from these values that all other properties of these microwave resonators are derived.

2.1.5 Statistical Mechanics of a Transmission Line

Consider a lossless LC resonator coupled to a semi-infinite transmission line with impedance Z_0. To find the spectral density of the input field, V_{in}, we can consider the voltage and current of a line being driven with an input wave and terminated in a matched load,

$$\begin{aligned} V(z=0,t) &= V_{\text{in}}(t) + V_{\text{out}}(t), \\ I(z=0,t) &= \frac{V_{\text{in}}(t)}{Z_0} - \frac{V_{\text{out}}(t)}{Z_0}. \end{aligned} \tag{2.26}$$

Combining these equations to eliminate the output field, we find that

$$I(z=0,t) = \frac{2V_{\text{in}}(t)}{Z_0} - \frac{V(z=0,t)}{Z_0}. \tag{2.27}$$

When we consider this source being coupled to an LC resonator, we can then use Kirchoff's current law to write the equation of motion of the flux inside the inductor as

$$\frac{d^2\Phi}{dt^2} + \frac{1}{Z_0 C}\frac{d\Phi}{dt} + \frac{\Phi}{LC} = \frac{2}{Z_0 C}V_{\text{in}}\,(t). \tag{2.28}$$

Comparing eq. (2.1) and eq. (2.28), the transmission line behaves in the same manner as a resistor in an LCR resonator.

Solving eq. (2.28) in frequency space then gives

$$\Phi(\omega) = K(\omega)I_{\text{in}}(\omega) = \frac{2/Z_0 C}{(\omega_0^2 - \omega^2) - i\omega/Z_0 C}V_{\text{in}}(\omega), \tag{2.29}$$

where $K(\omega)$ is the response of the system. The spectrum of the flux is taken from the spectrum of the input voltage by

$$\bar{S}_{\Phi\Phi}(\omega) = |K(\omega)|^2 \bar{S}_{V_{\text{in}}\,V_{\text{in}}}\,[\omega] \tag{2.30}$$

for single side spectral density $\bar{S}(\omega) = S(\omega) + S(-\omega)$.

A transmission line at temperature T generates a white input voltage noise[18], and so we can consider the effect of the line on the LC resonator as that of a thermal bath. If we had an LC resonator connected to a transmission line of temperature T and no external drive, thermal fluctuation of the transmission line would drive the resonator into thermal equilibrium[18] with the line.

Then in thermal equilibrium we solve for the energy of the LC resonator,

$$\bar{E} = \bar{S}_{V_{\text{in}}V_{\text{in}}}\,[\omega_0]\,\frac{1}{L}\int_0^\infty \frac{d\omega}{2\pi}|K(\omega)|^2 = \bar{S}_{V_{\text{in}}V_{\text{in}}}\,[\omega_0]\,/Z_0 = k_B T, \tag{2.31}$$

then

$$\bar{S}_{V_{\text{in}}V_{\text{in}}}[\omega] = Z_0 k_B T. \tag{2.32}$$

We define a noise current $I_n = 2V_{\text{in}}/Z_0$, we can say the transmission line acts as a noisy current source in parallel with a resistor leading to current noise [18]

$$\bar{S}_{I_n I_n}(\omega) = \frac{4k_B T}{Z_0}, \tag{2.33}$$

or equivalently a noisy voltage source $V_n = Z_0 I_n$ which is wired in series with a resistor that has voltage noise

$$\bar{S}_{V_n V_n}(\omega) = Z_0^2 \bar{S}_{I_I I_n}(\omega) = 4Z_0 k_B T. \tag{2.34}$$

2.1.6 Capacitive Coupling to an RLC resonator

A resonator directly coupled to a transmission line will inherently hit a limit of quality; an LC resonator with impedance Z_0 directly coupled to a transmission line will be limited to a maximum quality factor of

$$Q = \frac{\omega_0}{\kappa} = \omega_0 Z_0 C. \tag{2.35}$$

Thus, even if the environment is completely non-dissipative, energy can simply escape into the transmission line. One can amend this issue by using a capacitor to couple the transmission line to the resonator. Consider the generic case, with internal resonator losses given by a resistance R, with input and output capacitors (C_{in} and C_{out}). Then looking at the resonator from the input or output we have a modified impedance Z'_σ

$$Z'_\sigma = \frac{1 + q_\sigma^2}{q_\sigma^2} Z_0, \tag{2.36}$$

with modified capacitance

$$C'_\sigma = \frac{1}{1 + q_\sigma^2} C_\sigma, \tag{2.37}$$

where $q_\sigma = \omega Z_0 C_\sigma$ and $\sigma = in$ or out for notational convenience.

This leads to a small shift in frequency of the resonance as the total capacitance of the system becomes $C_{\text{tot}} = C + C_{\text{in}} + C_{\text{out}}$, so we have $\omega' = 1/\sqrt{LC_{\text{tot}}}$. While this may seem to leave the system no different from directly coupling to a resonator of different capacitance, the difference becomes obvious when we examine the quality factor of the

system. The quality factor of the loaded resonator becomes $Q = \left(\frac{1}{Q_{\rm i}} + \frac{1}{Q_{\rm in}} + \frac{1}{Q_{\rm out}}\right)^{-1}$ where

$$Q_{\rm i} = \frac{R}{Z_{LC}}, \tag{2.38}$$

is the internal quality factor and

$$Q_{\rm in,out} = \frac{Z_0'}{Z_{LC}} = \frac{1}{q_\sigma^2}\frac{Z_0}{Z_{LC}}, \tag{2.39}$$

for $Z_{LC} = \sqrt{L/C_{\rm tot}}$ are the coupling quality factors. Here our internal quality factor is largely unaffected, but our external quality factor is enhanced by $1/q_\sigma^2$, a significant improvement.

Before moving on we should amend our equation of motion to account for this change. Taking an RLC resonator coupled as described, and adapting eq. (2.27) we can find the equation of motion of the magnetic flux in the inductor to be [18]

$$I(z=0,t) = \sum_{\sigma={\rm int,in,out}} \left(\frac{2V_{\sigma,\,{\rm in}}\,(t)}{Z_\sigma'} - \frac{V(z=0,t)}{Z_\sigma'}\right). \tag{2.40}$$

Here the internal component has $Z_{\rm int}' = R$ which accounts for internal dissipation from the resistor, and the input and output components act as an effective input/output transmission line with $Z_\sigma' = Z_0/q_\sigma^2$. Then the equation of motion eq. (2.28) becomes

$$\frac{d^2\Phi}{dt^2} + \kappa\frac{d\Phi}{dt} + \omega_0^2\Phi = 2\kappa V_{\rm in}(t), \tag{2.41}$$

with

$$\kappa = \sum_{\sigma={\rm int,in,out}} K_\sigma, \tag{2.42}$$

$$V_{\rm in}(t) = \sum_{\sigma={\rm int,in,out}} \frac{\kappa_\sigma}{\kappa} V_{\sigma,\,{\rm in}}\,(t), \tag{2.43}$$

and

$$\kappa_\sigma = 1/Z_\sigma' C_{\rm tot}\,. \tag{2.44}$$

Then if we can assume the resistor and the transmission lines are in thermal equilibrium with the bath at temperature T the noise spectrum of $V_{\sigma,\,{\rm in}}$ as given by eq. (2.32) is then

$$\bar{S}_{V_{\sigma,\,{\rm in}}\,V_{\sigma',\,{\rm in}}}[\omega] = Z_\sigma k_B T \delta_{\sigma,\sigma'}. \tag{2.45}$$

2.1.7 Quantization of a Transmission Line

We are now going to undertake the somewhat arduous task of quantizing a transmission line. As we've seen, a transmission line with impedance Z_0 can be described as a chain of LC resonators with capacitance and inductance per unit length C_ℓ and L_ℓ. The Lagrangian of such a system with a length d is given by [22]

$$L = \int_0^d \left[\frac{1}{2} C_\ell \dot{\Phi}(z,t)^2 - \frac{1}{2L_\ell} \left(\frac{\partial \Phi}{\partial z}(z,t) \right)^2 \right] dz \tag{2.46}$$

for a given local flux $\Phi(z,t)$. We can use the Eular-Lagrange equation to find an equation of motion

$$\frac{\partial^2 \Phi}{\partial t^2} - v^2 \frac{\partial^2 \Phi}{\partial z^2} = 0 \tag{2.47}$$

where $v = 1/\sqrt{L_\ell C_\ell}$ is the phase velocity along the transmission line. The general solution is then

$$\Phi(z,t) = \sum_{n=1}^{\infty} \Phi_n(t) \cos\left(k_n z + \alpha_n\right), \tag{2.48}$$

or for the entire line,

$$\Phi_n(t) = A_n \cos\left(\omega_n t + \beta_n\right). \tag{2.49}$$

Here, k_n, α_n, A_n, B_n are given by the boundaries for a signal at $\omega_n = v k_n$. By combining eq. (2.46) and eq. (2.48) we find a new Lagrangian

$$L = \sum_{n=1}^{\infty} \left(\frac{1}{2} C_n \dot{\Phi}_n^2 - \frac{1}{2L_n} \Phi_n^2 \right), \tag{2.50}$$

where the system acts as an infinite chain of completely uncoupled LC resonators with $C_n = C_\ell d/2$ and $L_n = \frac{2L_\ell d}{n\pi^2}$. We can then define a canonically conjugate momentum to be

$$Q_n = \frac{\partial L}{\partial \dot{\Phi}_n} = C \dot{\Phi}_n, \tag{2.51}$$

which leads us to the Hamiltonian

$$H = \sum_{n=1}^{\infty} Q_n \dot{\Phi}_n - L = \sum_{n=1}^{\infty} \left(\frac{Q_n^2}{2C_n} + \frac{1}{2L_n} \Phi_n^2 \right). \tag{2.52}$$

The optimistic among us may assume we're essentially finished, and they would be wrong. We now begin to quantize the individual LC resonators in the infinite chain that is the transmission line. First, then, a commutation relation:

$$\left[\hat{\Phi}_n, \hat{Q}_m\right] = i\hbar\delta_{n,m}, \tag{2.53}$$

which gives the magnetic flux Φ_n and the charge Q_n of the nth resonator as

$$\hat{\Phi}_n = \sqrt{\frac{\hbar Z_n}{2}}\left(\hat{a}_n + \hat{a}_n^\dagger\right) \tag{2.54}$$

and

$$\hat{Q}_n = -i\sqrt{\frac{\hbar}{2Z_n}}\left(\hat{a}_n - \hat{a}_n^\dagger\right). \tag{2.55}$$

Here we have an effective impedance $Z_n = \sqrt{L_n/c_n} = 2Z_0/n\pi$, and $\hat{a}_n$ $\hat{a}_n^\dagger$ are the annihilation and creation operators of the mode in the nth LC resonator in the line. As is to be expected they satisfy the commutation relation

$$\left[\hat{a}_n, \hat{a}_m^\dagger\right] = i\hbar\delta_{n,m}, \tag{2.56}$$

which leads us to our final Hamiltonian

$$\hat{H} = \sum_{n=1}^{\infty} \hbar\omega_n \left(\hat{a}_n^\dagger \hat{a}_n + \frac{1}{2}\right) \tag{2.57}$$

for $\omega_n = 1/\sqrt{L_n C_n}$. Recreating the local flux operator in eq. (2.48) in these terms gives us

$$\hat{\Phi}(z,t) = \sum_{n=1}^{\infty} \sqrt{\frac{\hbar Z_n}{2}}\left(\hat{a}_n e^{-i\omega_n t} + \hat{a}_n^\dagger e^{i\omega_n t}\right)\cos\left(k_n z\right), \tag{2.58}$$

which we can finally use to solve for the voltage,

$$\hat{V}(z,t) = \frac{\partial\Phi}{\partial t}(z,t) = -i\sqrt{\frac{2v}{d}}\sum_{n=1}^{\infty}\sqrt{\frac{\hbar\omega_n Z_0}{2}}\left(\hat{a}_n e^{-i\omega_n t} - \hat{a}_n^\dagger e^{i\omega_n t}\right)\cos\left(k_n z\right). \tag{2.59}$$

It can be very illuminating to break apart the voltage in the system into inbound or "right" solutions, and outbound or "left" solutions

$$\hat{V}(z,t) = \hat{V}_{\text{in}}\left(t - \frac{z}{v}\right) + \hat{V}_{\text{out}}\left(t + \frac{z}{v}\right), \tag{2.60}$$

where we have

$$\hat{V}_{\text{in}}\left(t-\frac{z}{v}\right)=-i\int_0^\infty\frac{d\omega}{2\pi}\sqrt{\frac{\hbar\omega Z_0}{2}}\left\{\hat{a}_{\text{in}}\left(\omega\right)e^{-i\omega\left(t-\frac{z}{v}\right)}-\left(\hat{a}_{\text{in}}\left(\omega\right)\right)^\dagger e^{i\omega\left(t-\frac{z}{v}\right)}\right\},$$
$$\hat{V}_{\text{out}}\left(t+\frac{z}{v}\right)=-i\int_0^\infty\frac{d\omega}{2\pi}\sqrt{\frac{\hbar\omega Z_0}{2}}\left\{\hat{a}_{\text{out}}\left(\omega\right)e^{-i\omega\left(t+\frac{z}{v}\right)}-\left(\hat{a}_{\text{out}}\left(\omega\right)\right)^\dagger e^{i\omega\left(t+\frac{z}{v}\right)}\right\}. \tag{2.61}$$

Here the inbound and outbound modes are given by $\hat{a}_{\text{in}}\left(\omega\right)$ and $\hat{a}_{\text{out}}(\omega)$ respectively

$$\begin{aligned}\hat{a}_{\text{in}}\left(\omega\right)&=2\pi\sqrt{\frac{v}{2d}}\sum_{n>0}\hat{a}_k\delta\left(\omega-\omega_k\right),\\ \hat{a}_{\text{out}}\left(\omega\right)&=2\pi\sqrt{\frac{v}{2d}}\sum_{n<0}\hat{a}_k\delta\left(\omega-\omega_k\right).\end{aligned} \tag{2.62}$$

Then as we take the limit that $d\to\infty$, the only non-vanishing commutators of the operators are

$$\begin{aligned}\left[\hat{a}_{\text{in}}\left(\omega\right),\left(\hat{a}_{\text{in}}^\dagger\left(\omega'\right)\right)\right]&=2\pi\delta\left(\omega-\omega'\right),\\ \left[\hat{a}_{\text{out}}\left(\omega\right),\left(\hat{a}_{\text{out}}^\dagger\left(\omega'\right)\right)\right]&=2\pi\delta\left(\omega-\omega'\right).\end{aligned} \tag{2.63}$$

Now, if we consider that the transmission line is in thermal equilibrium, we have that

$$\left\langle\left(\hat{a}_{\text{in}}^\dagger(\omega)\right)\hat{a}_{\text{in}}\left(\omega'\right)\right\rangle=2\pi\delta\left(\omega-\omega'\right)n_{\text{th}}(\omega), \tag{2.64}$$

with the thermal occupation given by the Bose-Einstein distribution

$$n_{\text{th}}(\omega)=\frac{1}{\left(\exp\frac{\hbar\omega}{k_BT}-1\right)}. \tag{2.65}$$

As we've quantized the field we can now also calculate the quantum statistics of the voltage distribution, finding the noise spectrum of the input voltage to be

$$\bar{S}_{V_{\text{in}}V_{\text{in}}}\left[\omega\right]=\int dt\left\langle\left\{\hat{V}_{\text{in}}\left(t\right),\hat{V}_{\text{in}}\left(0\right)\right\}\right\rangle e^{i\omega t}=\frac{Z_0}{2}\hbar|\omega|\coth\left(\frac{\hbar|\omega|}{2k_BT}\right). \tag{2.66}$$

Please note that in the case where $k_BT\gg\hbar\omega$ this reduces to the case of eq. (2.32). Also of interest, as the semi-infinite transmission line behaves like a resistor, we can use the knowledge that the quantum noise from a resistor is equivalent to the noise voltage of an open terminal of the line, $V=2V_{\text{in}}$ to find that

$$\bar{S}_{VV}[\omega]=4\bar{S}_{V_{\text{in}}V_{\text{in}}}[\omega]=2Z_0\hbar|\omega|\coth\left(\frac{\hbar|\omega|}{2k_BT}\right). \tag{2.67}$$

2.1.8 Quantum Langevin Equation of an LC Resonator

By replacing our variables in eq. (2.28) with their quantum operator equivalents, and taking $\hat{I}_{in}(t) = \frac{2}{Z_0}\hat{V}_{\text{in}}(t)$, we have our quantum Langevin equation

$$\frac{d^2\hat{\Phi}}{dt^2} + \frac{1}{Z_0 C_{\text{tot}}}\frac{d\hat{\Phi}}{dt} + \frac{\hat{\Phi}}{LC_{\text{tot}}} = \frac{1}{C_{\text{tot}}}\hat{I}_n(t). \tag{2.68}$$

This is where we can begin to make some helpful approximations. Since we consider high Q resonators ($Q \gg 1$), and probe the dynamics only in a narrow band around the cavity resonance frequency, we can rewrite the input voltage as

$$\hat{V}_{\text{in}}(t) \simeq -i\sqrt{\frac{\hbar Z\omega_0}{2}}\left(e^{-i\omega_0 t}\int_{-\omega_0}^{\infty}\frac{d\omega}{2\pi}\hat{a}_{\text{in}}\left[\omega+\omega_0\right]e^{-i\omega t} - \text{ h.c. }\right) \tag{2.69}$$

where h.c. is the hermitian conjugate. Now since we only probe near to the cavity frequency we can change the limit of the integral from $-\infty$ to ∞. We are then able to define the operator of the input field to be

$$\hat{a}_{\text{in}}(t) = \int_{-\infty}^{\infty}\frac{d\omega}{2\pi}\hat{a}_{\text{in}}\left[\omega+\omega_0\right]e^{-i\omega t}, \tag{2.70}$$

which in turn satisfies

$$\left[\hat{a}_{\text{in}}(t), \hat{a}_{\text{in}}^{\dagger}(t')\right] = \delta\left(t-t'\right), \tag{2.71}$$

and allows us to simplify the input voltage as

$$\hat{V}_{\text{in}}(t) = -i\sqrt{\frac{\hbar Z\omega_0}{2}}\left(\hat{a}_{\text{in}}(t)e^{-i\omega_0 t} - \hat{a}_{\text{in}}^{\dagger}(t)e^{i\omega_0 t}\right). \tag{2.72}$$

The flux operator can be rewritten in the frame which rotates at ω_0 to be

$$\hat{\Phi}(t) = \sqrt{\frac{\hbar Z}{2}}\left(\hat{a}(t)e^{-i\omega_0 t} + \hat{a}^{\dagger}(t)e^{i\omega_0 t}\right), \tag{2.73}$$

where $\hat{a}(t)$ and $\hat{a}(t)^{\dagger}$ are the field envelope. These new flux and voltage operators can then be substituted into our quantum Langevin equation. We then separate the parts which rotate at $e^{i\omega t}$ and $e^{-i\omega t}$ to get

$$\frac{1}{2\omega_0}i\frac{d^2\hat{a}}{dt^2} + \frac{d\hat{a}}{dt} + \frac{1}{2Q}i\frac{d\hat{a}}{dt} + \frac{\kappa}{2}\hat{a} = \sqrt{\kappa}\hat{a}_{\text{in}}(t). \tag{2.74}$$

If we make the approximations that the envelope rotates slowly $\frac{d^2\hat{a}}{dt^2} \ll \omega_0 \frac{d\hat{a}}{dt}$, and that we have a high quality resonator ($Q \gg 1$) then in the lab frame we have

$$\frac{d\hat{a}(t)}{dt} + \left(i\omega_0 + \frac{\kappa}{2}\right)\hat{a}(t) = \sqrt{\kappa}\hat{a}_{\text{in}}(t). \tag{2.75}$$

For any system with multiple ports, $\sigma = 1, 2, 3...$ we have the input-output relation

$$\hat{a}_{\sigma,\text{ out}}(t) = \hat{a}_{\sigma,\text{ in}}(t) - \sqrt{\kappa_\sigma}\hat{a}(t). \tag{2.76}$$

2.2 Coplanar Waveguides

While it is often convenient to describe the properties of these circuits independent of their geometry, one must consider the geometry of the system to design it. Regardless of geometry, the circuit must comprise a central conductor and a ground. Perhaps most familiar is the coaxial cable, where the center conductor is contained in a conducting outer ground separated by a dielectric.

Standout among various designs is the coplanar waveguide (CPW). It consists of a center conductor and ground deposited in the same plane, on a face of a dielectric substrate. This is convenient, insofar as both components can be fabricated on the same face of the substrate. This means that the gap between ground and conductor can be scaled from a few microns to several millimeters without changing the line impedance as long as the ratio of their dimensions remains the same[2] . This allows us to change the confinement, and therefore the intensity, of our field profile without causing undue reflections.

While any transmission line can be described by the general transmission line equations discussed earlier, key quantities such as the impedance and wave propagation velocity will be determined by the geometry of the line. These relationships are often complex, so for convenience, we will take them from [23]. For a CPW on a substrate of height h, center conductor width a and gap to the ground plane s (giving total width

[2]This only holds true if the substrate height is sufficiently large, and the space above the line is uninterrupted for roughly $3b$ This holds true for all transmission lines used here

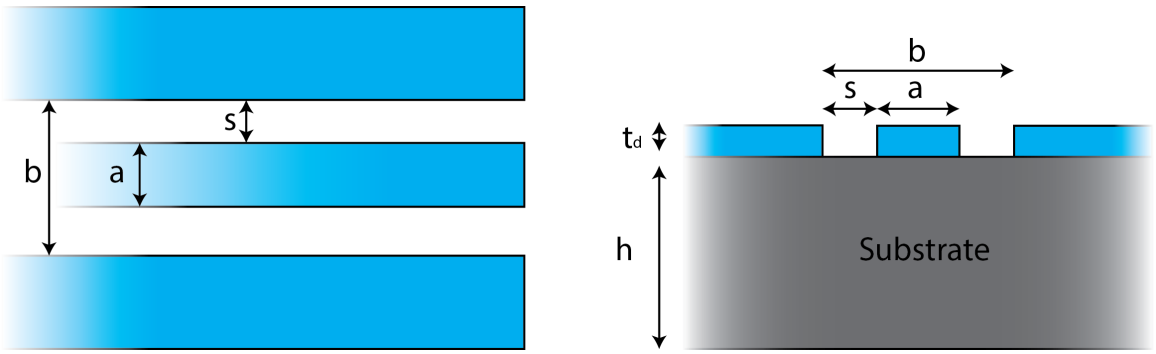

Figure 2.3: Schematic diagram of the elements in a coplanar waveguide (CPW) transmission line. Conductor shown in cyan, with substrate shown in grey.

$b = a + 2s$), and metal film thickness t_d (as shown in fig. 2.4) we have characteristic impedance

$$Z_0^{CPW} = \frac{60\pi}{\sqrt{\epsilon_{\text{eff}}}} \left(\frac{K(k)}{K\left(k'\right)} + \frac{K\left(k_3\right)}{K\left(k_3'\right)} \right)^{-1}, \tag{2.77}$$

where K is the elliptic integral of the first kind. Then

$$\widetilde{K} = \frac{K\left(k'\right) K\left(k_3\right)}{K(k) K\left(k_3'\right)}, \tag{2.78}$$

$$k = \frac{a}{b}, \tag{2.79}$$

$$k_3 = \frac{\tanh\left(\frac{\pi a}{4h}\right)}{\tanh\left(\frac{\pi b}{4h}\right)}, \tag{2.80}$$

$$k' = \sqrt{1 - k^2}, \tag{2.81}$$

and

$$k_3' = \sqrt{1 - k_3^2}. \tag{2.82}$$

We then need to find our effective dielectric constant ϵ_{eff}, which is simply a geometric average of the dielectric constant of the substrate ϵ_r and vacuum within the mode volume,

$$\epsilon_{\text{eff}} = \frac{1 + \epsilon_r \widetilde{K}}{1 + \widetilde{K}}. \tag{2.83}$$

For non-magnetic substrates such as the ones used here, we can then derive the effective speed of propagation

$$\nu_{\text{eff}} = \frac{c}{\sqrt{\epsilon_{\text{eff}}}}. \tag{2.84}$$

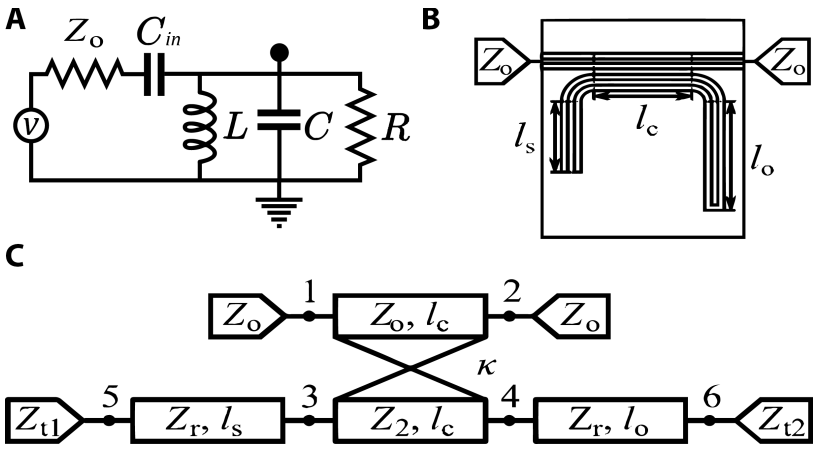

Figure 2.4: A: Circuit schematic of an LCR resonator coupled through capacitance C_{in} to an environment with characteristic impedance Z_0.
B: A transmission line with input impedance Z_i and output impedance Z_o, coupled to a quarter wavelength CPW resonator in a notch coupled configuration.
C: Transmission line diagram of the system depicted in b, where a transmission line of impedance Z_0 runs adjacent to another line of impedance Z_2 for distance l_c, which will terminate after a bend in a short ($Z_{t1} = 0$) and an open ($Z_{t2} = \infty$).

2.2.1 Coupling Between Adjacent Coplanar Waveguides

Coupling between waveguides is dependent on the geometry of the individual waveguides and their relative position and orientation. Within this work, we have only considered the coupling between two coplanar waveguides adjacent to each other within the same plane.

In the simplest case where coupling between adjacent coplanar waveguides is low we can neglect the effects of finite substrate thickness. This approximation will give a lower bound of the coupling, as infinite substrate height increases coupling. As is more fully addressed in [24], coupling C between adjacent lines with spacing D is approximated by

$$C = -20 \log_{10} (1 - Z_0/Z_\infty) , \tag{2.85}$$

where Z_∞ is the line impedance for $D \to \infty$, and

$$\frac{Z_0}{Z_\infty} = \frac{K\left(\sqrt{(1-k_8^2)}\right)}{K\left(k_8\right)} \frac{K\left(k_9\right)}{K\left(\sqrt{(1-k_9^2)}\right)}, \tag{2.86}$$

$$k_9 = \frac{2\sqrt{ab}}{a+b}, \tag{2.87}$$

and

$$k_8 = \frac{k_9}{\left[1-(b-a)^2/D^2\right]^{1/2}}. \tag{2.88}$$

While the full derivation of coupling between adjacent coplanar waveguides is too involved to present here, we can determine the frequency shift in a $\lambda/4$ resonator as depicted in fig. 2.4 b and c, due to the presence of the feedline as well as the loss to the feedline as given in [25]

$$\Delta f_r^a = -\frac{c_l \kappa^2 \sin\theta(2\cos\psi + \cos\theta)}{4\pi\left(l_c + l_o + l_s\right)} - \frac{c_l\left(Z_2 - Z_r\right)\sin\theta\cos\psi}{2\pi Z_r\left(l_c + l_o + l_s\right)}, \tag{2.89}$$

$$\frac{1}{Q^a} = \frac{2\kappa^2 \sin^2\theta}{\pi(2p-1)}. \tag{2.90}$$

In this, κ is a dimensionless coupling coefficient, $p = 1, 2, 3...$ is the mode number, where a quarter wave resonator will have center frequency

$$f_r^{(0)} = \frac{c_l}{4l}(2p-1), \tag{2.91}$$

and θ and ψ are phase variables given by

$$\psi = 2\pi\left(l_c + 2l_o\right) f_r^{(0)}/c_l, \tag{2.92}$$

$$\theta = 2\pi l_c f_r^{(0)}/c_l. \tag{2.93}$$

2.2.2 Kinetic Inductance

When current is made to flow in any medium there is an induced magnetic flux stored in magnetic fields, although this fails to account for the kinetic energy of the electrons themselves. In normal metals this kinetic inductance is a minute effect compared to

the resistivity of the normal metal and is thus ignored. Within superconductors, however, the resistivity is suppressed; then the energy required to accelerate Cooper pairs within the superconducting medium, which is normally too small an effect to perceive, becomes prominent. This effectively opposes any electromotive force, similar to the finite rate of change of magnetic flux in an inductor, hence "kinetic inductance". Please note that with this discussion, as with all other discussions within this work we refer only to models in the microwave frequency regime, up to $\approx 70\ GHz.$// We must then treat the inductance of a transmission line not only as the geometric inductance but as the sum of geometric and kinetic inductance, $L_\ell = L_g + L_K$.

Within a coplanar waveguide, the geometric inductance per unit length can be given as [26]

$$L_g = \frac{\mu}{4}\frac{K\left(k'\right)}{K(k)}, \tag{2.94}$$

and the kinetic energy of a superconducting current carried by n_s charge carriers is given by

$$E = \int \frac{1}{2} n_{\mathrm{s}} m v^2 dV = \int \frac{1}{2}\frac{n_{\mathrm{s}} m}{A e^2} I^2 = \frac{1}{2}\mu\lambda_{\mathrm{L}}^2 \frac{\ell}{at} I^2, \tag{2.95}$$

with cross sectional area $A = at_d$ and London penetration depth $\lambda_{\mathrm{L}} = \left(\mu m / n_{\mathrm{s}} e^2\right)^{-1/2}$. As kinetic inductance is proportional to I^2 it is generally treated as a function of the form

$$L_{\mathrm{K}} = \mu \frac{\lambda_{\mathrm{L}}^2}{at} g_g(s, a, t_d), \tag{2.96}$$

where $g_g(s, a, t_d) \approx 5$ is derived via conformal mapping in [26], or more generally

$$g_g(s, a, t_d) = \frac{1}{2k^2 K(k)^2}\left(-\ln\left(\frac{t_d}{4a}\right) + \frac{2(a+s)}{(a+2s)}\ln\left(\frac{s}{a+s}\right) - \frac{a}{(a+2s)}\ln\left(\frac{t_d}{4(a+2s)}\right)\right). \tag{2.97}$$

Here, g_g is simply a geometric factor that relates the available cross-sectional area for current to travel to the kinetic inductance. It's derivation relies heavily upon conformal mapping methods too involved to describe here which are discussed in [26].

There are several properties of note, firstly that while the geometry plays a large factor in the kinetic inductance, it depends very strongly on the London penetration

depth of the superconductor. This in turn is dependent on the magnetic environment and any stray radiation, which can break apart Cooper pairs. Kinetic inductance also depends on film thickness; if the film is thickness smaller than λ_L it is more accurate to use film thickness t_d when calculating g_g, under presumption that some current flow penetrates the entire depth of the conductor. In thicker films g_g is more accurately calculated using by $t_d \approx 2\lambda_L$ due to penetration depth in superconductors limiting the cross-sectional area of current flow. There is also a small dependence of λ_L but that is neglected here.

It should also be noted that $g(s, a, t_d)$ is only weakly dependent on a and t_d, the kinetic inductance then decreases with the cross-sectional area of the center pin, as this decreases the kinetic energy of electrons for a set current.

2.2.3 Losses in Microwave Resonators

Microwave resonators generally suffer from three primary sources of loss, neglecting loss to input and output coupling which can generally be engineered arbitrarily. These loss mechanisms are radiative losses to the external environment, resistive losses from the surfaces of the conductors, and dielectric losses within the dielectric medium.

Radiative Losses

Even in a situation where the materials are perfectly lossless (a dream in itself), the resonator will still lose energy by radiating it into the environment. While not taking into account the meandering of the transmission line, the backing plane, or suppression of radiation via a waveguide there is an analytical solution for radiation loss for a straight quarter wave resonator with a semi-infinite dielectric [27, 28]

$$Q_{rad} = \frac{\pi(1+\epsilon)^2}{2\epsilon^{5/2}} \frac{\eta_0}{Z_0} \frac{1}{I'(\epsilon, n)} \frac{1}{n - \frac{1}{2}} \left(\frac{L}{b}\right)^2 \tag{2.98}$$

for a resonator of total length L and total spacing between ground planes b in the nth mode, where $\eta_0 = 377$, and Ω is the impedance of free space. Here I' is a tabulated,

analytically calculated value which for our use cases of $n = 1$ and $\epsilon = 11.86$ we use $I' \simeq 1.62$.

In our devices, we have lengths of order $L \approx$ mm with ground plane separations on orders $b = 25$ μm, which gives $Q_{rad} \cong 5 \times 10^6$. Radiative losses should then not be considered the limiting factor in quality even before considering the radiation suppression given by the sample holder channel.

Resistive Losses

While one would hope that working with superconductors would mean that resistive losses are non-existent, many parts of life are disappointing. The superconductor can be modeled as containing two fluids, quasiparticles of finite resistance and number density n_n, and a fluid of superconducting Cooper pairs with zero DC resistance, but with finite AC kinetic inductance. These two fluids effectively act as a resistor (quasiparticles) and an inductor (superconductors) in parallel. As in any parallel circuit of this kind, the larger the resistance the more of the current will travel through the inductor. As the normal fluid has a resistance inversely proportional to the number density of quasiparticles, the lower the temperature is below the critical temperature, the less current will flow through the fluid with finite resistance. However, at any finite temperature and frequency, some small fraction of the current will flow through the lossy normal fluid, limiting maximum Q.

For a superconductor with normal conductance $\sigma_n = n_n e^2 \tau_n / m$, where τ_n is the scattering time of the quasiparticles [29], the superconductor has AC conductance

$$\sigma = \sigma_n + i\frac{A}{\omega L_K}, \tag{2.99}$$

where A is the cross-sectional area along which the current flows.

To truly understand the losses imposed by this limited conductance it is expedient to transform the conductance into an effective resistance per unit length [26],

$$R_\ell = L_{\mathrm{K}}^2 \omega^2 \sigma_{\mathrm{n}} = \frac{n_{\mathrm{n}}}{n_{\mathrm{s}}} L_{\mathrm{K}} \omega^2 \tau_{\mathrm{n}} g(s, a, t). \tag{2.100}$$

While this form doesn't immediately indicate any temperature dependence, BCS theory tells us that

$$n_n/n_s = \exp(-1.76T_C/T), \tag{2.101}$$

and using the London equations we can phenomenologically model kinetic inductance as changing in temperature roughly as

$$L_K \propto \lambda_L^2 \approxeq \lambda_L(0)^2 \left(1 - \left(\frac{T_c}{T}\right)^4\right). \tag{2.102}$$

Dielectric Losses

Regardless of any loss along the conductor, there is also loss when electromagnetic field lines pass through a lossy material. This loss can be expressed as an additional imaginary component in the dielectric constant, such that $\epsilon = \epsilon_{\text{re}} + i\epsilon_{\text{im}}$. This loss is expressed as the conductance in eq. (2.18) with the capacitance of the line C_ℓ giving conductance

$$G = C_\ell \omega \tan\left(\frac{-\epsilon_{\text{im}}}{\epsilon_{\text{re}}}\right), \tag{2.103}$$

which in turn gives us a limiting Q of an LCR resonator made with this capacitor as

$$Q_{\text{diel}} = \frac{\omega_r C}{G} = \frac{1}{\tan\left(\frac{-\epsilon_{\text{im}}}{\epsilon_{\text{re}}}\right)} = \left(\frac{1}{\tan\delta}\right). \tag{2.104}$$

As dielectric losses normally form the limit of quality factor, several materials are the standard choices for substrate, namely silicon, and sapphire[30].

2.2.4 Resonance Fitting Methods: Notch Configuration

When measuring microwave resonators one must choose what configuration to measure them in, reflection or transmission. While transmission may seem preferable, one cannot directly determine the internal losses of a transmission measurement as you are missing a baseline to reference. Traditional reflection measurements are likewise limited, as they cannot measure multiple multiplexed devices. This can be resolved by measuring in a so-called notch configuration, where the resonator to be measured

is coupled to a transmission line, which is measured in transmission (S_{21}), and the resonance appears as a dip in the spectrum, where the signal couples into and is reflected out of the device to continue along the transmission line. This is fundamentally different from measuring in transmission; here signals couple into and out of the resonator from the feed line with a phase shift imparted by the resonator and mix with the feedline signal. The notch configuration effectively acts as an interferometer. This data can then be used to extract not only the center frequency of the resonance f_r, but both the internal quality factor of the resonator Q_i as well as the external, or coupling, quality factor Q_e (which is used in cases where $Q_{\text{in}} = Q_{\text{out}}Q_e$. Following [31] Q_e is complex ($Q_e = |Q_e| \exp(-i\Phi)$) with impedance mismatches quantified by Φ. The fitting and extraction of this data has been well studied [32] and is given by

$$S_{21}^{\text{notch}}(f) = \underbrace{ae^{i\alpha}e^{-2\pi i f\tau}}_{\text{environment}} \underbrace{\left[1 - \frac{(Q_t/|Q_e|)\, e^{i\Phi}}{1 + 2iQ_t\,(f/f_r - 1)}\right]}_{\text{resonator}}. \tag{2.105}$$

The first term, which accounts for the environment, models the additional changes to amplitude a, the phase shift α and the electronic, or cable, delay τ when probing the system at frequency f. These account for any net changes to amplification or attenuation on the cables outside the device under test (DUT), the offset phase change due to the length and impedance of cabling outside of the DUT, and the finite phase change, which is proportional to the applied frequency, as the signal travels at finite speed down the line.

The second term, labeled the resonator term above, accounts for the signal interaction with the resonator of interest itself. Here as before, f_r is the resonance frequency, Q_t is the loaded or total quality factor such that $Q_l^{-1} = Q_i^{-1} + \text{Re}\{Q_e^{-1}\}$, and Φ quantifies the impedance mismatch. There is some debate within the literature whether the term $e^{i\Phi}$ arises from differing input and output impedances at the two ports of the resonator [31], or from standing waves in the transmission line [33], but that determination is beyond the scope of this project.

The complete method for geometrically fitting the measurement data is given in [32]

with the methods used corresponding to those used there.

2.3 Modelling Superconductors in FEM simulation

There has been a great deal of academic interest in how superconducting resonators can be modeled in FEM simulations, in large part because low loss superconducting resonators are integral to qubit design [34, 35]. Being able to model the superconducting surface as not only a perfect electric conductor will allow us to account for frequency shifts and losses as mentioned in section 2.2.2. To accurately model our superconducting films we will need to understand some important facets of its BCS (Bardeen, Cooper and Schrieffer) state [36] as well as the device's sensitivity to quasiparticle dissipation [37]. In FEM simulations this is leveraged using surface impedance techniques, namely the Mattis-Bardeen conductivity [38]. Much of this analysis is also discussed in The Physics of Superconducting Microwave Resonator by Jiansong Gao [33] as well as the very handy thesis from Matthew Reagor [39].

A superconducting surface can be modelled via a complex surface impedance ($Z_s = R_s + j\delta X_s$) with a differential surface reactance, δX_s. Measurement of the transmission through the cavity with a VNA provides all the information required to model the impedance as

$$Z_s = \frac{\omega\mu_0\lambda}{p_{\text{mag}}}\left(\frac{1}{Q_m} - 2i\frac{\delta f}{f}\right) \tag{2.106}$$

where λ is the penetration depth, p_{mag} is the magnetic participation ratio (which can be calculated independently as given in eq. (2.119)), Q_m is the quality of the surface conductor, and $\delta f/f$ is the shift in frequency the resonator experiences from the $\lambda = 0$ limit, which is an offset from the zero temperature value $\lambda(T = 0)$. These methods were derived from the theories set forth by Nam in 1967 [40].

BCS superconductors can be considered in two limits, the "dirty" limit where the mean free path of charge carriers ℓ is less than the coherence length ξ, or the clean

limit where the coherence length is less than the mean free path [29]. This effectively measures whether electrons, or in this case Cooper pairs, have an effective mean free path longer (clean) or shorter (dirty) than their coherence length. Clean superconductors behave how one would expect, while in dirty superconductors scattering by non-magnetic impurities suppress the superconductivity [36].

The impedance of superconductors is related to the normal state conductivity by two conductivities, known generally as the Mattis-Bardeen conductivities, such that the impedance is given by [39]

$$Z_s \propto Z_n \times (\sigma_1 - \imath\sigma_2)^{\nu}\,, \tag{2.107}$$

where ν is $-1/2$ in the dirty limit and $-1/3$ in the clean limit. It can then be seen that determining ν for a given material will immediately tell you of which limit—dirty or clean—one is in [41].

At low temperatures we know for any superconductor $\sigma_2 \gg \sigma_1$, so we factor eq. (2.107) for expansion

$$Z_s \propto Z_n \sigma_2^{\nu} \left| 1 + \left(\frac{\sigma_1}{\sigma_2}\right)^2 \right|^{\nu/2} e^{\imath \operatorname{Arg}\left(\left(\frac{\sigma_1}{\sigma_2}\right) - \imath\right)}, \tag{2.108}$$

where for a non-real argument,

$$\operatorname{Arg}\left(\left(\frac{\sigma_1}{\sigma_2}\right) - \imath\right) = 2\arctan\left[\frac{\mathcal{I}\left(\left(\frac{\sigma_1}{\sigma_2}\right) - \imath\right)}{|z| + \mathcal{R}\left(\left(\frac{\sigma_1}{\sigma_2}\right) - \imath\right)}\right]. \tag{2.109}$$

Then, as $\sigma_2 \gg \sigma_1$, $(\sigma_1/\sigma_2) \ll 1$,we can reduce the Arg by expanding an arctangent, resulting in

$$\operatorname{Arg}\left(\left(\frac{\sigma_1}{\sigma_2}\right) - \imath\right) \approx -\frac{\pi}{2} + \left(\frac{\sigma_1}{\sigma_2}\right) + \mathcal{O}\left(\left(\frac{\sigma_1}{\sigma_2}\right)^3\right). \tag{2.110}$$

Then, returning to eq. (2.108), we expand the polynomial

$$\left(1 + \left(\frac{\sigma_1}{\sigma_2}\right)\right)^{\nu/2} \approx 1 + \frac{\nu\left(\frac{\sigma_1}{\sigma_2}\right)^2}{2} + \mathcal{O}\left(\left(\frac{\sigma_1}{\sigma_2}\right)^4\right), \tag{2.111}$$

and have the full surface impedance from eq. (2.108) as

$$Z_s \propto Z_n \sigma_2^{\nu} \left(1 + \frac{\nu \left(\frac{\sigma_1}{\sigma_2}\right)^2}{2} + \mathcal{O}\left(s^4\right)\right) (-\imath) \left(1 + \imath \left(\frac{\sigma_1}{\sigma_2}\right) - \frac{\left(\frac{\sigma_1}{\sigma_2}\right)^2}{2} + \mathcal{O}\left(\left(\frac{\sigma_1}{\sigma_2}\right)^3\right)\right). \tag{2.112}$$

Keeping only leading order terms we then have

$$R_s \propto R_n \sigma_1 \sigma_2^{\nu-1} \tag{2.113}$$

and

$$X_s \propto R_n \sigma_2^{\nu}, \tag{2.114}$$

for

$$Z_s \propto R_n \left(\sigma_1 \sigma_2^{\nu-1} + i\sigma_2^{\nu}\right), \tag{2.115}$$

which allows us to define penetration depth as $\lambda \equiv X_s/(\omega\mu_0)$, and the surface $Q_m \cong \sigma_2/\sigma_1$ for which both conductivities can be calculated explicitly.

So it is then that for a superconductor with energy gap $E = \hbar\Delta(T)$ at reduced temperature $\mathcal{T} = k_B T/\hbar$ we can calculate the dimensionless Mattis-Bardeen conductivities as [29, 39]

$$\sigma_1 = \frac{1}{\omega} \int_{\Delta}^{\infty} d\epsilon \frac{(\epsilon+\omega)\epsilon + \Delta^2}{\sqrt{(\epsilon+\omega)^2 - \Delta^2}\sqrt{\epsilon^2 - \Delta^2}} \left[\tanh \frac{\epsilon+\omega}{2\mathcal{T}} - \tanh \frac{\epsilon}{2\mathcal{T}}\right], \tag{2.116}$$

and

$$\sigma_2 = \frac{1}{\omega} \int_{\Delta-\omega}^{\Delta} d\epsilon \frac{(\epsilon+\omega)\epsilon + \Delta^2}{\sqrt{(\epsilon+\omega)^2 - \Delta^2}\sqrt{\Delta^2 - \epsilon^2}} \left[\tanh \frac{\epsilon+\omega}{2\mathcal{T}}\right]. \tag{2.117}$$

Now, all this work to define these conductivities may seem frivolous, but there are two properties of these values that make them ideal for use:

1. They are easily integrated numerically.

2. They simplify the response of a superconductor to an RF field to one that only depends on the temperature and the frequency compared to the energy gap.

The choice of materials then provides us with the energy gap and the normal state impedance. The BCS energy gap itself has a temperature dependence which is universal with respect to T/T_c, and can be numerically solved as [29]

$$\frac{1}{N(0)V} = \int_0^{\omega_c} \frac{\tanh\left(\frac{1}{2T}\sqrt{\xi^2+\Delta^2}\right)}{\sqrt{\xi^2+\Delta^2}} d\xi \tag{2.118}$$

where $N(0)$ is the the density of states of Cooper pairs at $T = 0$ and V is the BCS interaction strength. Using this formula we can simply numerically solve a table of values for any T/T_c, and solve eq. (2.116) and eq. (2.117) to find the complex impedance of a superconductor in a wide range of temperatures and frequencies.

Simply put, to fully model our superconductor we need only to find T_c for our film and determine whether the superconductor is clean or dirty. Then surface impedance boundary conditions can fully model the response of the superconductor in FEM simulation.

As for the magnetic participation ratio, we can calculate it independently with generic skin depth δ, which will be λ for a superconductor [38]

$$p_{\text{mag}} = \frac{\delta \int_{\text{surf}} |H|^2 dA}{\int_{\text{tot}} |H|^2 dV}. \tag{2.119}$$

From this, and the previous fit, we can also immediately extract the penetration depth from the scale of the frequency shift [42],

$$\frac{\delta f(T)}{f} = \frac{1}{\lambda}\left(\frac{p_{\text{mag}}}{\omega\mu_0}\right)\delta X_s(T). \tag{2.120}$$

2.4 Theory of Mechanical Resonators

As with nearly every aspect of modern physics, a simple but effective model for a mechanical resonator is that of a mass on a spring. While our resonators do not exist as a point mass, we overcome this by treating them as a model point mass with effective mass m_{eff} [43]. Then we consider an applied force F where the displacement of the mass from its equilibrium x is determined by the spring constant k_s of the

spring and Hooke's law,

$$F_{\text{spring}} = -k_s x. \tag{2.121}$$

When we consider the motion of the mass, we then have the differential equation

$$m_{\text{eff}}\ddot{x}(t) = -kx(t), \tag{2.122}$$

where the solution is given by $x = x_0 \cos(\omega_m t)$ for an initial position x_0 and with angular frequency $\omega_m = \sqrt{k_s/m_{\text{eff}}}$.

When mechanical losses are present, we represent the damping of the system as a force opposing the motion,

$$F_{\text{damp}} = -m_{\text{eff}}\,\Gamma_m \dot{x} \tag{2.123}$$

where Γ_m is a total damping rate, such that we can model the system as the differential equation with Langevin force from the dissipative environment $F_n(t)$

$$m_{\text{eff}}\,\ddot{x} + m_{\text{eff}}\,\Gamma_m \dot{x} + m_{\text{eff}}\,\omega_m^2 x = F_n(t). \tag{2.124}$$

Acknowledging that this motion is harmonic, we can surmise that $x(t) = x_0 e^{rt}$, finding two solutions,

$$x_{\pm}(t) = \bar{x} e^{-\frac{\Gamma_m}{2}t \pm i\omega_m \sqrt{(1-\Gamma_m^2/4\omega_m^2)}t}. \tag{2.125}$$

It should be noted that this expression assumes $\Gamma_m < 2\omega_m$, which is fulfilled by all mechanical resonators we discuss here. Of note, this indicates that mechanical motion decreases in amplitude as

$$|x_{\pm}(t)| = x_0 e^{-\Gamma_m t/2}. \tag{2.126}$$

The damping force also has the effect of shifting the resonance frequency from its unperturbed value down by a factor of $\sqrt{(1-\Gamma_m^2/4\omega_m^2)}$.

It must also be noted that $x_{\pm}$ are complex, and the position of a mechanical object must be real, we employ a linear combination of x_+ and x_-. We choose the orthogonal

$$\begin{aligned} x_{\text{i}}(t) &= \frac{x_+(t) + x_-(t)}{2} \\ &= \bar{x} e^{-\Gamma_m t/2} \cos(\omega_m t) \end{aligned} \tag{2.127}$$

and

$$\begin{aligned} x_{\mathrm{q}}(t) &= \frac{x_+(t) - x_-(t)}{2i} \\ &= \bar{x} e^{-\Gamma_m t/2} \sin(\Omega_0 t) \end{aligned} \tag{2.128}$$

which are referred to as *in-phase* and *quadrature* components of motion, with x_i being fully real and x_q being fully imaginary.

Notably, the force noise of the bath is then given by

$$\bar{S}_{F_n F_n}[\omega] = 4m\Gamma_m k_B T. \tag{2.129}$$

2.4.1 Quantization of Mechanical Resonators

It will hopefully come as no surprise to the reader that the Hamiltonian for a mechanical harmonic oscillator is given by[44]

$$H = \frac{p^2}{2m} + \frac{m\omega_m^2 x^2}{2}. \tag{2.130}$$

Conveniently, we can simply replace the classical momentum and position with operators $\hat{p}$ and $\hat{x}$ such that

$$[\hat{x}, \hat{p}] = i\hbar. \tag{2.131}$$

We can likewise define creation and annihilation operators

$$\hat{b}^\dagger = \sqrt{\frac{m\omega_m}{2\hbar}} \left(\hat{x} - i\frac{\hat{p}}{m\omega_m} \right), \tag{2.132}$$

and

$$\hat{b} = \sqrt{\frac{m\omega_m}{2\hbar}} \left(\hat{x} + i\frac{\hat{p}}{m\omega_m} \right), \tag{2.133}$$

such that $\left[\hat{b}, \hat{b}^\dagger\right] = 1$. The position and momentum operators can also be defined in terms of these operators and the zero-point motion $x_{zp} = \sqrt{\hbar/2m\omega_m}$ with[44]

$$\hat{x} = x_{zp} \left(\hat{b} + \hat{b}^\dagger \right), \tag{2.134}$$

$$\hat{p} = -m\omega_m x_{zp} i \left(\hat{b} - \hat{b}^\dagger \right). \tag{2.135}$$

We can then write the Hamiltonian as

$$\hat{H} = \hbar\omega_m \left(\hat{b}^\dagger \hat{b} + \frac{1}{2} \right). \tag{2.136}$$

This implies two major properties, that the quantum harmonic oscillator has discrete energies $E_n = \hbar\omega_m\left(n+\frac{1}{2}\right)$, $n = 0, 1, 2, ...$, and that even in the ground state with $n = 0$ there is a non-zero energy $E_0 = \hbar\omega_m/2$.

2.4.2 Quantum Langevin Equation of a Mechanical Resonator

Similarly to how we defined a quantum Langevin equation of an LC resonator, we can do the same for a mechanical resonator, resulting in

$$m\frac{d^2\hat{x}(t)}{dt^2} + m\Gamma_m\frac{d\hat{x}(t)}{dt} + m\omega_m^2\hat{x} = \hat{F}_n(t). \tag{2.137}$$

Here, the noise spectrum of the Langevin force $\hat{F}_n$ is given by [18]

$$\bar{S}_{F_nF_n}[\omega] = 2m\Gamma_m\hbar|\omega|\coth\left(\frac{\hbar\omega}{2k_BT}\right). \tag{2.138}$$

We can make the same approximation due to the high quality resonator, and simplify the quantum Langevin equation to[18]

$$\frac{d\hat{b}(t)}{dt} + \left(i\omega_m + \frac{\Gamma_m}{2}\right)\hat{b}(t) = \sqrt{\kappa}\hat{b}_{\text{in}}\,(t). \tag{2.139}$$

2.4.3 Effective Mass

While in writing about these systems we treat them as a point mass, there are obviously differences between that point mass and our mechanical elements. We address this by using the methods introduced in [43] to describe how these approximations relate to their real-world counterparts. We can use a scalar field $\rho(\vec{r})$ to describe the solid resonator by describing the density of the resonator at the location $\vec{r}$. Taking the Young's modulus $E(\vec{r})$ at each point as well as the Poisson's ratio $\nu(\vec{r})$ we define an eigenvalue problem to solve for the vibrational modes within the solid, each mode at angular frequency ω_m and with a deformation $\vec{u}(\vec{r})$ indicating the shape (or normalized displacement) of the mode such that the time dependent position of the solid at the undeformed position $\vec{r}$ is given by

$$\vec{u}(\vec{r}, t) = \vec{u}(\vec{r})\cos(\omega_m t). \tag{2.140}$$

We then must relate this deformation to the scalar position coordinate $x(t)$ by choosing a reference position $\vec{r}_0$, and normalizing the displacement field such that we have a vector displacement

$$\vec{x}(\vec{r},t) = \frac{\vec{u}(\vec{r})}{|\vec{u}(\overrightarrow{r_0})|}x(t), \tag{2.141}$$

where $x(t)$ is the equivalent mass on a spring co-ordinate used in this chapter. Then if $x(t) = 1$ nm the mechanical resonator at location $\vec{r}_0$ has displaced along the vector $\vec{u}(\overrightarrow{r_0}) / |\vec{u}(\overrightarrow{r_0})|$ by 1 nm.

We can also determine the potential energy of the mechanical mode by dividing the structure into parts of volume dV such that each component can be approximated by a mass on a spring, such that each such component has potential energy dU given by

$$dU(\vec{r},t) = \frac{1}{2}\rho(\vec{r})dV\Omega_0^2\frac{|\vec{u}(\vec{r})|^2}{|\vec{u}(\overrightarrow{r_0})|^2}x^2(t). \tag{2.142}$$

Integrating this spatially we have

$$\begin{aligned} U(t) &= \frac{1}{2}\int_V dV\rho(\vec{r})\frac{|\vec{u}(\vec{r})|^2}{|\vec{u}(\overrightarrow{r_0})|^2}\Omega_0^2x^2(t) \\ &= \frac{1}{2}m_{\text{eff}}\Omega_0^2x^2(t), \end{aligned} \tag{2.143}$$

where the effective mass is then defined by

$$m_{\text{eff}} = \int_V dV\rho(\vec{r})\frac{|\vec{u}(\vec{r})|^2}{|\vec{u}(\overrightarrow{r_0})|^2}. \tag{2.144}$$

It is important to note that both the position coordinate and effective mass are determined by the choice of $\vec{r}_0$, and the standard convention is to choose a location where $|\vec{u}(\overrightarrow{r_0})|$ is maximal, such that m_{eff} is minimized.

2.5 Theory of Electromechanical Systems

After already deriving the equations of motion for both the LC circuit and the mechanical resonator, we can look at how the systems interact. In most cases, the capacitance of the resonator is altered by the movement of the mechanical element

[45]. For small displacements from equilibrium, the capacitance can be approximated to be linearly related to displacement

$$C_{\rm tot}(x) = C_{\rm tot}(0) + \frac{\partial C}{\partial x}x. \tag{2.145}$$

Then the coupling between the LC circuit and the motion of the mechanical element is given by the capacitive energy shift

$$E_{\rm cap} = \frac{1}{2}C_{\rm tot}(x)V^2, \tag{2.146}$$

which gives rise to a force, the radiation pressure

$$F_{\rm rad} = -\frac{\partial E_{\rm cap}}{\partial x} = -\frac{1}{2}\frac{\partial C}{\partial x}V^2. \tag{2.147}$$

We then have two coupled nonlinear equations from eq. (2.124) and eq. (2.28) which govern our system

$$C_{\rm tot}(x)\frac{d^2\Phi}{dt^2} + \frac{1}{Z_0}\frac{d\Phi}{dt} + \frac{\Phi}{L} = I_n(t) + I_d(t), \tag{2.148}$$

and

$$m\frac{d^2x}{dt^2} + m\Gamma_m\frac{dx}{dt} + m\omega_m^2 x = F_n(t) - \frac{1}{2}\frac{\partial C}{\partial x}[V(t)]^2. \tag{2.149}$$

where if you recall, $I_n(t)$ is the noise current, $F_n(t)$ is the Langevin force from mechanical dissipation, and $I_d(t)$ is the drive current.

Given all that, we can determine the output voltage of the system's transmission line to be

$$V_{\sigma,\,\rm out}(t) = V_{\sigma,\,\rm in}(t) - Z_\sigma I(t), \tag{2.150}$$

where the time dependent current is given by

$$I(t) = \sum_{\sigma=\rm int,in,out}\left(\frac{2V_{\sigma,\,\rm in}(t)}{Z_\sigma} - \frac{V(t)}{Z_\sigma}\right). \tag{2.151}$$

Sadly, there is no analytic solution in general for these equations; only in approximations can we find any solace. Using the approximations for the quantum Langevin equations in the previous sections, we can explore this system in greater depth.

2.5.1 Quantum Langevin Equations of an Electromechanical System

Similarly to previous sections, we find our initial quantum Langevin equations by inserting quantum operators into eq. (2.148) and eq. (2.149), giving

$$\frac{d^2\hat{\Phi}}{dt^2} + \frac{1}{Z_0 C_{\text{tot}}(\hat{x})}\frac{d\hat{\Phi}}{dt} + \frac{\hat{\Phi}}{LC_{\text{tot}}(\hat{x})} = \frac{1}{C_{\text{tot}}}\left[\hat{I}_n(t) + I_d(t)\right], \tag{2.152}$$

and

$$m\frac{d^2\hat{x}}{dt^2} + m\Gamma_m\frac{d\hat{x}}{dt} + m\omega_m^2\hat{x} = \hat{F}_n(t) + \hat{F}_{\text{rad}}(t) \tag{2.153}$$

Note that we've included the drive current $I_d(t)$ into our equations. Likewise, we include the radiation pressure of the cavity field as given by

$$\hat{F}_{\text{rad}}(t) = -\frac{1}{2}\frac{\partial C}{\partial x}[\hat{V}(t)]^2. \tag{2.154}$$

Because we make the same approximations as we did individually for both the resonators, we have the simplified equations with external drive field[3] $\alpha_{\text{in}}(t)$,

$$\frac{d\hat{a}(t)}{dt} + \left[i\omega_0(\hat{x}) + \frac{\kappa}{2}\right]\hat{a}(t) = \sqrt{\kappa}\left[\hat{a}_{\text{in}}(t) + \alpha_{\text{in}}(t)\right], \tag{2.155}$$

and

$$\frac{d\hat{b}(t)}{dt} + \left(i\omega_m + \frac{\Gamma_m}{2}\right)\hat{b}(t) = \sqrt{\kappa}\hat{b}_{\text{in}}(t) + i\frac{x_{\text{zp}}}{\hbar}\hat{F}_{\text{rad}}(t). \tag{2.156}$$

We also ignore the position dependence of κ as it is much smaller compared to ω_0. We can then define our electromechanical coupling,

$$g_0 = -\frac{\partial\omega_0}{\partial x}x_{\text{zp}} = \frac{\omega_0}{2}\frac{1}{C_{\text{tot}}}\frac{\partial C}{\partial x}x_{\text{zp}}. \tag{2.157}$$

When we expand to first order in $\omega_0(\hat{x})$ we get the quantum Langevin equation

$$\frac{d\hat{a}(t)}{dt} + \left(i\omega_0 + \frac{\kappa}{2}\right)\hat{a}(t) - \sqrt{\kappa}\hat{a}_{\text{in}}(t) = \sqrt{\kappa}\alpha_{\text{in}}(t) + ig_0\left[\hat{b}(t) + \hat{b}^\dagger(t)\right], \tag{2.158}$$

and

$$\frac{d\hat{b}(t)}{dt} + \left(i\omega_m + \frac{\Gamma_m}{2}\right)\hat{b}(t) - \sqrt{\kappa}\hat{b}_{\text{in}}(t) = ig_0\left[\hat{a}^\dagger\hat{a}(t) + \frac{1}{2}\right]. \tag{2.159}$$

[3]For cavities with multiple ports, $\sigma = 1, 2, 3...$ we have $\hat{a}_{\text{in}}(t) = \sum_\sigma \sqrt{\frac{\kappa_\sigma}{\kappa}}\hat{a}_{\sigma,\text{in}}(t)$ and $\alpha_{\text{in}}(t) = \sum_\sigma \sqrt{\frac{\kappa_\sigma}{\kappa}}\alpha_{\sigma,\text{ in}}(t)$

We're done, thankfully; just one final note before we can close out this section. The static term $1/2$ in the equation above is the static radiation pressure from the quantum fluctuation of the cavity field and will not have any dynamical effect on the system. As such, we will agree to throw it out in future discussions, where both of us will be too polite to mention it.

Chapter 3

Sample Package

3.1 Sample Package Simulation

As opposed to testing 3D microwave devices, where one need only connect an SMA antenna of the approximately correct length to the bulk cavity, the design of package holders for on-chip microwave devices is considerably more complex. The wiring on the fridge is often similar, but rather than emitting the signal into the free space of the cavity one must couple it to transmission lines, which then connect to the device on the test chip.

The input and output lines are traditionally connected to push-mate SMP connectors, where the male connector is soldered to a transmission line on a PCB. Traditionally for microwave applications bare copper PCBs are used, as they have excellent conductive properties in the microwave bands and at low temperatures where such chips are generally tested. Then, as mentioned in section 2.2.3, the major concern is loss in the dielectric media used for the PCB.

Numerous dielectrics suitable for low-temperature microwave applications have been designed. Not only do they generally have small dielectric loss tangents at cryogenic temperatures, but they also have similar coefficients of thermal expansion to copper over the temperature range of interest; this reduces internal stresses during cooling which can lead to delamination.

Even given these necessary characteristics, as well as impedance matching techniques

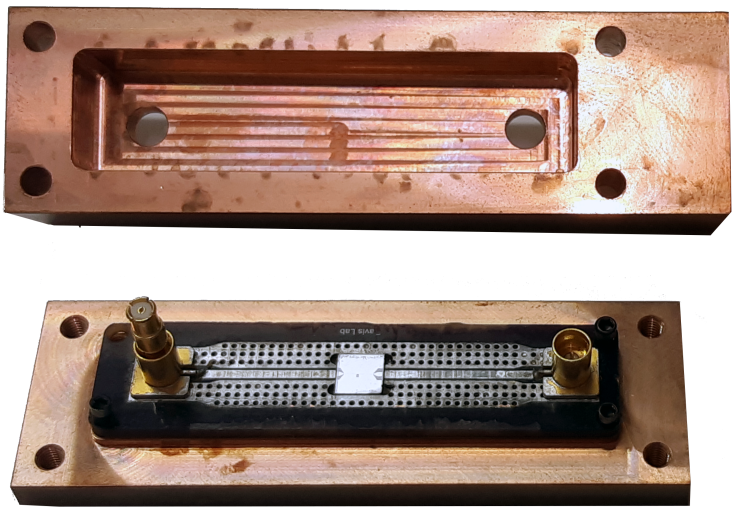

Figure 3.1: Image of first cavity design with generic PCB, with hole milled into PCB to deposit chip.

discussed in chapter 2, there are a great variety of designs available for these microwave packages. We will discuss their design and simulation in this section, while the test chips themselves will be discussed in chapter 4.

3.1.1 Initial Package Design

The simplest design for microwave packages, and the one that most end up in, is known as the coffin design. It consists of a long rectangular cavity with a single transmission line along its center, with two SMP connectors tacked to either side of the line for readout in transmission. Following the design presented in [46] a basic coffin layout was considered.

Material choices were also limited; when the project began, sourcing printed circuit boards to wirebond to the fabricated chips was the primary concern. Dielectric materials suited to low temperature, high-frequency measurement was generally provided by companies who primarily targeted industrial projects with minimum prices and orders exceeding the needs of the project. Initial concerns about pricing led to initial testing with generic printed circuit boards from sources previously used in the lab

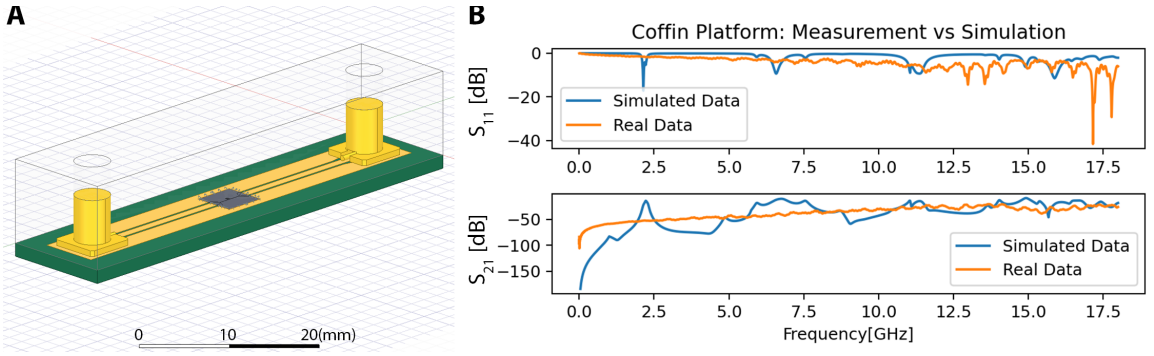

Figure 3.2: A: HFSS simulation of initial coffin cavity, ENIG gold in yellow, FR-4 in green.
B: Comparison of simulated to measured package response, performed in HFSS.

fabricated on lossy FR-4 substrates.

This is in itself problematic for simulations; FR-4 is not a specific material of given properties. FR-4 is actually a class of composite materials composed of woven fiberglass cloth with an epoxy resin binder as described by the National Electrical Manufacturers Association [47]. Actual material characteristics can vary widely between manufacturers, particularly at higher (GHz) frequencies. Characteristics used in the simulation were taken from industry averages as recorded in Ansys HFSS.

This led to the design of the early boards being limited in scope by what these inexpensive PCB fabrication services could provide, that being FR-4 substrates with metals that are lossy in the GHz regime. The design for the earliest tests is shown in fig. 3.1 and as can be seen, the trace was coated in electroless nickel immersion gold plating, with a cutout for the chip and screws. The PCB was contained within a copper coffin-style cavity, and the PCB was wire-bonded to the chip using 33 μm aluminum wedge-wedge bonds. The original simulation failed to account for reflections due to the discontinuities in the line and the wire bonds, which was addressed by fully simulating it in HFSS post-mortem as seen in fig. 3.2. It can also be seen that in practice, reflections were more pronounced than transmission even in the best-case scenario. A local cavity loss in transmission of $\approx$ 50 dB is overall consistent with the measured response, with the differences in transmission being minor. It is inter-

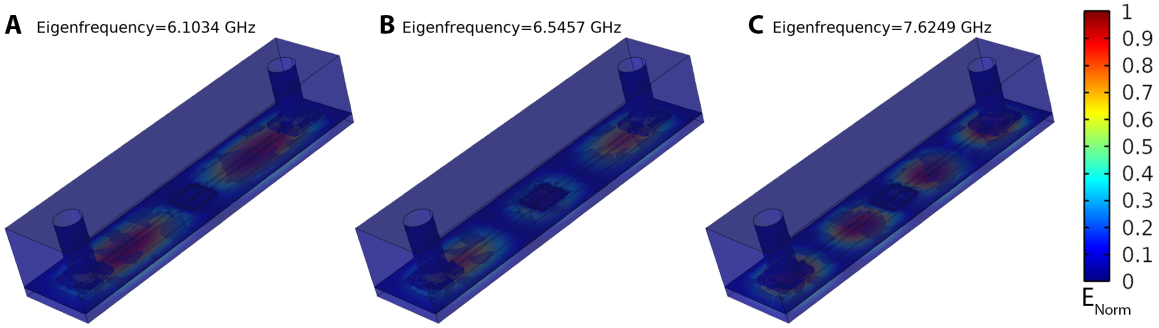

Figure 3.3: Simulation of parasitic cavity modes in COMSOL. Magnitude of excitation normalized to maximum of all sub-figures, in units of V/m.

esting to note that the uninterrupted ground plane of the PCB acted as a capacitor allowing plate modes to form within the dielectric as shown in fig. 3.3. The simulated dips in reflection align to the plate modes in the 5 to 8 GHz regime, though further simulations have not been conducted. As we will discuss in later sections, the first coffin cavity proved to be too lossy for any measurements of on-chip resonators to be performed. However, it still did provide a basis to attempt to zero in on parameters for the newly grant acquired TPT wire bonder, and for developing early measurement scripts.

3.1.2 Revised Coffin Design

While there were many issues associated with the initial coffin design, we decided after considering the recommendations in the literature that the primary issue was likely the poor electrical properties of the FR-4 substrate. At this point, we determined that it would be better to seek out PCBs made from low-temperature compatible, low-loss dielectrics with bare metal traces. Pricing and order sizes still proved to be an issue, however. At this point, we contacted Omni Circuit Boards Ltd., who responded to our hesitancy to meet the required minimum order by offering castoffs from previous projects so that we could determine if the boards would meet our needs. The boards were fabricated from Rogers 6010 ceramic dielectric with aluminum traces and copper

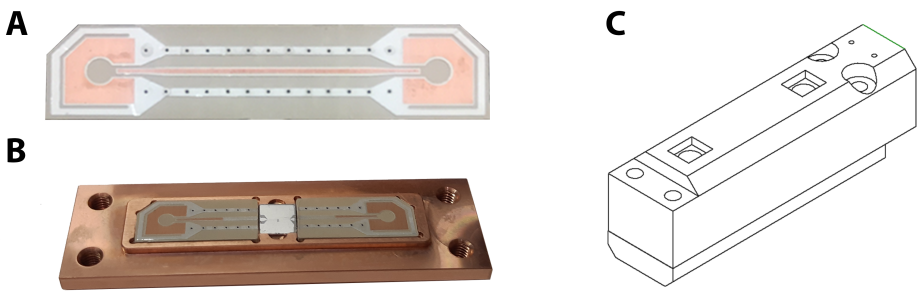

Figure 3.4: a: The aluminum/copper PCB provided by Omni Circuitboards. b: Image of the copper cavity designed to hold the PCB and chip. c: Schematic of the cavity including the lid, designed to sit vertically on a fridge with a round chamber 40 mm in diameter.

bond-pads. We designed and machined a more compact coffin-style cavity to house the PCBs, though as the boards did not contain a cutout for the chips, boards were instead cleaved using a razor, with the chip housed between the two halves as seen in fig. 3.4.

At this point, upon recommendation from an industry contact met during a Quanta Create workshop, we began to simulate packages in the Ansys HFSS software suite. Rather than modeling systems as transmission lines as with Keysight ADS, HFSS is a Finite Element Modelling software. In this system, the entire cavity, as well as the trace, are modeled. Due to high industry adoption, microwave electronics manufacturer Amphenol also makes models of their SMP connectors available which are modeled to act as ports with the correct impedance and waveform.

After choosing a center frequency around which the system will be swept, HFSS then begins to mesh the geometry. This is when the system geometry is broken into discrete polygons, with the simulation determining the field based upon boundary conditions at each frequency at each vertex of the polygons. Thus, a simulation with a greater polygon count will be more computationally intensive; however, if the polygons are not distributed finely enough particularly in areas of interest such as transmission lines and resonators the software will not be able to accurately model mode shapes of resonances.

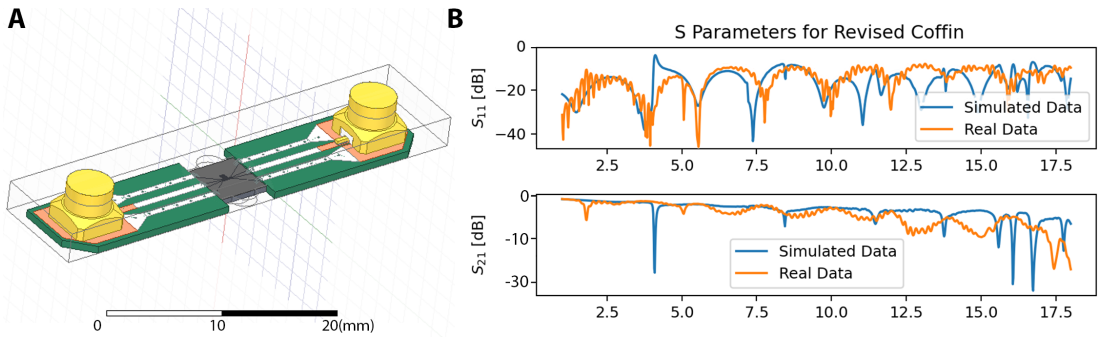

Figure 3.5: A:FEM simulation of the second platform modeled in Ansys HFSS. B:Comparison of data measured using the revised launch cavity at room temperature with dummy chip containing only a 50 Ω transmission line. Simulation created in Ansys HFSS software. Differences between simulation and measurement discussed in body of text.

To this end, HFSS meshes designs iteratively. It begins with a relatively coarse mesh and simulates the field at the center swept frequency. Then it increases the density of the mesh in areas with rapidly changing fields or dense geometry and repeats the simulation. It does this for either a set number of refinements or until the field profile changes less than a set proportion given as a threshold; in this manner, areas of less interest can be modeled more coarsely, while areas of interest or thin geometry are not overlooked.

This new PCB design, having traces made of aluminum, would also superconduct at the base temperature of the fridge. To account for this, the aluminum traces were modeled as perfect electric conductors. While this would not account for the kinetic inductance or the power-dependent heating of the device, it was hoped that this would not prove problematic as we were not at liberty to alter the design of the PCB. Overall the simulations align very well to the measurement as seen in fig. 3.5. The differences here are likely due to the changes in the dielectric properties of the substrate due to temperature not being fully modelled in the simulation, resulting in a shift in the effective path length from the changing dielectric constant.

Unfortunately, several factors contributed to this design making it a less than ideal platform. The cleaving of the boards proved destructive to the traces, bending the

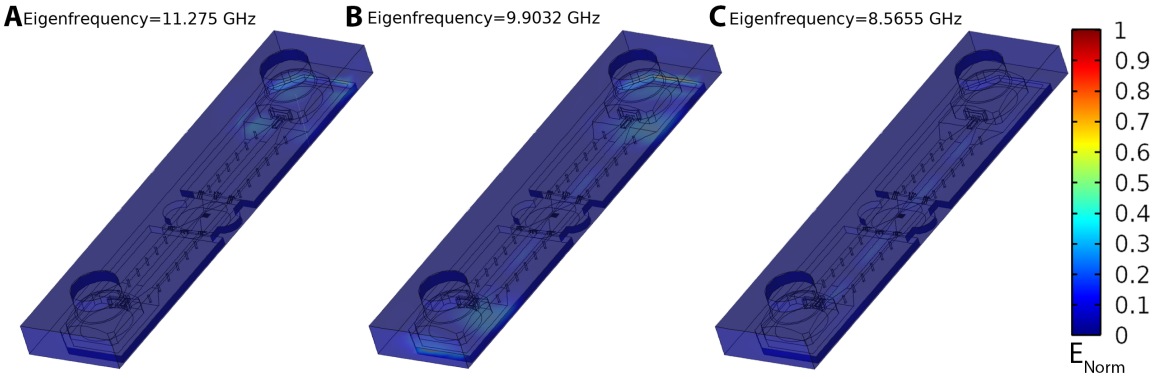

Figure 3.6: Simulation of parasitic cavity modes in COMSOL. Magnitude of excitation normalized to maximum of all sub-figures, in units of V/m.

trace near to the boundary with the chip, which caused wire-bonding to be unreliable. Additionally, the traces themselves were fabricated from relatively thin aluminum, which was degraded by repeated wire-bonding as different chips were inserted and bonded. While excellent for single bonds, the removal of the bonds left marks that would impede subsequent bonding, and the thin traces were unsuitable for polishing to remove remnant marks. There is also the issue of impedance mismatch; our RF components, SMP connectors, and chips were designed to the standard 50 Ω impedance used in academic settings while the boards had been designed to the common industrial 70 Ω standard, leading to lower throughput and increased reflection. Simulations of the cavity transmission show strong agreement to the observed issues with transmission, indicating that the faults as simulated are indeed responsible for the issues; this comparison can be seen in fig. 3.5.

Initial tests proved more promising than the previous design, with overall transmission higher than in the previous design. Performance still did not meet the desired quality, however, and due to the difficulty in repeated wire-bonding onto the transmission line surface after cleaving, a more traditional bare copper PCB was produced for the next generation of devices.

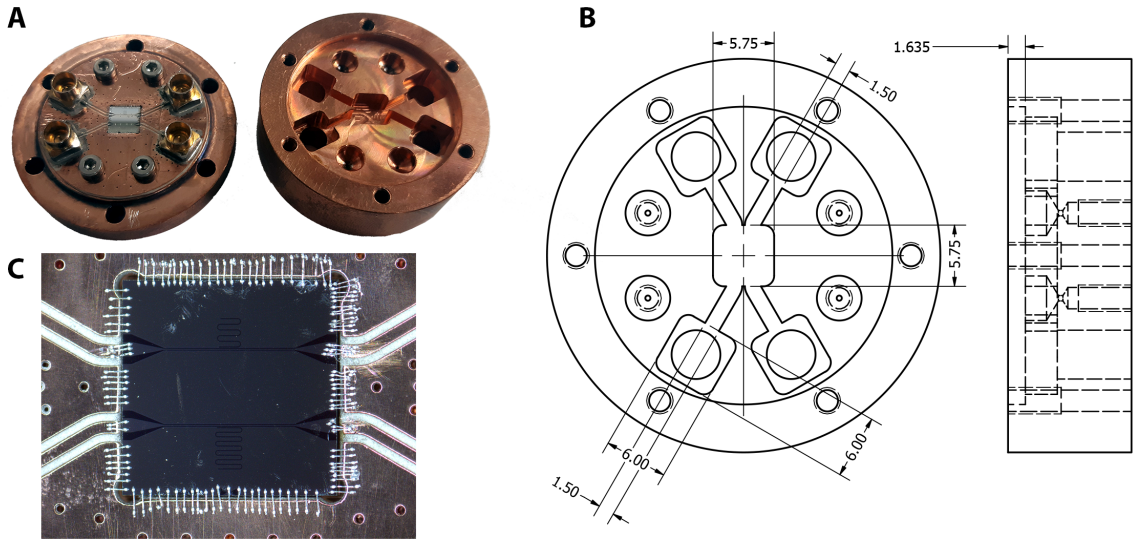

Figure 3.7: A: Image of package with chip wirebonded to platform.
B: Schematic showing relevant dimensions of package volume.
C: Close-up of chip wirebonded into cavity.

3.1.3 Round Cavity Design

Given the difficulties associated with the previous platforms, it was decided a more thorough design process would be necessary to create a reusable platform for broadband measurement. While platforms for cryogenics testing have been designed for frequencies up to 116 GHz, they are designed for temperatures of 4-100 K and don't account for the limited cooling power of pulse tube or dilution cooling units [48]. Additionally, an ideal sample holder should not only provide an RF connection from the on-chip device to a coaxial cable but also suppress parasitic, or unwanted, resonances. The transmission lines should therefore be single-mode, as reflection and transmission coefficients only make sense within that framework. If a higher-order mode can propagate then it can excite parasitic resonances; then the excitation of higher mode may occur due to small irregularities or asymmetries in the circuit, from manufacturing or assembly issues, which ultimately reduces quality factors[18, 46, 49].

As has been done previously, the sample holder will be fabricated from oxygen-free high conductivity copper both for its conductive properties and its high thermal con-

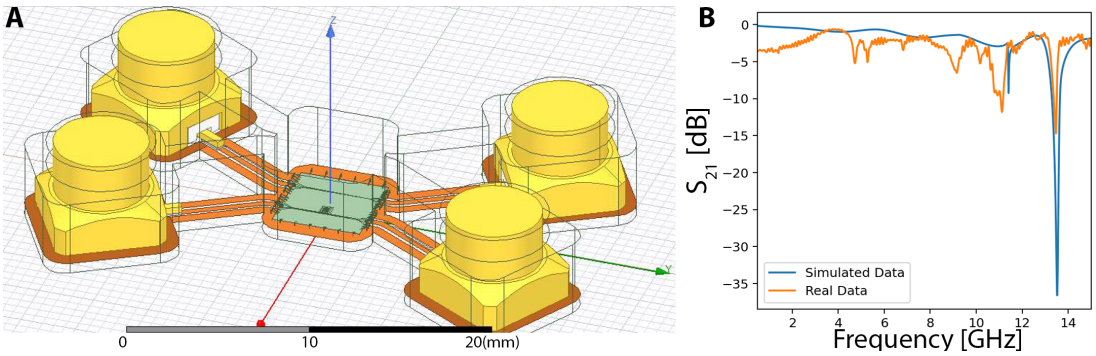

Figure 3.8: A: HFSS simulation of round cavity design. Orange sheet is shell element copper layer.
B: Comparison of transmission in simulation vs room temperature measurement.

ductivity. Additionally, the footprint of the device must be small, as some of our fridge units have a cylindrical volume of only 40 mm in diameter.

Having determined the sourcing of our next PCB, we determined that the dielectric would be Rogers RO3010, a ceramic with dielectric constant $\varepsilon_r = 10.2$ and a loss tangent of only $\tan\delta = 0.0035$. The conduction layers would be made from 1/2 oz. rolled copper with metalized vias. This was provided by Sunstone Circuits Printed Circuit Boards.

Then in order to suppress higher-order modes, we must reduce the cross-sectional area along the propagation direction of the waveguides. This will be accomplished by an array of vias along the sides of the PCB transmission line as well as a rectangular channel in the sample holder along the cavity. As a rule, if via spacing along the sides of a transmission line is less than $\lambda/20$ you can consider the transmission line to be fully isolated [50]. In a narrow channel, we can assume signals will propagate as if it were a rectangular waveguide of width a. This allows us to suppress transmission under the cut-off frequency

$$f_{\text{cutoff}} = \frac{c}{2a\sqrt{\varepsilon_{eff}}}. \tag{3.1}$$

As the wave being suppressed primarily propagates not in the PCB but in the channel, it has an effective dielectric constant ε_{eff} near to unity. Then by reducing channel size to 1.5×3 mm^2 we cut off any waveguide modes under 50 GHz, well above the

18 GHz our VNA can measure, as shown in eq. (3.1).

As our standard chip size, the smallest that could be used in optical lithography at the time was 5×5 mm. To wire-bond the chip to the PCB without crushing any bonds, a 5.75×5.75 mm chamber was left over the chip face. Approximating to the first-order, we can treat this chamber roughly as a rectangular microwave cavity of width and length d and l, with the lowest resonant frequency of

$$f_{min} = \frac{c\sqrt{d^2 + l^2}}{2dl} \tag{3.2}$$

or 36.9 GHz, again well above the 18 GHz upper limit of our VNA. While the chamber openings increase the effective volume to some degree, it is still well above the range of interest.

In addition to standard modeling techniques, the copper traces on the PCB were modeled as shell elements. Rather than treating it as a conductor of infinite thickness, often layers of thin metals are replaced by a sheet impedance boundary condition. This model holds when the field decays quickly to zero within the layer. For thinner layers such as the PCB where the field may not decay to zero within the depth of the film the shell element allows the simulator to treat these thinner layers without the need to densely mesh the region, saving on calculation time [51].

The field relationships on either side of the thin sheet can be given by

$$\begin{bmatrix} \mathbf{n} \times \mathbf{H}_{t1} \\ \mathbf{n} \times \mathbf{H}_{t2} \end{bmatrix} = \begin{bmatrix} y_{11} & y_{12} \\ y_{21} & y_{22} \end{bmatrix} \begin{bmatrix} \mathbf{n} \times \mathbf{n} \times \mathbf{E}_{t1} \\ \mathbf{n} \times \mathbf{n} \times \mathbf{E}_{t2} \end{bmatrix} \tag{3.3}$$

wherein the frequency dependent y matrix characterizes the layer with normal vector at the surface $\mathbf{n}$. This can be used in a closed analytical in using a transmission line model, or in numerical form as implemented here by linking to a FEM unit cell modelling the layer. Then the finite element polyhedra on each side, $\Gamma_{1,2}$ can be

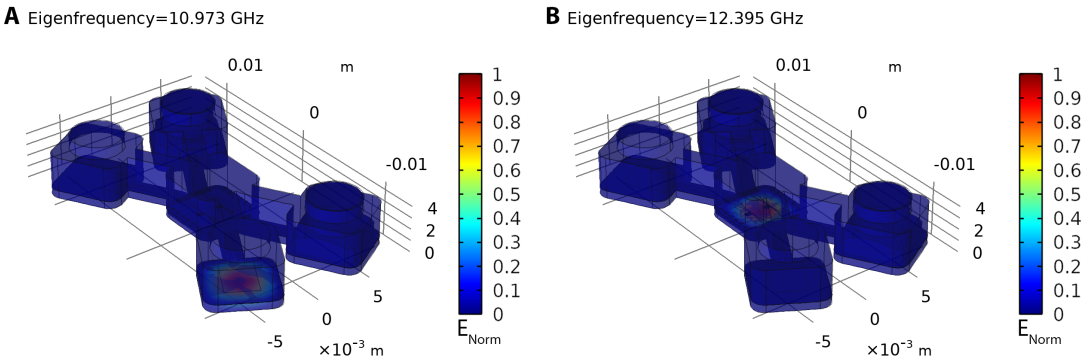

Figure 3.9: Simulation of parasitic cavity modes in COMSOL. Magnitude of excitation normalized to maximum of all sub-figures, in units of V/m.

accurately modelled with the additional boundary conditions

$$\begin{aligned}
&\int_{\Gamma_1} \mathbf{E}_1^* \bullet (\mathbf{n}_1 \times v_r \operatorname{curl} \mathbf{E}_1)\, d\Gamma = \\
&- j\omega\mu_o \int_{\Gamma_1} (\mathbf{E}_1^* \bullet (\mathbf{n}_1 \times (y_{11}\mathbf{n}_1 \times \mathbf{E}_1) + (y_{12}\mathbf{n}_1 \times \mathbf{E}_2))\, d\mathrm{I} \\
&\int_{\Gamma_2} \mathbf{E}_2^* \bullet (\mathbf{n}_2 \times v_r \operatorname{curl} \mathbf{E}_2)\, d\Gamma = \\
&- j\omega\mu_o \int_{\Gamma_2} (\mathbf{E}_2^* \bullet (\mathbf{n}_1 \times (y_{22}\mathbf{n}_2 \times \mathbf{E}_2) + (y_{21}\mathbf{n}_2 \times \mathbf{E}_1))\, d\Gamma
\end{aligned} \tag{3.4}$$

where $E_{1,2}^*$ are weighting functions used in the FEM Galerkin method of weighted residuals [52]. In this way the shell element models similarly to a finite impedance method, with an additional boundary condition. The coupling between the two sides is via the y_{21} and y_{12} terms, giving an additional degree of freedom to the electric field on the surface.

As can be seen in fig. 3.8 these methods provide very accurate results when compared to physical measurement. The observed additional drops in fig. 3.8 at 10 GHz and 12 GHz respectively can be partially explained through additional modelling of the sample holder as seen in fig. 3.9. The top and bottom copper plating of the PCB provides areas without vias such as under the SMP connections to excite plate modes at roughly 10 GHz. The higher dielectric constant of the silicon chips, with the top conducting layer and copper surface of the cavity to be excited near to 12 GHz. These ultimately limit the performance of the cavity.

Chapter 4

Chip Design: Simulation and Fabrication

One of the primary concerns in designing any future electromechanical systems is that of the substrate. There have been many prior experiments that have sought to determine ideal substrate choices for high-quality microwave resonators [30, 53]. The two commonly selected materials with robust histories of implementation are sapphire substrates, which possess the higher raw quality factors [54, 55], and high-resistivity silicon [56], which are generally chosen for their ease of fabrication and compatibility with more traditional circuit technology [57]. We will test both substrate options, though high-resistivity silicon is considered more favorable for reasons to be discussed later.

One must also choose a superconducting metal to create the devices from; for this our selection has been made easier by availability. The common choices are aluminum which is chosen for its long-term stability and self-limiting oxide [58], and niobium which is chosen for its higher critical temperature [59]. When patterning a metal film in a lift-off fabrication process with critical dimensions in the tens of microns it is preferable to use electron beam evaporation to deposit the metal [57] as sputtering leaves a film of much higher roughness, leading to loss. As the local nanoFAB cannot conduct electron beam evaporation of niobium, we elected to use aluminum as a metal layer.

As discussed in section 2.2.4 chips would be designed in what is known as a notch configuration which allows for relatively weak resonator-feedline coupling without significant perturbations to the propagating modes in the feedline CPW [60]. In this case, the chip will consist of a large and robust feedline, a CPW wire-bonded to the pin and ground planes of the package, and a smaller more sensitive resonator coupled to the feedline along its side.

In this configuration, the external quality factor depends not only on the design of the resonator itself, but also on the port impedances and the coupling elements, be they inductive [61], capacitive [62], or both [55].

When designing chips more physical constraints also had to be considered. When fabricating chips, the smallest chip that could be processed using optical lithography was 5×5 mm and so we considered that to be our canvas for the exercise. As wire bonds add significant loss at greater lengths it was considered all chips should be designed to equal size, so they could fit flush to the package PCB.

With all these characteristics and limitations in mind, we will begin to discuss the iterations of chip design.

4.1 Simulation in Chip Design

4.1.1 On the Choice of Simulation Software

While in an ideal case all electromagnetic solvers would solve for the same possible fields, and thus make choice of solver irrelevant, this is not the case. While well modeled simulations will usually return the same result, the required computational power and available boundary conditions can vary widely between solvers. Two main electromagnetic simulation software suites were used during this work, COMSOL and Ansys HFSS, and it would be best to analyze when and why they were implemented. COMSOL is a solver that integrates everything from mechanical simulation to optical band simulation, fluid modelling, and thermomechanical modelling. Meanwhile,

Ansys HFSS is designed entirely to solve DC to GHz electromagnetic problems, and this allows for the workflow to be streamlined with that in mind.

Meshing, the method through which the geometry of the problem is transformed into a mesh of nodes at which the field is solved, in COMSOL is not as tuned for circuit simulation as in Ansys HFSS. In order to to capture the detail of a planar resonator, meshing was begun by a dense, 2D triangulated mesh on the resonator of interest. Then the mesh for the surrounding ground plane was meshed at a lower resolution, where finally the 3D substrate and air were forced to accommodate the dense mesh on the interface while being allowed to transition to a loose tetrahedral mesh in the far-field to save on simulation time. This was all done manually, and thus any areas of particularly dense field evolution could be undermeshed, while oftentimes areas were meshed more densely than required to model the solution, wasting processing power. This means that for systems with high-aspect ratios, such as planar resonators, there are large areas of the field being meshed inefficiently.

Meanwhile Ansys uses iterative meshing[63]. Beginning with a rough mesh, with initial node spacing set to be a given fraction of the wavelength simulated, via a method known as lambda refinement. Lambda refinement is the process of refining the inital mesh such that all tetrahedra are smaller than a certain fraction of the wavelength. It provides a minimum mesh density over all objects. The reference wavelength is related to the desired solution frequency in terms of wavelength in the used dielectric media. The mesh is then refined iteratively by refining areas and seeing the degree to which the solution is affected, with a given threshold of what changes are considered significant.

In addition, Ansys allows for unique boundary conditions such as shell elements[64]. Rather than treating a thin metallic layer as a conductor of infinite thickness, often layers of thin metals are replaced by a sheet impedance boundary condition. This model holds when the field decays quickly to zero within the layer. For thinner layers such as the PCB where the field may not decay to zero within the depth of the film

the shell element allows the simulator to treat these thinner layers without the need to densely mesh the region, saving on calculation time [51].

It is for these reaons that simulations were often done in Ansys HFSS rather than COMSOL. However, the data visualization in HFSS is less advanced than in COMSOL, so often for plots of fields included in this thesis they were re-simulated in COMSOL both to confirm the simulation results, and to provide cleaner figures.

4.1.2 Early Compact Resonator Design

Initially, we set out to duplicate the results of one of the most impressive microwave cavity interferometers yet produced, one with noise below that of the standard quantum limit [7]. Though never having produced on-chip microwave devices before, we had initially assumed fabrication and measurement to be the less integral parts of the development process. While incorrect, it did provide a task to attempt that allowed us to develop many of the basic methods used in this report.

The devices consisted of an aluminum resonator patterned in a notch geometry from a CPW feedline. The resonator itself was not a CPW meander as in previous works [15] but rather a compact meandering microstrip line. The core design philosophy of this device was to allow a mechanical element to modulate as much of a microwave circuit's capacitance as possible; therefore they reduced the total capacitance of the system and placed the mechanical element in an electric field maxima.

This design is more difficult to model than the meandered CPW line. When so much of the capacitance in the system is not due to the properties of the transmission line but to the mutual self-capacitance of the model traditional transmission line models break down and the system must be modeled in FEM software.

COMSOL then used a linear system solver (the Pardiso solver [65]) to solve for eigenfrequencies of the system as $A - \sigma B + \zeta^2 C = 0$ where A, the system matrix, is the Jacobian (stiffness) matrix, B is the damping matrix, and C is effectively the mass matrix, where ζ is the shift — that is, the number around which the software searches

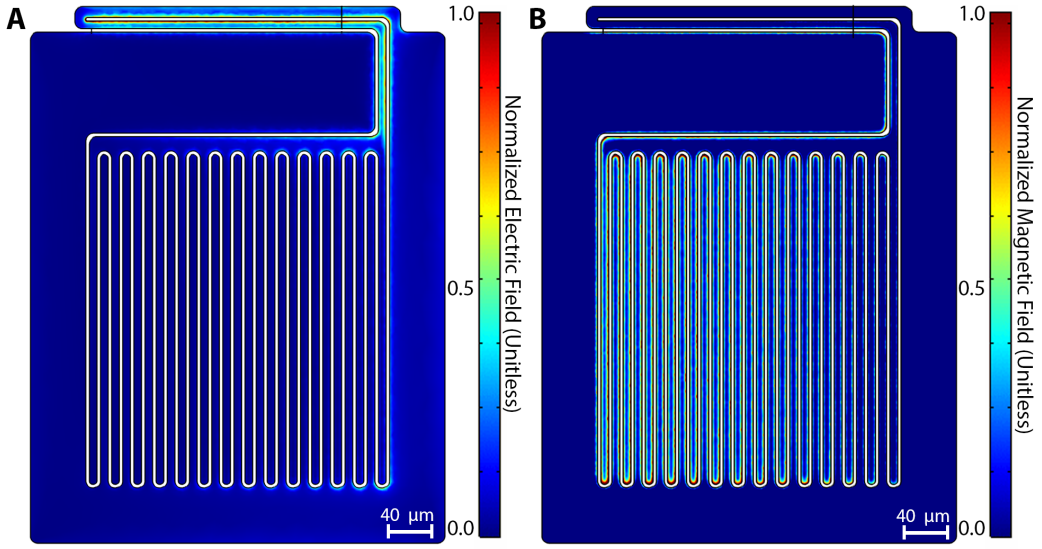

Figure 4.1: COMSOL simulation of early compact resonator, resonance at 8.5 GHz. Electric field distribution shown in A, magnetic field shown in B.

for eigenvalues, and returns only those solutions that are positive-definite.

The COMSOL simulation of the field distribution in the mode of interest (the quarter wavelength resonance) is shown in fig. 4.1.

Unfortunately, while the design of these chips formed the basis for the early part of the project (when we were using coffin-style microwave chip platforms) we did not succeed in measuring the devices to compare results to the simulations. Because the capacitance of these devices is very low, the electric field concentration is greater, which may cause the resonator to drive at a local field intensity great enough to cause the film to transition into normal conduction when measured at a high photon number; as we did not have a HEMT or JPA, but only room temperature amplification, we measured at powers much higher than those reported in the original work.

After a lack of success with early devices on the first two coffin-style platforms, we sought to return to an easy, analytically designed platform and began to work with more traditional CPW resonators. It is possible that if one of these devices was fabricated for the round platform a resonance signal would be visible.

As these meandering microstrip resonators were tested early in process development

it is also possible that mentioned fabrication defects (see section 4.2) were impactful enough on these devices that all measured devices had a warped dimension, as these devices lie in the low-resolution limit of the available optical lithography systems.

4.1.3 Quarter Wavelength CPW Resonators

As opposed to the first attempted design, the quarter wavelength CPW resonators have a great wealth of analytic solutions for estimating wavelength and quality factor, as seen in chapter 2. They were modeled in Ansys HFSS using the frequency-dependent impedance boundary condition described in section 2.3, although spatial field profiles within this thesis have been modeled and displayed in COMSOL as the program has better data visualization capabilities.

The quarter wavelength CPW resonator is made up of the coplanar waveguide it is named for, as described in section 2.2. As discussed previously, microwave waveguides allow a signal made up of alternating electric and magnetic fields propagate along the waveguide. As they do so, the signal evolves in phase as it travels through the waveguide, which also then allows for standing waves to form.

The easiest such wave to visualize is one with matching boundary conditions on each side, the half-wavelength resonator. In this, the pin of the CPW is connected to ground on each end of a length of CPW, with the total length of the CPW forming a half wavelength in the effective dielectric constant ϵ_{eff}, as given in eq. (2.83). With the pin shorted to ground on each side, no electric potential can be formed to ground, so the electric field maxima is at the center, with minima on each side. Conversely, the current density is maximized at the shorted pins, and minimized at the center. In this way, a half wavelength resonator is the same as the string on a guitar; the electric field being the kinetic energy of the moving string, clamped at the edges, with potential energy stored at the clamping points pulling the string back to center.

The quarter wavelength defies explanation via guitar analogies, but the same principle

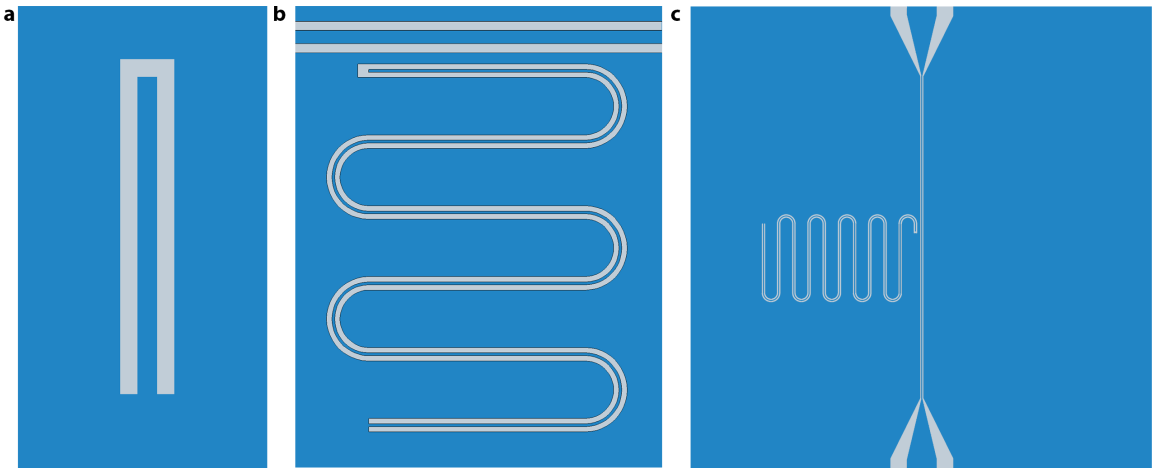

Figure 4.2: a: A simple schematic of an un-meandered CPW quarter wave resonator. b: A meandered quarter wavelength CPW resonator, notch coupled to a larger feedline running along the top of frame, from which the signal couples into and out of the resonator as described in section 2.2.
c: A cartoon showing the layout of a 5×5 mm chip showing the relative position and size of both the central feedline and resonator.

applies. Here, one end of the CPW is shorted to ground, while the other is "open", ending without directly connecting to another conductor as pictured in fig. 4.2a. Here the electric field is greatest at the open, and the magnetic field around the other side (the shorted pin). Then the waveguide is resonant at a quarter wavelength within a medium of ϵ_{eff}. If one reaches for physical analogy, here this is the doorstop; the free end able to vibrate, while the end attached (or shorted) to the wall has the potential energy maximized.

All quarter wavelength CPW resonators studied here follow this design, with the only difference being that they meander, curving along their length, as shown in fig. 4.2b. This is not for any deep reason, rather it saves on the space on chip, allowing longer waveguides to be fabricated. The resonator is coupled to a central feedline as discussed in section 2.2 and shown in fig. 4.2c. **Mk 1 Resonators**
Initially, to circumvent low yield fabrication processes each chip was designed with two transmission lines with an identical resonator. It was thought that in the final

iteration, now having access to two feedlines in the round cavity configuration, that one line might be used with a mechanical element with the other a resonator without a mechanical element. This would allow us to see if any issues in the quality of the resonance may be caused by the mechanical element or some other fabrication issue. The first generation of these quarter-wavelength resonators were designed with pin width $a = 5$ μm, gap $s = 7.5$ μm, and $t = 150$ nm. This gives an impedance of $Z_0 = 65$ Ω not accounting for mutual self-capacitance and inductance from the meander. This not only decreases the coupling to the feed line, increasing Q_i, but allows the system to sit at a minimum in the derivative of the frequency shift in eq. (2.89). In this way, using eq. (2.90) we set our geometry such that the limit to the quality factor is $1/Q^a \approxeq 10^{-6}$ such that a cavity with quality factor 1,000,000 would be critically coupled. This was the only consideration in the spacing between the feedline and the resonator. In this context, a critically coupled resonator is one that allows maximum energy transmission from feedline to cavity, or when $Q_{in,out}$ from eq. (2.39) perfectly matches the internal quality factor of the resonator, giving a minimum in $S_{21}(\omega)$ as seen in eq. (2.105).

These resonators were simulated to have center frequencies of $f_0 = 8.625$ GHz with $Q_i = 56,402$ using the impedance boundary conditions described in section 2.3. The design patterned onto the chips can be seen in fig. 4.3, along with the simulated resonance profile.

Mk 2 Resonators

To increase the data gained from limited fridge time, we designed these resonators to be multiplexed. This describes resonators in a notch configuration sharing the same feedline, at differing frequencies. The $f_0 = 8.625$ GHz resonator was the same as in Mk 1, with the additional resonator of the same transverse dimensions and coupler length, but with longer length giving center frequency $f_0 = 4.603$ GHz and was simulated to have $Q_i = 118445$.

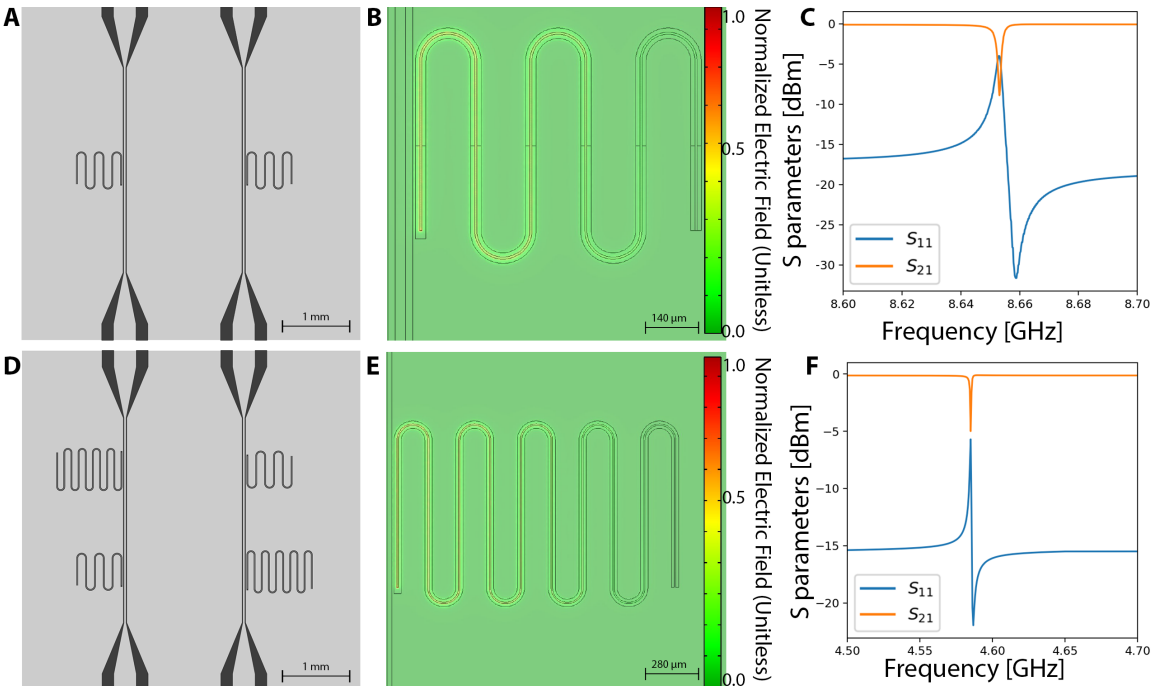

Figure 4.3: A: Mk 1 chip layout, aluminum in light grey with silicon in dark. B: 8.65GHz electric field profile, displayed in COMSOL. C: Simulated S parameters for 8.65 GHz resonator.
D: Mk 2 chip layout, aluminum in light grey with silicon in dark. E: 4.65 GHz electric field profile, displayed in COMSOL. F: Simulated S parameters for 8.65 GHz resonator.

Additionally, when designing the MK 1 chips the patterns had exported with lower curve resolution such that curves were made from straight segments of $\approx 5\ \mu m$. While the design of the 8.65 GHz resonator was otherwise unchanged, the curve resolution was fixed before Mk 2. The design patterned onto the chips can be seen in fig. 4.3, along with the simulated resonance profile.

Etched Resonators

The only changes made to devices that are etched rather than lifted off is that each line only contains one resonator, with each line having one or the other frequency of resonator from the Mk 2 design.

4.2 Nanofabrication of devices

4.2.1 Lift-off method for device fabrication

Initially, devices were patterned using an additive fabrication process referred to as a bilayer liftoff; this process to create on-chip devices with deposited metal, which is briefly described by a cartoon in fig. 4.4.

The reason a bilayer is chosen as opposed to a single layer resist is due to the ability to undercut the resist. When metal is evaporated, it is deposited in a semi-directional manner. Were a single layer of resist used, there would be a bridge of metal connecting the trace intended to stay on the substrate, and the layer on the resist intended to be removed; attempting to perform lift-off would then tear the metal layer, ruining devices.

With the undercut resist the metal is deposited from "above", and therefore cannot be deposited in the "shadow" of the undercut. This allows for the deposited film to be wholly unattached to the metal on the resist, allowing for easy removal.

Silicon wafers were first diced into square chips. Then they were cleaned in an acetone dip, where the chip was agitated to remove any organic contaminants. This was followed by an isopropanol (IPA) dip and then air-dried using compressed nitrogen gas

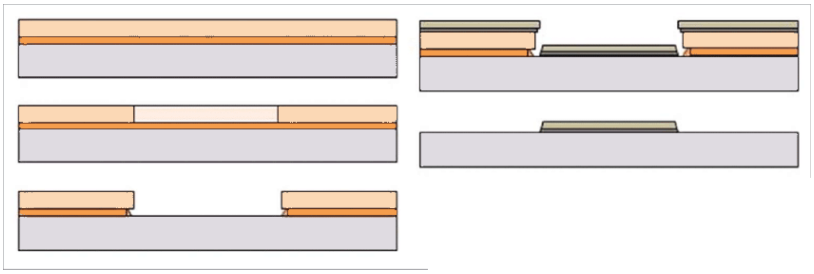

Figure 4.4: A cartoon of a bilayer lift-off. First, a soluble lower layer is spun onto the chip, then a positive tone photoresist is spun over top. At this point, the top photoresist is exposed, then developed to remove the upper layer of the photoresist where it has been exposed. Then the soluble lower layer is dissolved to create an undercut, and metal is deposited. Then when the bilayer is dissolved, the pattern is left behind in metal.

(N_2). Chips were then submerged within a piranha ($3H_2SO_4 : 1H_2O_2$) bath for ten minutes to remove any remaining organic contaminants. Chips were then treated with a bake step at 150°C, followed by gas-phase hexamethyldisilazane (HMDS) treatment which gives the chip a hydrophobic surface and improves photoresist adhesion.

At this point, chips are spin-coated with two photoresists as follows: LOR 5B is applied to the chip and is spun for ten seconds at 500 RPM to coat the chip, at which point it is spun for 45 seconds at 5000 RPM which should give a final thickness of 375 nm. Then the chip is baked at 150°C for five minutes. The chip is then coated with AZ1512 photoresist where it is spun for ten seconds at 500 RPM, followed by 45 seconds at 5000 RPM, resulting in a final thickness of 1.1 μm, and baked at 100° C for 90 seconds. The recipe and process was taken from the nanoFAB SOP[66]. These spin rates were verified using the Filmetrics Thickness Monitor (F10-VC), with the experimental data shown in fig. 4.5.

Chips are then exposed using the Heidelberg MLA150 maskless aligner. In areas of the chip that will be coated in aluminum during the final design are exposed to 405 nm blue light with a dose of 160 mJ/cm^2. While the nanoFAB recommends a dose of 120 mJ/cm^2 it was found that this led to consistent underexposure.

The areas of the AZ1512 which have been exposed are then soluble in a photoresist

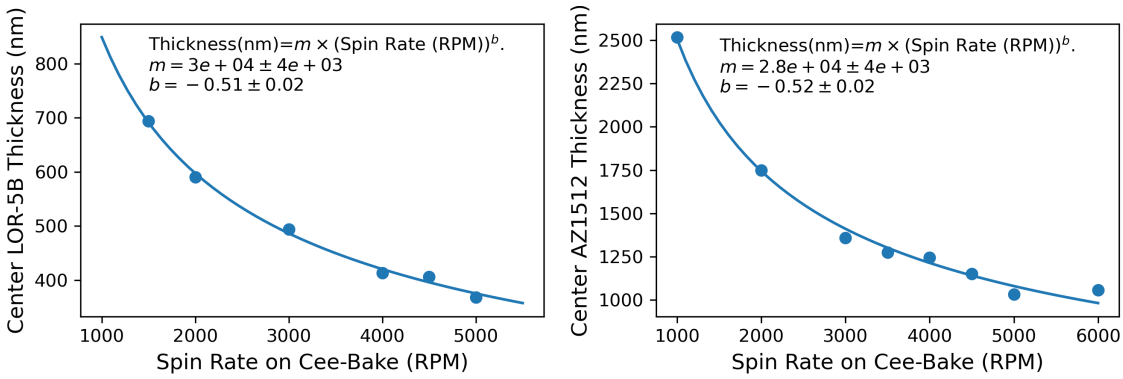

Figure 4.5: Spin curve for both LOR-5B and AZ1512 optical photoresists.

developer, such as AZ Dev 1:1. To clear the AZ1512 resist layer we then immerse them in AZ Dev 1:1 developer for 90 seconds, followed by a 60 second immersion in a dilute 1:1 solution of H_2O:MF-319 developer which clears and undercuts the LOR 5B layer allowing access to the substrate beneath.

While it is possible to use undiluted MF-319, which is the recommended application in the nanoFAB SOP, this was not found to be practical. The recommended development time for the undiluted developer was six seconds, and any small variation would result in large variations in undercut depth. This led any development involving small features (≈ 1 μm) to become unreliable. A 1:1 dilution with deionized water caused a tenfold reduction in development speed, allowing for a more reproducible minute development time.

Commonly experienced underexposure may have been due to the underlying layer of LOR-5B, but I did not conclusively determine its root cause. Examples of the effect of underdevelopment can be seen in fig. 4.6. The vertical striping and rough metal edges apparent above the meandering microstrip device are areas in which the metal lifted off where it was not intended, because of thin amounts of resist residue present in these areas that did not completely develop away. The characteristic stripe pattern is a result of the Heidelberg MLA150 raster scanning the area during exposure; areas at the sides of the scan tend to be slightly underexposed compared to the center of the scan area. Increasing the dose during exposure eliminates this resist residue, as

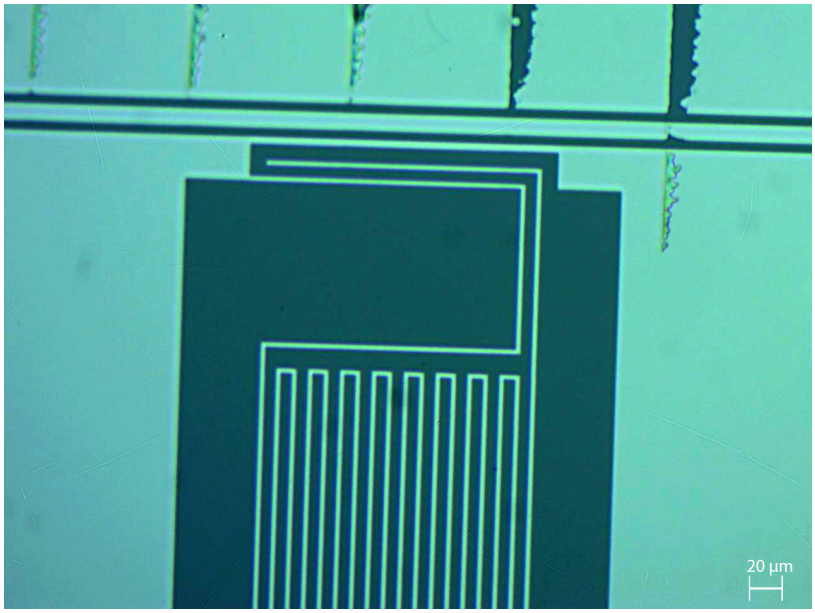

Figure 4.6: Optical microscope image of a patterned aluminum device that was underexposed during development.

all intended portions of the resist film receive a dose necessary to clear them during the develop time.

The chips are then taken to a load-lock chamber of the electron beam evaporator PVD-750 and pumped into low-vacuum (10^{-8} Torr) before an electron beam evaporates aluminum to deposit an aluminum thin film. The film is deposited at 4 Å/s to a total thickness of 150 nm. At this point chips are immersed in PG Remover to remove the remaining resist, leaving behind only the patterned sections of aluminum. While many resources tend to recommend sonication in PG remover, after repeated failed fabrication runs[1] we adopted a gentler liftoff. Chips were left suspended face-down in a PG remover bath overnight and then rinsed in acetone and IPA the following morning. During sonication it is suspected that the pieces of aluminum already lifted off contacted the surfaces remaining, abrading and sticking to them rendering the devices unusable.

[1]This is due in part to a lack of a commonly used "adhesion layer" of metal beneath the aluminum. While in most non-superconducting applications a layer of a metal that bonds more strongly to silicon such as titanium is used below a layer of aluminum, this layer would not superconduct and would therefore greatly reduce microwave quality factors.

4.2.2 Etching method of device fabrication

The quality factor of superconducting resonators is often caused by defects or contamination at the substrate-metal interface [67, 68]. Often this takes place as organic contamination due to remnant resist in lift-off processes, or in two-level system (TLS) defects caused by oxides and imperfections in the substrate where it is exposed to air. Both of these problems can be addressed by heavy surface cleaning, and surface engineering [54, 57]. In this case, we chose to use the same cleaning process as for lift-off (acetone, IPA, and piranha) with the addition of RCA-SC1 cleaning and a Hydrofluoric Acid (HF) dip in a Buffered Oxide Etch(BOE). The RCA-SC1 clean consists of a bath of NH_4OH:H_2O_2:$5H_2O$, at 75 °C. The chip is then immediately submerged in a bath of BOE containing 1% HF. Afterward, the wafers are dried with nitrogen gas and placed in the load lock of the deposition chamber within ten minutes to prevent the buildup of oxides on the surface.

The initial RCA clean serves two primary purposes. The peroxide removes traces of organic contaminants, and the ammonia serves to remove particles, modifying the surface to remove zeta potentials [69]. This leaves behind a clean silicon dioxide layer, though it cannot remove metallic contamination present. Then the BOE strips this formed oxide layer, leaving behind a bare silicon surface. However, if any metallic contaminants are present this will lead to immediate contamination of the silicon layer [70].

Unfortunately, the glassware present within the nanoFAB is not free of metallic contamination. Thus when performing the cleaning, it is very possible that the surface was contaminated, which would cause an unknown degree of loss at substrate interfaces. As this was brought to our attention very late into the development process, all etched devices were likely subject to this contamination as it was considered too time-consuming to purchase the new glassware and plastic containers necessary for

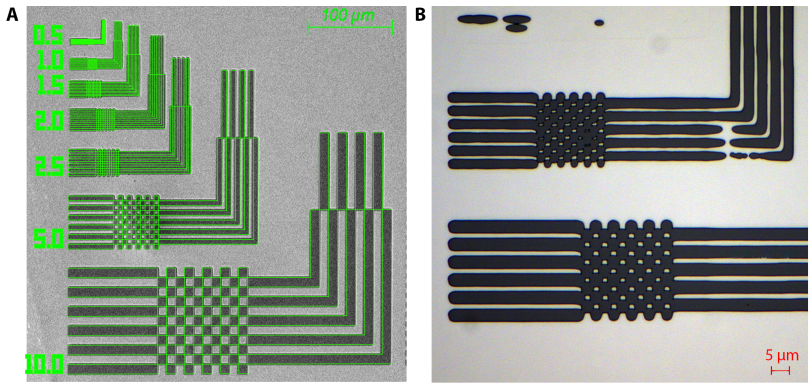

Figure 4.7: A: SEM image of resolution test post-development, with an overlay of resolution test outline.
B: Optical image showing overetching due to lack of bias with distortion due to etching anisotropy.

the process.

In ideal circumstances, the HF dip removes native oxides which act as TLS defects [54], and immediately coating the surface in aluminum prevents new oxides from forming. Aluminum's self-limiting oxide process ensures that exposure of the aluminum to air isn't problematic.

At this point in development, a protective sacrificial resist is applied and the chips are diced, while the aluminum oxide layer and aluminum coating prevent further contamination of the underlying silicon substrate surface. The sacrificial resist is then dissolved, and the chips are shelf-stable and storable for future development.

At this point, only a single layer of photoresist needs to be applied to the chip, with the only limitation on thickness being selectivity of the etch; in the case of all etches used here, the standard 1.1 μm thickness of AZ1512 is appropriate. The resist is then baked for a reduced time (60 s) due to better thermal conduction with the chip and is ready to be patterned.

The resist is again patterned using an increased 160 mJ/cm^2 dose, though due to the etches having a multidirectional etch profile a bias to the pattern is suggested to avoid over-etching. The bias can be determined through the use of a resist testing pattern such as that shown in fig. 4.7. For features of this size, a universal and isotropic

shrinking of the pattern by the bias is sufficient.

After a proper tuning of the bias necessary to control for horizontal over-etch so that dimensions are fabricated as intended, which is consistent for a given film thickness and etch time, devices can be made repeatably.

Etch based subtractive manufacturing has an additional benefit at future points in the process; as all features are etched away from a single layer of aluminum, mechanical elements can be taller (as tall as the main device) and can be produced without a second deposition which would lead to a lossy oxide interface between the metals of the microwave and mechanical elements [57]. Because the electric field by design is very concentrated in this region these dielectric losses would also be comparatively large.

4.2.3 Installing Chips Into the Package

In order to electrically access the on-chip resonator more must be done than simply placing the chip in the cavity. Before any other steps are taken the chip must be firmly fixed within the cavity. Any adhesive used would need to be stable to low temperatures, have low electrical conductivity, and have high thermal conductivity. These properties would aid in thermally anchoring the chip to the fridge, but prevent stray adhesive along the signal path from causing parasitic capacitances.

To this end we used a 1:1 dilution of GE varnish and Toluene; GE varnish is commonly used to secure cabling in fridges and has the required conductivities, while the toluene dilutes the varnish allowing it to flow and settle into the tight tolerances between chip and platform.

Just as it is necessary to be easy to install chips, they must be removable, else a new PCB and platform cap would be required for every chip tested. Thus as seen in the round platform, channels are milled into the base plate where the chip will be attached to allow excess varnish to flow away from the chip, and so solvent will be

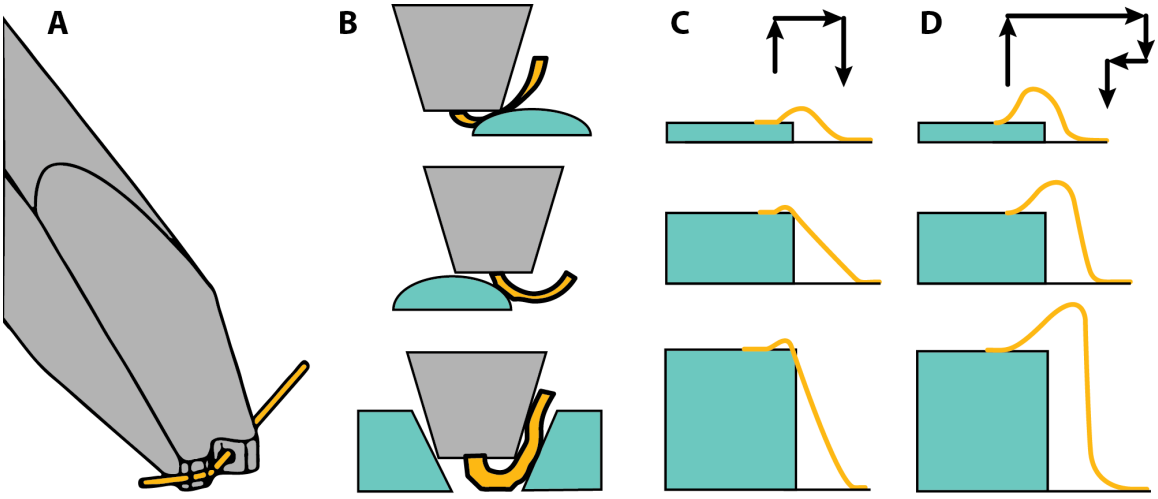

Figure 4.8: A: Schematic drawing of wedge bonding head, wire shown in gold. Width-depth of wirebonds not emphasized, ribbons 33 μm wide. B: Schematic Drawings of difficulties created by uneven bond surface. Metal bond pad shown in cyan.
C: Cartoon showing basic wire bond path, highlighting problems with uneven bond pad height.
D: Bond path implemented for any height differences greater than 100 μm to avoid contacting higher bond pad.

able to reach and dissolve the varnish. Then the base plate and PCB can simply be immersed in methanol and sonicated to remove used chips.

While this provides physical stability to the chip, it does not achieve electrical contact. This is achieved through wire-bonding the chip to the PCB. To reduce inductance, wider "ribbon" wire bonds are preferred in the RF domain as inductance scales inversely to cross-sectional conductive area [71]. The other parameter that contributes to the high impedance of wire bonds is their resistance, which can be alleviated by using superconducting wire bonds leaving only a smaller kinetic inductance contribution [71]. It is also important that wire bonds be as short as is feasible, and so packages are designed to have the chips sit flush and level with the PCB surface.

Wire-bonding in this work was performed with 33 μm wide aluminum ribbon wire-bonds installed using the new TPT HB16 Wire-bonder within the NanoFAB. There were considerable difficulties involved in developing an SOP for wire-bonding; in part due to contamination photoresist under the aluminum decreasing film adhesion, or

Material		Bond Power	Bond Force [mN]	Bond Time [ms]
Copper	Initial Bond	400	250	250
	Final Bond	425	300	275
Aluminum	Initial Bond	425	350	300
	Final Bond	450	450	300

Table 4.1: Final bonding parameters for bond pad by material.

else simply due to the complexities of the bonding process. Bonds are affixed to the surface by using a small "foot" to depress the bond onto the surface with a set force, and then vibrating ultrasonically with enough intensity to destroy oxide layers on the surface and bond, cold-welding the wire to the surface.

As one can imagine, this could be destructive to both wire and substrate and tuning of force and ultrasonic parameters is a difficult process with parameters unique to the material being bonded to. Common issues such as cratering can be difficult to diagnose, as it can be caused by bond force being either too high or too low or by excessive ultrasonic energy [72].

Parameters were eventually tuned for both the copper and aluminum bond pads, and bonding became more regular, failing only due to surface irregularities that caused an uneven bond pad surface. After finishing with a chip, wire-bond remnants must be removed from the PCB, which was performed through mechanical polishing of the affected areas.

After the chip is connected to the package, the package must then be connected to the fridge. The cavity is first secured via a screw to a mounting block with the interface being coated in Apiezon M vacuum grease, to increase thermal contact at the surface. This mounting block is then affixed to the cold plate of the fridge in the same manner, and stainless steel coaxial cable supplied by Coax Co, Ltd. connects the SMA cabling on the chosen fridge to the SMP connector on the PCB surface. The device is then ready to be cooled and measured.

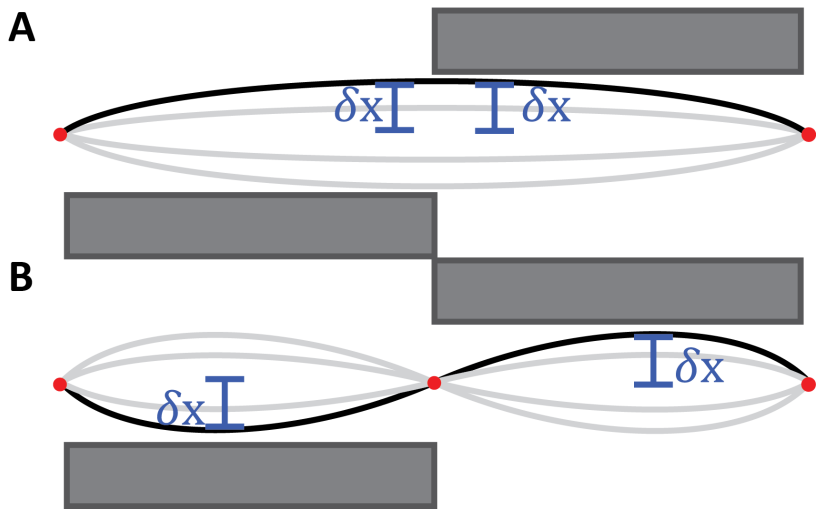

Figure 4.9: Cartoon of essential features of mechanics design. A: Fundamental mode, with equal displacement toward and away from plates, causing no first-order change in capacitance.
B: Second-harmonic mode showing the first-order change in separation, and thus capacitance.

4.3 Mechanics

While the simulation of electromechanical coupling is possible in FEM software such as COMSOL it can be difficult to implement. The high aspect ratio of the resonators compared to the thickness of deposited films along with the scale of the mechanical elements necessitating placement in areas where the electrical field is highly sensitive to perturbation make efficient simulation a nightmare.

The design of the mechanical elements was largely undertaken for the compact resonators during the forced home quarantine of the early COVID-19 pandemic. Rather than simulate the coupled mechanics and microwave resonances, the microwave resonance was modeled with and without a linear displacement, scaled by the modeshape of the deformed mechanical element. This does fail to accurately account for various phenomena in the coupled system such as backaction [73, 74] and radiation pressure shifts [75], however, it still gives a reasonable first-order approximation of the degree to which the mechanics will impact the microwave resonance.

However, rather than sensing displacement due to force as in [7] we are more in-

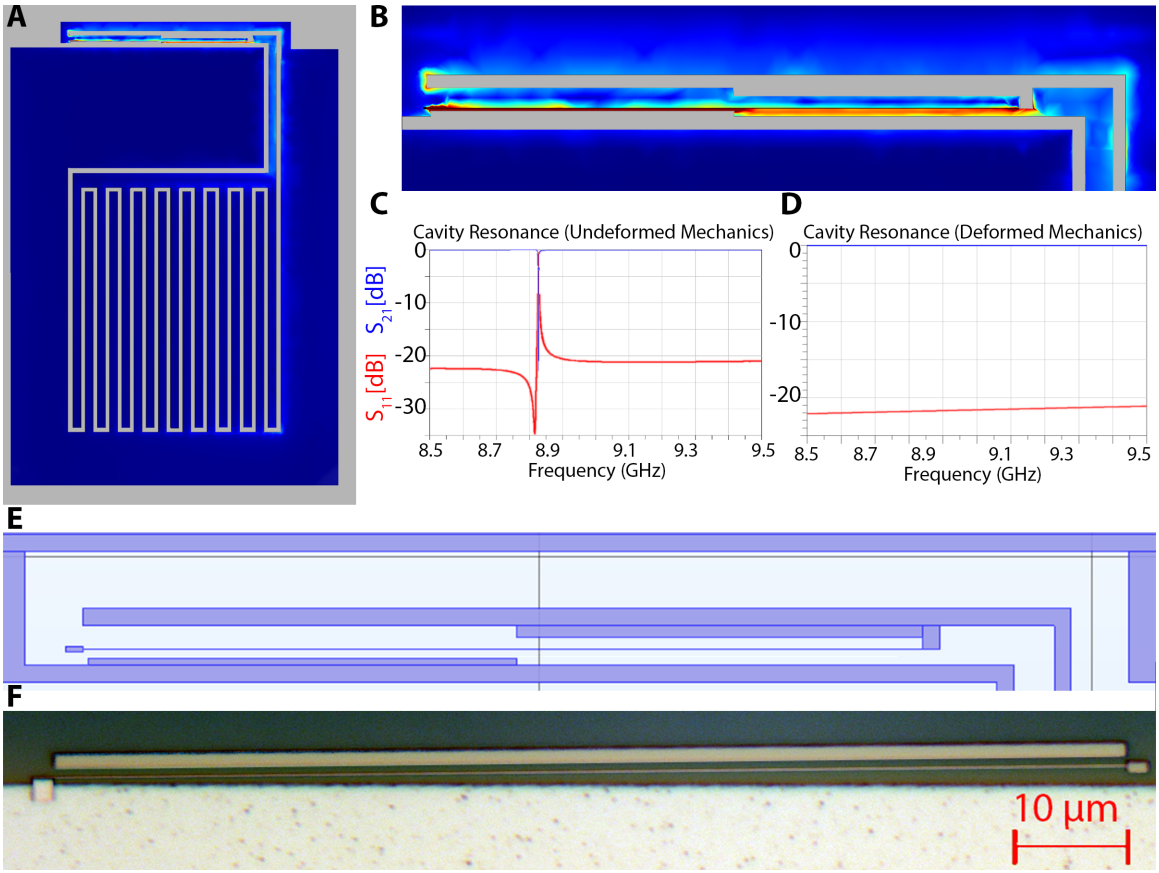

Figure 4.10: A: Cavity fundamental mode, electric field distribution.
B: Close-up of the field near mechanical element, long thin wire at E-field maximum.
C: Resonance when mechanics undeformed.
D: Resonance when mechanics deformed in modeshape of 2nd harmonic to a maximum displacement of 10 nm.
E: Schematic showing design of mechanics.
F: Image of test pattern mechanics pre-release, post-deposition and liftoff.

terested in sensing torque. Because of this the sensor must not only be sensitive to torque, but must be insensitive to linearly applied forces.With slight modifications of the mechanical elements shown in [7], namely the inclusion of aluminum blocks or pads on opposite sides of the mechanical element as seen in fig. 4.10, each block extends for half of the length of the mechanical element running alongside it at equal distance as seen in fig. 4.9. It can be seen, then, that this would provide a first order change in capacitance to ground when subjected to the motion of the second harmonic of the resonator, not the fundamental mode. With a magnetic sample deposited on a pad at the center of the string, any torque would actuate that twisting mode, while linear force would in turn couple to the fundamental mode; this makes the modified resonator a great candidate for sensing in-plane torque.

While the deformation has been exaggerated for demonstration here, the greater than 500 MHz shift from a 10 nm displacement shows the system would be highly sensitive to mechanical actuation. This toy model is insufficient to derive estimates of electromechanical coupling that could be reasonably compared to the literature, but are simply meant to provide guidance to future work. The scales and separations of devices shown here are easily fabricated using electron beam lithography, as shown in section 4.3.1. More intensive simulation of mechanics was left at this point to focus on fabrication and measurement of the microwave cavities but remains a goal for future work.

4.3.1 Fabrication of Mechanics

Test fabrication of mechanical elements was performed as an additive, lift-off process, though the focus of the project shifted to producing higher quality etched resonators before successful release and measurement of mechanics. Unlike developing a lift-off process for the newly installed Heidelberg MLA150 optical lithography system, a well-developed process for electron beam lithography at the nanoFAB was already developed [76]. After cleaning of chips using acetone and IPA (Piranha at this point

would have etched the already deposited aluminum), chips are dehydrated by baking for five minutes at 200 ° C. Then a layer of PMMA 495K, a positive tone EBL resist, is spun onto the chip at 4000 RPM resulting in a 100 nm coating, and baked at 180 ° C for ten minutes. After allowing the chip to cool for two minutes, an identical coat and bake process is done with PMMA 950K, which is less viscous than PMMA 495K, for a combined bilayer depth of ≈120 nm.

The pattern is then exposed with a dose of 10 keV for an area dose of 120 μ C/cm^2 with an aperture of 10 μm. Development is then conducted at room temperature, with a sixty-second development in MIBK:IPA 1:3, quenched for twenty seconds in an IPA bath, and rinsed in deionized water before drying with nitrogen. This leaves behind a straight to slightly undercut sidewall, suitable for evaporating up to a 60 nm thick metal layer.

After depositing a 50 nm thick aluminum layer via electron beam evaporation, the lift-off is performed by submerging the chips metal-down in an acetone bath for at least an hour, usually overnight for convenience. Mechanical elements deposited using this method are shown in fig. 4.10. The skew from straight and the placement drift are due to a lack of adequate alignment in the EBL step. Alignment marks patterned into the aluminum during the optical lithography step did not have adequate contrast to the silicon when viewed through the resist in the EBL. To resolve this issue, I would recommend an additional step where aluminum alignment marks are used in optical lithography to pattern near-field alignment marks in gold, which will be higher contrast through the resist and can be used for the alignment of mechanics.

Release of the mechanical element was attempted, using the generic isotropic silicon etch on the nanoFAB's NGP80 reactive ion etch system, but the mechanics were destroyed during the process. As focus of the project shifted to ensuring higher microwave quality factors, this was abandoned and the reasons for this not discovered. I suspect a combination of the stress in the native aluminum film destroying the beam as it was not partially annealed[7], as well as the imperfect selectivity of argon ion

etching between aluminum and silicon etching away the beam[77]. Future work will need to be done to improve masking and release before this is viable.

Chapter 5

Results: Measurement of Chips

5.1 Measurement Apparatus

5.1.1 ^{3}He Fridge Measurements

Initially, due to constraints on the availability of dilution fridges, it was decided to perform measurements of devices at low temperature on a ^{3}He refrigerator with base temperature ≈ 0.5 K. The RF wiring was comprised of coaxial cables from Coax-Co Japan connected via Pasternack Pe-034 connectors on the fridge, and with Amphenol RF SMP-MSSB-PCS connectors attaching to the package PCB. Room temperature amplification of 16 dB was used, as although cryogenic amplification doesn't suffer from the same amount of noise [78, 79], no low-temperature amplification was available on the fridges used. 20 dB of attenuation was included at the base stage of the fridge which despite not being enough to thermally anchor the coax lines still reduced power and high-temperature noise at the cavity. The inclusion of additional low-temperature attenuation caused heating issues that prevented reaching base temperature. Additional attenuation for power sweeps was included at room temperature on the output of the VNA. A diagram of the measurement setup was included in fig. 5.1

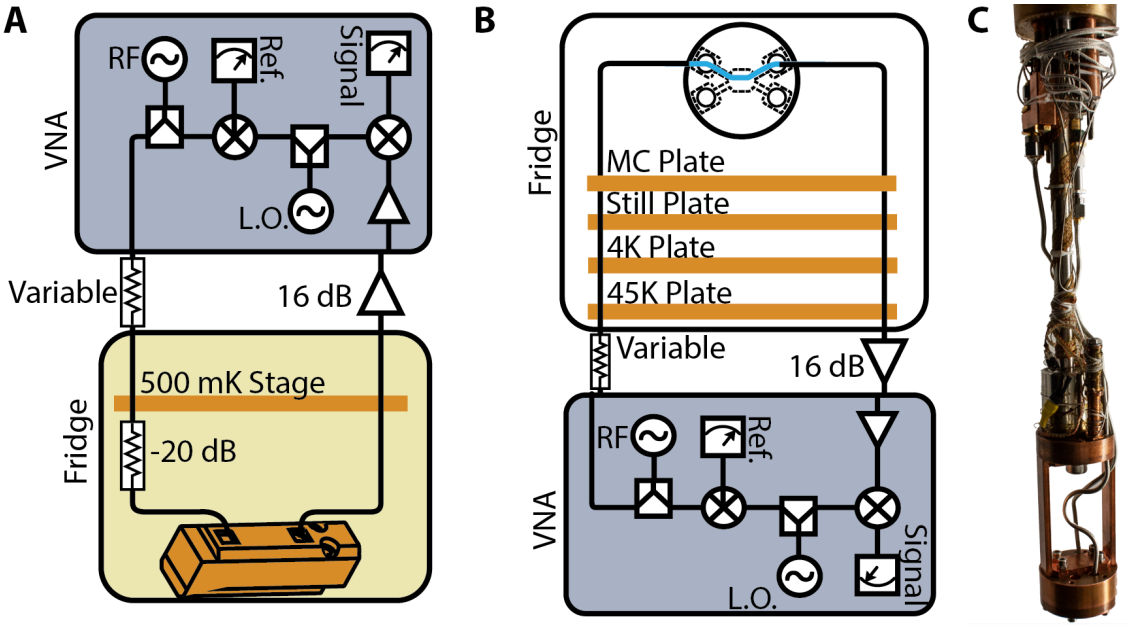

Figure 5.1: A: Diagram of measurement setup on Ice Oxford ^{3}He refrigerator on which coffin package measurements (as well as etched chip round cavity) measurements were taken.
B: Diagram of measurement setup on Davis lab designed tabletop dilution refrigerator, on which measurements of chips in the round platform were primarily taken.
C: Image of round cavity platform mounted to ^{3}He refrigerator.

5.1.2 Tabletop Dilution Refrigerator Measurements

Measurements taken on the round platform were primarily conducted on a dry (pulse tube cooled) dilution refrigerator built within the Davis lab. Stainless steel cables carry signals from room temperature to the base stage, which can reach temperatures considerably lower than the pulse tube fridge used prior. As the fridge was wired just prior to use, there was no attenuation on the input line at each stage to thermalize the signal; variable attenuation was instead added at the output of the VNA. Again, no low-temperature amplifiers were made available at the time of experiment, and 16 dB amplification was used at room temperature. A diagram of the measurement apparatus is included in fig. 5.1.

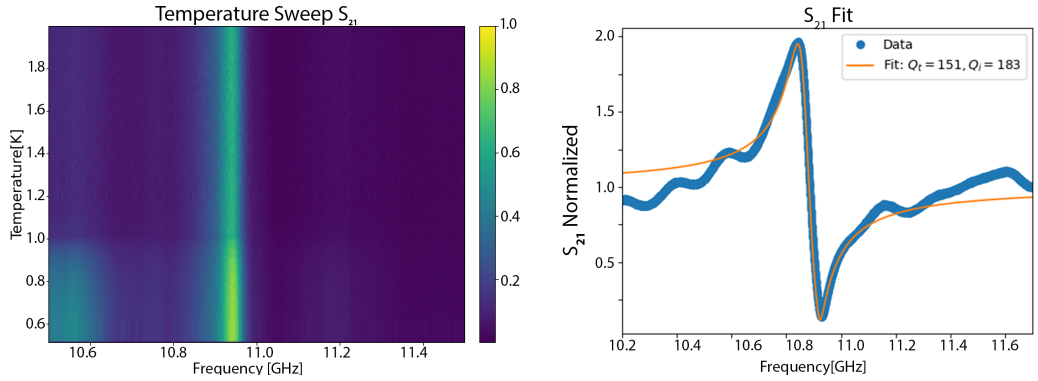

Figure 5.2: Measurements taken of early compact resonator in original coffin design.

5.2 Early Compact Resonators

Measurement of the early compact resonators was recorded across two platforms, both the original coffin style package and the revised coffin package. The measurements in the initial coffin design were less than satisfactory. With an upper limit of the quality factor of 183, there was no significant change in resonance frequency or quality as the temperature was varied above and below $T_C = 1.2$ K. Additionally, the resonance lineshape was not the characteristic "dip" of a notch coupled resonator, but rather a Fano lineshape [80]. This lineshape can arise from many electronic systems in which complexity arises from the non-trivial geometry of a resonator [81], and can be viewed as the effect of the competition between a resonant and a non-resonant scattering process [82]. Thus we assume there is a large non-resonant scattering effect lowering the quality of an already low-quality resonator.

This, combined with a lack of change in the resonator frequency or quality as it crossed the superconducting transition led me to believe that rather than seeing the resonator on-chip, we were simply exciting a parasitic resonance on the platform with the lossy FR-4 substrate obscuring the lineshape.

Combining that knowledge with the overall low transmission through the cavity, and we elected to move to the revised coffin design for further tests of the early compact resonators. At this time we also began to take SEM images of the chips, to see if

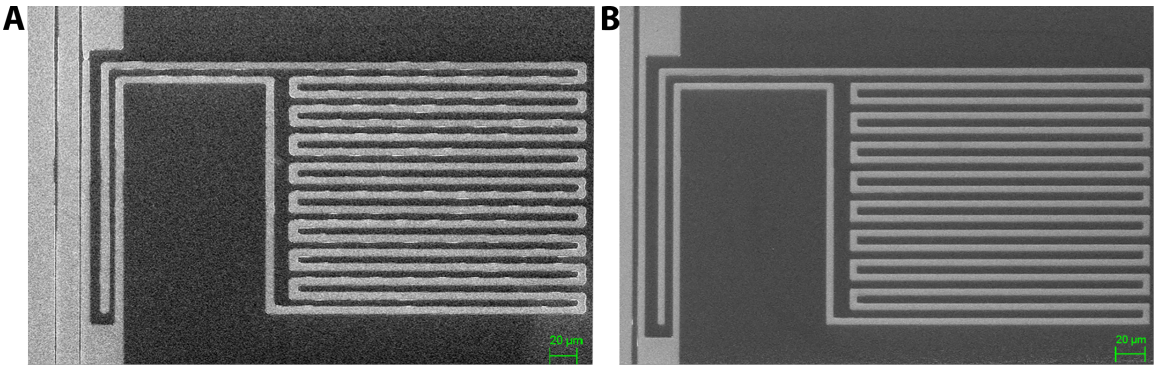

Figure 5.3: A: SEM image of the first measured device showing uneven exposure/poor liftoff quality along edges of aluminum, and inconsistent CPW width.
B: Image of the second measured device, showing improvements in line edge roughness, with widened transmission line.

there were defects that weren't obvious in optical microscopes.

Under examination in the SEM, it became obvious that thin elements in the feedline were overdeveloped, causing an over deposition (or rather, under-lifting off) of aluminum. To combat this, as mentioned in section 4.2, we began to experiment with diluting the MF-319 used to undercut the LOR-5B, which yielded better results. Transmission lines were also widened to lower sensitivity to changes in small fabrication variance.

Subsequent measurements of the early compact resonators were performed on the revised coffin platform. This led to an overall higher transmission through the cavity and easier to resolve on-chip resonances. At this point, seeking to confirm superconductivity and determine the quality of our aluminum film we probed the devices around their resonance frequency while stepping the temperature. The results of this are shown in Figure 5.4.

During future measurement runs, due to limited time during each cooldown, temperatures were only finely swept over temperatures where the resonators were superconducting. Coarse temperature sweeps were taken in both the revised coffin package and round coffin package to confirm superconducting transitions, but without enough resolution to be useful in extracting film characteristics and are included in fig. 5.5.

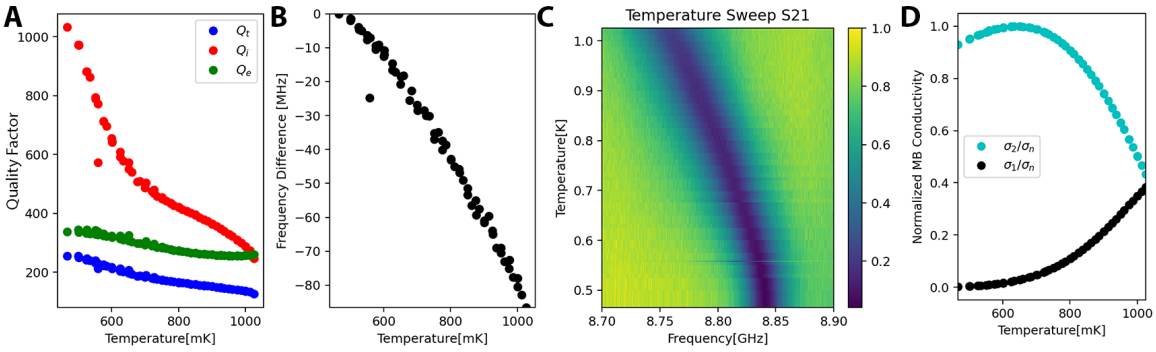

Figure 5.4: Data taken from Temperature sweep of compact resonator cavity in revised coffin platform.
A:Internal (Q_i), External(Q_e), and Total(Q_t) quality factor as temperature is swept.
B: Change in center resonance frequency as the temperature is swept.
C: Normalized data showing the behavior of resonance with changing temperature.
D: Normalized Mattis Bardeen conductivity across range of temperatures. Ratio of MB conductivity computed numerically for each resonant frequency for a given temperature.

5.3 Quarter Wavelength CPW Resonators

With the implementation of the round cavity platform as well as access to a dilution refrigerator, measurement of the quarter wavelength CPW resonators showed an immediate improvement.

5.3.1 Quarter Wavelength CPW Mk 1

The first measured chip, dubbed the "Mk. 1", as shown in fig. 5.6 had a center frequency $f_0 = 8.646$ GHz and showed quality factors in the range of $17,010$ and showed the hallmark frequency shift of superconducting aluminum. Because of the decreased transmission loss on the fridge cabling, we were also able to drive enough power into the cavity to easily force the cavity into normal conduction, also shown in fig. 5.6. The lack of agreement with the simulated $f_0 = 8.625$ GHz and $Q_i = 56,402$ is not unreasonable for resonators of this scale. It is unclear what caused the decrease in Q_i from simulation.

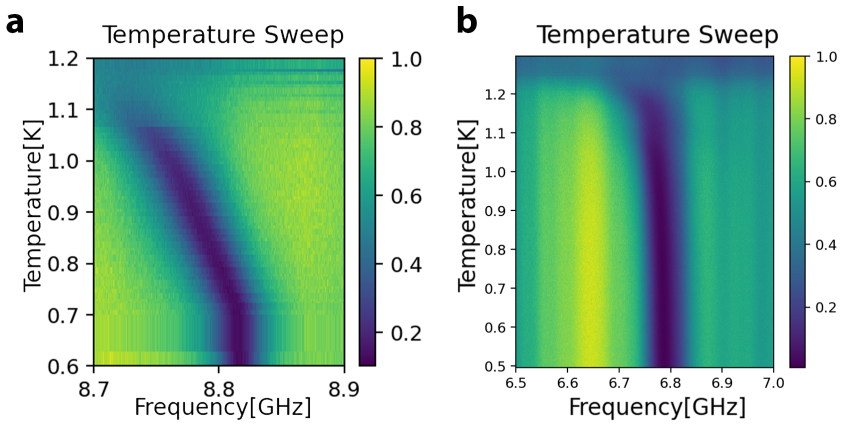

Figure 5.5: Data taken from Temperature sweeps of:
a: Mk 1 resonator on revised coffin platform.
b: Mk 2 resonator on round platform.

The doubled resonances at a slight frequency shift seen in these measurements are caused by the chip having a resonator of the same frequency on both lines, where the signal from the first CPW couples not only to the resonator along its edge but also radiatively couples to the resonator on the other line. This will be addressed more thoroughly in fits of subsequent measurements.

5.3.2 Quarter Wavelength CPW Mk 2

As discussed in section 4.1.3 the Mk. 2 chips not only had an increased resolution of curvature but also had a second, lower frequency resonator multiplexed along each transmission line. The measurement of this lower frequency resonator is shown in fig. 5.7. The devices were measured to have $f_0 = 4.581$ GHz and $Q_i = 56052$ for the higher quality resonance. The lack of agreement with the simulated $f_0 = 4.603$ GHz and $Q_i = 118445$ is within expectations for devices of this scale when fabricated. It is unclear what caused the decrease in Q_i from simulation. This generation of devices was produced using the recipes discussed in section 4.2.1.

We again see the radiative coupling between the two lines, though with the higher Q_i the picture becomes more clear. We see the lower quality resonance with greatly

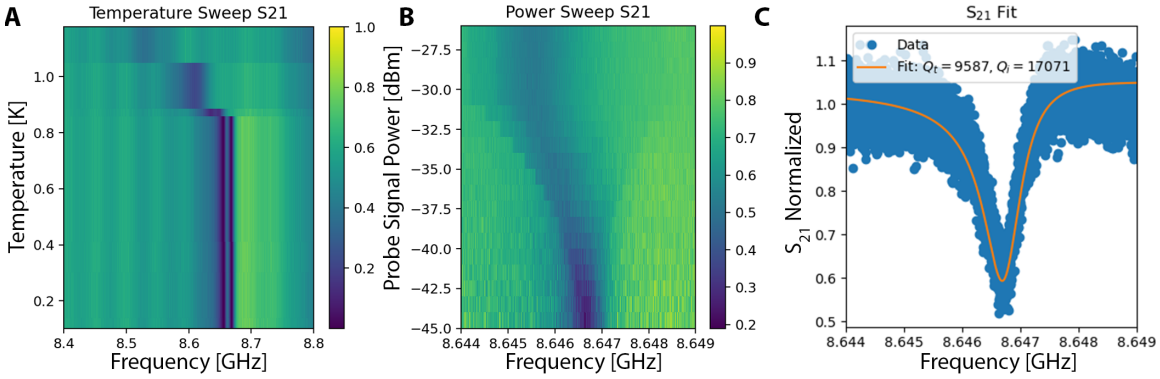

Figure 5.6: Temperature, Power sweep showing first implemented quarter-wavelength resonator on a round platform.
A: Plot of normalized S_{21} over range of temperature sweep.
B: Plot of normalized S_{21} over range of power sweep.
C: Sample of the quality factor at the lower end of the sweep, -45 dBm.

reduced Q_e take on a Fano shaped resonance, indicating a non-resonant scattering effect [82], which aligns well with the premise that it is radiatively coupling between the lines even though the round platform suppresses resonant scattering in that frequency range, as discussed in section 3.1.3. The frequency shift of the lower quality resonator is also consistent with a decreased coupling in the frequency shift predicted by eq. (2.89).

This can be further validated by examining the change in quality factor with respect to drive power these two devices exhibit, as shown in fig. 5.8. The higher quality resonance shows decreasing quality factor with a higher power, indicating a high cavity photon occupation causing heating and dielectric losses. Meanwhile, the lower quality resonance shows the inverse, a plateau at lower power with increasing Q at higher power, indicative of the "low power plateau" and then cavity photon enhancement of a resonant circuit [83, 84].

This would further support the idea that the second, lower-quality resonator is being driven through non-resonant scattering within the platform geometry.

It is interesting at this point to compare the accuracy of the simulated system to that measured here. As can be seen in fig. 5.9 we can confirm that the parameters of our

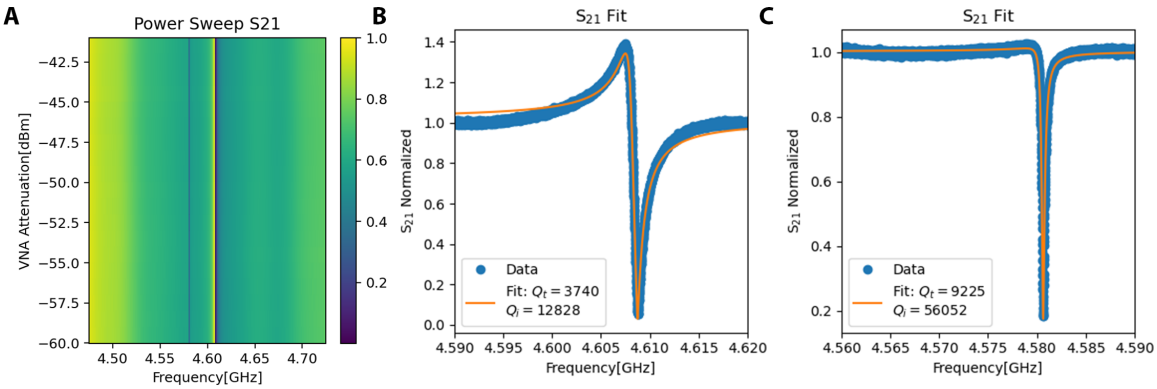

Figure 5.7: Power sweep showing variation in linewidth over drive power.
A: Power sweep for the entire range.
B: Lower quality factor resonance at -59 dBm.
C: higher quality factor resonance at -59 dBm.

	T_C [K]	London Penetration Depth [nm]	Energy Gap at $T = 0$ K
Measured	1.21 ± 0.05 K	52 ± 3 nm	3.52 kT_c *
In Literature	$1.196 \pm 0.005K$[85]	51.4 nm[33]	3.52 kT_c [33]

Table 5.1: Measure Aluminum superconducting properties compared to those found in literature. *Taken from literature, and used in fits.

film derived from the Mk 1 resonator measurements result in much more accurate simulation of on-chip modes compared to the use of perfect conductor boundaries, further justifying the model.

5.3.3 Etched Device Measurement

Due to the tabletop dilution unit being out of operation for an extended period, and subsequently given to a higher priority experiment, subsequent measurements of etched quarter wavelength CPW resonators were again performed on the ^{3}He fridge. The quality of these devices is notably lower than previous, with quality factors maxing out in the 600 range. Of note, however, is that these devices were produced with only one transmission line in the cavity, and show no signs of the "doubled" resonances, further confirming the theory of radiative coupling in prior devices. At this

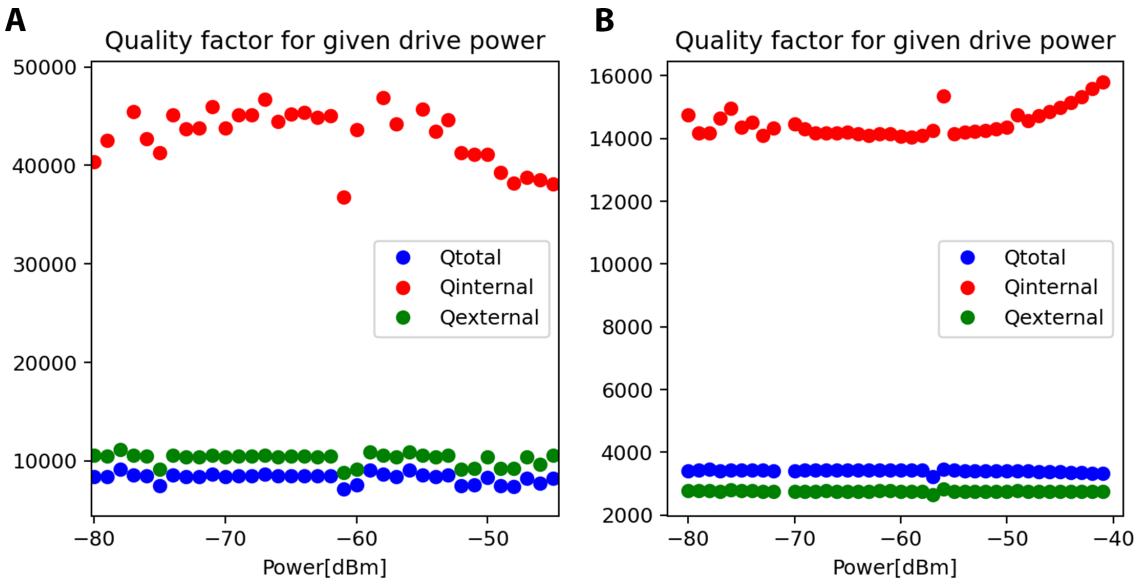

Figure 5.8: A: Quality factor as a function of drive power in the lower frequency, higher quality resonance.
B: Quality factor as a function of drive power in the higher frequency, lower quality resonance.

point, FESEM images were taken with the help of Matt Rudd to attempt to diagnose the issues, as shown in fig. 5.11.

It appears that near areas of exposed silicon have some sort of pitted texture, not visible in an optical microscope. It seems likely that some form of over-etching occurred, where the etch under-etched the resist mask, creating defects on the metal meant to remain protected during the etch.

These defects appear to have been left on all devices fabricated using the wet-etch method, so unless a different etchant is used, or the reason for the issue is uncovered, this method should not be considered viable. It is unclear why the method which has been cited as giving the highest quality factors in the literature [57] has been ineffective in this case. There may be some metal contamination present in the nanoFAB not present in their work, or it may have been some other process component.

Subsequent measurement of RIE etched devices showed no significant improvement over wet-etched devices, though there was not sufficient time to image the devices to determine if the same artefacting was present. This leads us to conclude the problem

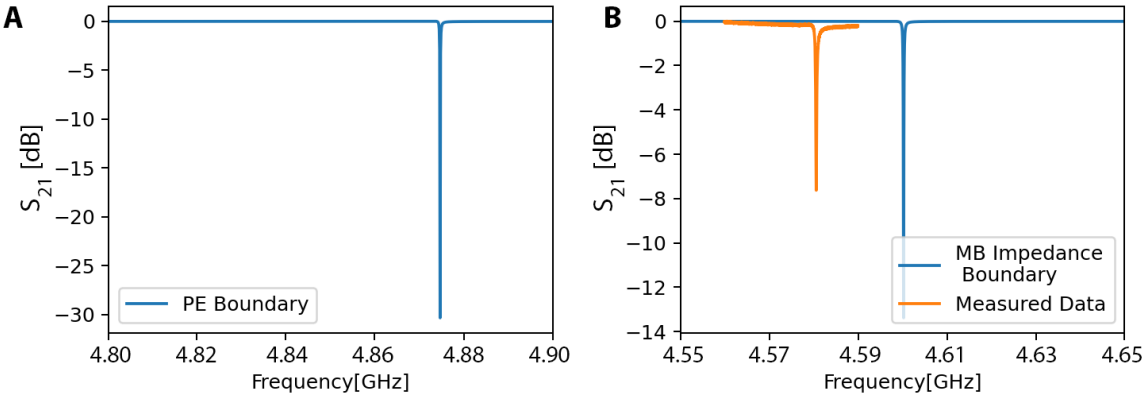

Figure 5.9: A: Simulation results using perfect electrical (PE) conductor boundary to model superconductor.
B: Simulation using surface impedance boundary condition derived from Mattis-Bardeen (MB) conductivity (as discussed in section 2.3) compared to the MK 2 resonator measurement. After solving for both parts of the complex conductivity at each frequency point used in simulation as seen in fig. 5.4, and interpolating for intermediate frequency values, the surface impedance used for the film in the simulation was set using eq. (2.115).

with these devices isn't perhaps wholly due to the etching, but also in part due to the surface treatment applied prior to deposition. While following the methods laid out in the literature, the nanoFAB has no metal contaminant-free glassware or plastic containers. While the first part of the clean (SC-1) removes zeta potentials [70] and modifies the surface it can also embed the surface with metallic contamination. During the subsequent buffered oxide etch, the chip is cleaned of its thin oxide layer some of its ionic contaminants. However, the bare silicon is highly reactive, and any metallic contamination present would have possibly recontaminated the wafer, leading to a highly lossy dielectric surface layer [69].

At the time of fabrication, it was unclear that the effect would be so deleterious, and so to save time and limit budget expenditure uncontaminated glassware was not purchased for this development step. New glassware would be essential if one wanted to re-attempt this process.

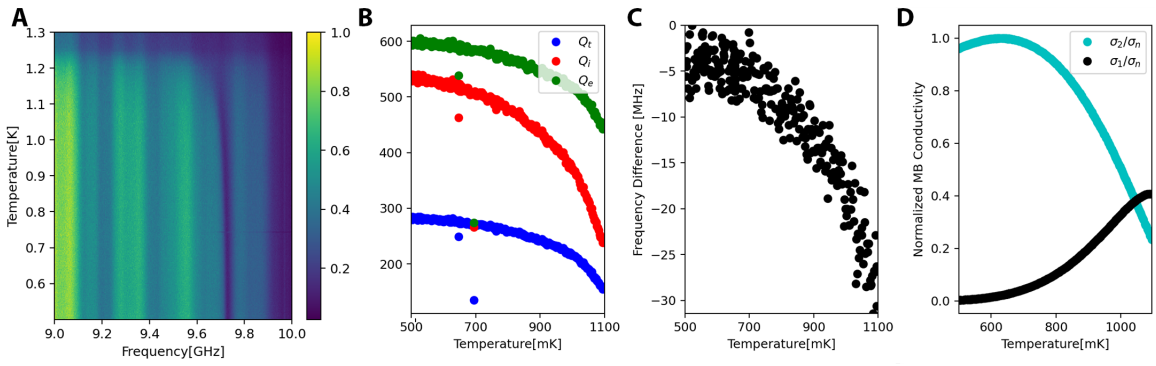

Figure 5.10: A: Temperature sweep of S_{21} measurement for measured wet-etched device.
B: Change in quality factor of wet-etched resonator across temperature range.
C: Shift in resonator frequency with temperature.

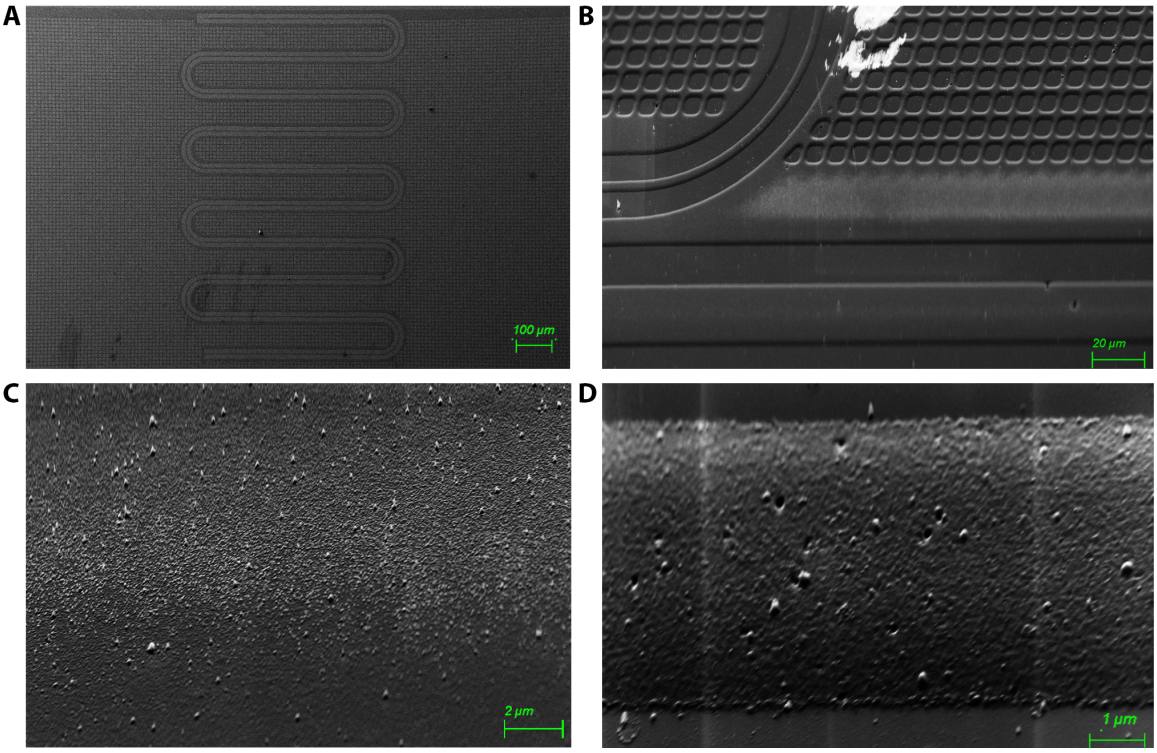

Figure 5.11: Images of a measured device created using the wet etching method. A: wide view showing meandering $\lambda/4$ resonator.
B: Artefacting along feedline boundary.
C: Close-up of artefacts, displaying texture of issue.
D: Close-up of the center pin, from 60° angle showing pitting of surface and curved profile.

Chapter 6

Conclusions, Recommendations, & Future Work

6.1 Conclusions

The primary focus of this thesis was to develop a platform for testing on-chip microwave devices at low temperatures. We succeeded in designing and building a platform capable of testing on-chip devices over a broadband (0-12 GHz) frequency range at a negligible loss. We also designed, fabricated, and measured on-chip microwave resonators with quality factors greater than 50,000. While ultimately unsuccessful in implementing a mechanical element within the microwave cavity there are straightforward methods to include those elements given additional time. The quality factors of the resonators in this work are lower than the best reported within the literature [54, 86], but are competitive with many state-of-the-art sensing platforms [87–90] and are greater than those reported in the work cited as the closest to quantum-limited electromechanical sensing [7]. Additionally, as discussed in chapter 5 we have outlined several near-term possibilities for further refinement of these devices such as acquiring uncontaminated glassware for substrate cleaning, and RIE ashing of remnant photoresist.

This work provides a platform that is easily adaptable in a turnkey fashion, along with a breadth of fabrication knowledge. Any future work within the Davis lab with on-chip electromechanics should proceed quickly and without issue.

6.2 Recommendations & Future Work

As set out in the report, further development of these devices can be accomplished through a relatively mundane assay of methods and testing.

If it is decided that fabrication through etching is too great a risk, and lift-off fabrication is pursued, quality factors could be improved via developing an RIE ashing recipe to clean remnant photoresist [91, 92] which has been shown to improve quality factors [67]. This should be performed prior to deposition, to decrease losses at the substrate-metal interface [68] as well as after lift-off.

However, it is recommended in the future that etched devices be pursued for two reasons. First, as mechanical elements will have to be deposited after the patterning of the main device there will be an oxide interface between the aluminum used to produce the elements, removal of which can cause heavy losses in areas of intense electric fields [57]. Second, while lift-off has proven easier to implement, etched devices have been shown conclusively to be capable of producing higher-quality resonators [54, 77, 86].

Future work in this direction will also have to grapple with the fabrication of mechanics. While the methods presented here show remarkable progress in fabrication, it has yet to yield a successful release. It is unclear if the beams were destroyed during release due to stresses within the aluminum or improper etch chemistry, leading to the aluminum being etched alongside silicon. While the latter will require additional testing, similar devices made in the literature have made use of a partial anneal at $\approx 300°C$ to destress the aluminum before release [7] which was not available in the nanoFAB at the time the release was conducted due to construction within the cleanroom. This would be simple to test in the future.

Bibliography

[1] K Jensen, K. Kim, and A Zettl, "An atomic-resolution nanomechanical mass sensor," *Nature nanotechnology*, vol. 3, no. 9, pp. 533–537, 2008.

[2] H. Mamin and D Rugar, "Sub-attonewton force detection at millikelvin temperatures," *Applied Physics Letters*, vol. 79, no. 20, pp. 3358–3360, 2001.

[3] G. Anetsberger, O. Arcizet, Q. P. Unterreithmeier, R. Rivière, A. Schliesser, E. M. Weig, J. P. Kotthaus, and T. J. Kippenberg, "Near-field cavity optomechanics with nanomechanical oscillators," *Nature Physics*, vol. 5, no. 12, pp. 909–914, 2009.

[4] R. G. Knobel and A. N. Cleland, "Nanometre-scale displacement sensing using a single electron transistor," *Nature*, vol. 424, no. 6946, pp. 291–293, 2003.

[5] M Poggio, M. Jura, C. Degen, M. Topinka, H. Mamin, D Goldhaber-Gordon, and D Rugar, "An off-board quantum point contact as a sensitive detector of cantilever motion," *Nature Physics*, vol. 4, no. 8, pp. 635–638, 2008.

[6] S Etaki, M Poot, I Mahboob, K Onomitsu, H Yamaguchi, and H. Van der Zant, "Motion detection of a micromechanical resonator embedded in a dc squid," *Nature Physics*, vol. 4, no. 10, pp. 785–788, 2008.

[7] G. Anetsberger, E. Gavartin, O. Arcizet, Q. P. Unterreithmeier, E. M. Weig, M. L. Gorodetsky, J. P. Kotthaus, and T. J. Kippenberg, "Measuring nanomechanical motion with an imprecision below the standard quantum limit," *Physical Review A*, vol. 82, no. 6, 2010, ISSN: 1094-1622. DOI: 10.1103/physreva.82.061804. [Online]. Available: http://dx.doi.org/10.1103/PhysRevA.82.061804.

[8] C. Ockeloen-Korppi, E. Damskägg, J.-M. Pirkkalainen, T. Heikkilä, F. Massel, and M. Sillanpää, "Noiseless quantum measurement and squeezing of microwave fields utilizing mechanical vibrations," *Physical review letters*, vol. 118, no. 10, p. 103 601, 2017.

[9] W. Heisenberg, "ber den anschaulichen inhalt der quantentheoretischen kinematik und mechanik," *W. Z. Physik*, 43:172,

[10] W. K. Heisenberg, "Uber den anschaulichen inhalt der quantentheoretischen kinematik und mechanik," *Uspekhi Fizicheskikh Nauk*, vol. 122, no. 4, pp. 651–671, 1977.

[11] J. Von Neumann, *Mathematische grundlagen der quantenmechanik*. Springer-Verlag, 2013, vol. 38.

[12] C. M. Caves, "Quantum-mechanical noise in an interferometer," *Physical Review D*, vol. 23, no. 8, p. 1693, 1981.

[13] H. Ramp, B. D. Hauer, K. C. Balram, T. J. Clark, K. Srinivasan, and J. P. Davis, "Elimination of thermomechanical noise in piezoelectric optomechanical crystals," *Phys. Rev. Lett.*, vol. 123, p. 093 603, 9 2019. DOI: 10.1103/PhysRevLett.123.093603. [Online]. Available: https://link.aps.org/doi/10.1103/PhysRevLett.123.093603.

[14] P. H.-C. Kim, *Passive and active cooling of cavity optomechanical torque sensors for magnetometry applications*. University of Alberta, 2019.

[15] C. A. Regal, J. D. Teufel, and K. W. Lehnert, *Measuring nanomechanical motion with a microwave cavity interferometer*, 2008. arXiv: 0801.1827 [quant-ph].

[16] D Vitali, P Tombesi, M. Woolley, A. Doherty, and G. Milburn, "Entangling a nanomechanical resonator and a superconducting microwave cavity," *Physical Review A*, vol. 76, no. 4, p. 042 336, 2007.

[17] H Kamerlingh Onnes, "Further experiments with liquid helium. d. on the change of electrical resistance of pure metals at very low temperatures, etc. v. the disappearance of the resistance of mercury," *Koninklijke Nederlandse Akademie van Wetenschappen Proceedings Series B Physical Sciences*, vol. 14, pp. 113–115, 1911.

[18] C. U. Lei, *Circuit Cavity Electromechanics in the Quantum Regime*. California Institute of Technology, 2017.

[19] D. Cattiaux, I. Golokolenov, S. Kumar, and et al, "A macroscopic object passively cooled into its quantum ground state of motion beyond single-mode cooling," *Nature Communications*, vol. 12, 2021. [Online]. Available: https://doi.org/10.1038/s41467-021-26457-8.

[20] W. Marshall, C. Simon, R. Penrose, and D. Bouwmeester, "Towards quantum superpositions of a mirror," *Physical Review Letters*, vol. 91, no. 13, p. 130 401, 2003.

[21] D. Pozar, *Microwave Engineering*. 2012.

[22] L. Bishop, *Circuit Quantum Electrodynamics*. Yale University, 2010.

[23] R. N. Simons, *Coplanar Waveguide Circuits, Components, and Systems*. John Wiley & Sons, Inc., 2002.

[24] G. Chione and C. U. Naldi, "Coplanar waveguides for mmic applications: Effect of upper shielding, conductor backing, finite-extent ground planes, and line-to-line coupling," *IEEE Transactions on Microwave Theory and Techniques*, vol. 3, pp. 260–267, 1987.

[25] I. Besedin and A. Menushenkov, "Quality factor of a transmission line coupled coplanar waveguide resonator," *EPJ Quantum Technol.*, vol. 5, 2018.

[26] T. K. K. Yoshida K. Watanabe and K. Enpuku, "Evaluation of magnetic penetration depth and surface-resistance of superconducting thin-films using coplanar waveguides," *IEEE Transactions On Applied Superconductivity*, vol. 5(2):1979–1982, 1995.

[27] B. A. Mazin, *Microwave kinetic inductance detectors*. California Institute of Technology, 2005.

[28] A Vayonakis and J Zmuidzinas, *Radiative losses from 2-d apertures*, 2001.

[29] M. Tinkham, "Introduction to superconductivity," 2004.

[30] J. M. Sage, V. Bolkhovsky, W. D. Oliver, B. Turek, and P. B. Welander, "Study of loss in superconducting coplanar waveguide resonators," *Journal of Applied Physics*, vol. 109, no. 6, p. 063 915, 2011. DOI: 10.1063/1.3552890. eprint: https://doi.org/10.1063/1.3552890. [Online]. Available: https://doi.org/10.1063/1.3552890.

[31] M. S. Khalil, M. J. A. Stoutimore, F. C. Wellstood, and K. D. Osborn, "An analysis method for asymmetric resonator transmission applied to superconducting devices," *Journal of Applied Physics*, vol. 111, no. 5, p. 054 510, 2012.

[32] S. Probst, F. B. Song, P. A. Bushev, A. V. Ustinov, and M. Weides, "Efficient and robust analysis of complex scattering data under noise in microwave resonators," *Scientific Instruments*, vol. 86, p. 024 706, 2015.

[33] J. Gao, *The physics of superconducting microwave resonators*. California Institute of Technology, 2008.

[34] M. Reagor, H. Paik, G. Catelani, L. Sun, C. Axline, E. Holland, I. M. Pop, N. A. Masluk, T. Brecht, L. Frunzio, and et al., "Reaching 10ms single photon lifetimes for superconducting aluminum cavities," *Applied Physics Letters*, vol. 102, no. 19, p. 192 604, 2013, ISSN: 1077-3118. DOI: 10.1063/1.4807015. [Online]. Available: http://dx.doi.org/10.1063/1.4807015.

[35] K. Geerlings, S. Shankar, E. Edwards, L. Frunzio, R. J. Schoelkopf, and M. H. Devoret, "Improving the quality factor of microwave compact resonators by optimizing their geometrical parameters," *Applied Physics Letters*, vol. 100, no. 19, p. 192 601, 2012. DOI: 10.1063/1.4710520. eprint: https://doi.org/10.1063/1.4710520. [Online]. Available: https://doi.org/10.1063/1.4710520.

[36] J. Bardeen, L. N. Cooper, and J. R. Schrieffer, "Theory of superconductivity," *Phys. Rev.*, vol. 108, pp. 1175–1204, 5 1957. DOI: 10.1103/PhysRev.108.1175. [Online]. Available: https://link.aps.org/doi/10.1103/PhysRev.108.1175.

[37] P. K. Day, H. G. LeDuc, B. A. Mazin, A. Vayonakis, and J. Zmuidzinas, "A broadband superconducting detector suitable for use in large arrays," *Nature*, vol. 425, no. 6960, pp. 817–821, 2003.

[38] J. Turneaure, J Halbritter, and H. Schwettman, "The surface impedance of superconductors and normal conductors: The mattis-bardeen theory," *Journal of Superconductivity*, vol. 4, no. 5, pp. 341–355, 1991.

[39] M. Reagor, *Superconducting Cavities for Circuit Quantum Electrodynamics*. Yale University, 2015.

[40] S. B. Nam, "Theory of electromagnetic properties of superconducting and normal systems. i," *Phys. Rev.*, vol. 156, pp. 470–486, 2 1967. DOI: 10.1103/PhysRev.156.470. [Online]. Available: https://link.aps.org/doi/10.1103/PhysRev.156.470.

[41] S. B. Nam, "Theory of electromagnetic properties of strong-coupling and impure superconductors. ii," *Phys. Rev.*, vol. 156, pp. 487–493, 2 1967. DOI: 10.1103/PhysRev.156.487. [Online]. Available: https://link.aps.org/doi/10.1103/PhysRev.156.487.

[42] M. Reagor, W. Pfaff, C. Axline, R. W. Heeres, N. Ofek, K. Sliwa, E. Holland, C. Wang, J. Blumoff, K. Chou, *et al.*, "A quantum memory with near-millisecond coherence in circuit qed," *arXiv preprint arXiv:1508.05882*, 2015.

[43] B. D. Hauer, C. Doolin, K. S. D. Beach, and J. P. Davis, "A general procedure for thermomechanical calibration of nano/micro-mechanical resonators.," *Ann. Phys.*, vol. 339, 181–207, 2013.

[44] M. Aspelmeyer, T. J. Kippenberg, and F. Marquardt, "Cavity optomechanics," *Reviews of Modern Physics*, vol. 86, no. 4, p. 1391, 2014.

[45] M. Kounalakis, Y. M. Blanter, and G. A. Steele, "Flux-mediated optomechanics with a transmon qubit in the single-photon ultrastrong-coupling regime," *Physical Review Research*, vol. 2, no. 2, p. 023 335, 2020.

[46] D. Schuster, *Circuit Quantum Electrodynamics*. Yale University.

[47] F. Sarvar, N. J. Poole, and P. A. Witting, "Pcb glass-fibre laminates: Thermal conductivity measurements and their effect on simulation," *Journal of Electronic Materials*, vol. 19, 1345–1350, 1990.

[48] D. Russell, K. Cleary, and R. Reeves, "Cryogenic probe station for on-wafer characterization of electrical devices," *Review of Scientific Instruments*, vol. 83, no. 4, p. 044 703, 2012. DOI: 10.1063/1.3700213.

[49] A. S. Averkin, K. A. Karpov, E. G. Shulga, N. Abramov, U. Huebner, E. Il'ichev, and A. V. Ustinov, "Broadband sample holder for microwave spectroscopy of superconducting qubits," *Review of Scientific Instruments*, vol. 85, 2014.

[50] F.-J. Pajares, M. Ribo, J.-R. Regue, P. Rodriguez-Cepeda, and L. Pradell, "A multimodal analysis of the effects of guard traces over near wideband signal paths," in *2005 International Symposium on Electromagnetic Compatibility, 2005. EMC 2005.*, vol. 3, 2005, 933–936 Vol. 3. DOI: 10.1109/ISEMC.2005.1513659.

[51] W. Renhart, C. Magele, and C. Tuerk, "Thin layer transition matrix description applied to the finite-element method," *IEEE Transactions on Magnetics*, vol. 45, no. 3, pp. 1638–1641, 2009. DOI: 10.1109/TMAG.2009.2012763.

[52] O. D. K. Y. Belytschko T., "A coupled finite element-element-free galerkin method," *Computational Mechanics*, vol. 17, pp. 186–195, 1995.

[53] A. D. O'Connell, M. Ansmann, R. C. Bialczak, M. Hofheinz, N. Katz, E. Lucero, C. McKenney, M. Neeley, H. Wang, E. M. Weig, A. N. Cleland, and J. M. Martinis, "Microwave dielectric loss at single photon energies and millikelvin temperatures," *Applied Physics Letters*, vol. 92, no. 11, p. 112 903, 2008. DOI: 10.1063/1.2898887. eprint: https://doi.org/10.1063/1.2898887. [Online]. Available: https://doi.org/10.1063/1.2898887.

[54] A. Megrant, C. Neill, R. Barends, B. Chiaro, Y. Chen, L. Feigl, J. Kelly, E. Lucero, M. Mariantoni, P. J. J. O'Malley, D. Sank, A. Vainsencher, J. Wenner, T. C. White, Y. Yin, J. Zhao, C. J. Palmstrøm, J. M. Martinis, and A. N. Cleland, "Planar superconducting resonators with internal quality factors above one million," *Applied Physics Letters*, vol. 100, no. 11, p. 113 510, 2012. DOI: 10.1063/1.3693409. eprint: https://doi.org/10.1063/1.3693409. [Online]. Available: https://doi.org/10.1063/1.3693409.

[55] M. S. Khalil, M. J. A. Stoutimore, F. C. Wellstood, and K. D. Osborn, "An analysis method for asymmetric resonator transmission applied to superconducting devices," *Journal of Applied Physics*, vol. 111, no. 5, p. 054 510, 2012, ISSN: 1089-7550. DOI: 10.1063/1.3692073. [Online]. Available: http://dx.doi.org/10.1063/1.3692073.

[56] M. S. Moeed, C. T. Earnest, J. H. Béjanin, A. S. Sharafeldin, and M. Mariantoni, "Improving the time stability of superconducting planar resonators," 2019. arXiv: 1905.00131 [physics.app-ph].

[57] A. Dunsworth, A. Megrant, C. Quintana, Z. Chen, R. Barends, B. Burkett, B. Foxen, Y. Chen, B. Chiaro, A. Fowler, R. Graff, E. Jeffrey, J. Kelly, E. Lucero, J. Y. Mutus, M. Neeley, C. Neill, P. Roushan, D. Sank, A. Vainsencher, J. Wenner, T. C. White, and J. M. Martinis, "Characterization and reduction of capacitive loss induced by sub-micron josephson junction fabrication in superconducting qubits," *Applied Physics Letters*, vol. 111, no. 2, p. 022 601, 2017. DOI: 10.1063/1.4993577. eprint: https://doi.org/10.1063/1.4993577. [Online]. Available: https://doi.org/10.1063/1.4993577.

[58] L. Grünhaupt, M. Spiecker, D. Gusenkova, N. Maleeva, S. T. Skacel, I. Takmakov, F. Valenti, P. Winkel, H. Rotzinger, W. Wernsdorfer, and et al., "Granular aluminium as a superconducting material for high-impedance quantum circuits," *Nature Materials*, vol. 18, no. 8, 816–819, 2019, ISSN: 1476-4660. DOI: 10.1038/s41563-019-0350-3. [Online]. Available: http://dx.doi.org/10.1038/s41563-019-0350-3.

[59] J. M. Gambetta, C. E. Murray, Y.-K.-K. Fung, D. T. McClure, O. Dial, W. Shanks, J. W. Sleight, and M. Steffen, "Investigating surface loss effects in superconducting transmon qubits," *IEEE Transactions on Applied Superconductivity*, vol. 27, no. 1, 1–5, 2017, ISSN: 1558-2515. DOI: 10.1109/tasc.2016.2629670. [Online]. Available: http://dx.doi.org/10.1109/TASC.2016.2629670.

[60] M. Jerger, S. Poletto, P. Macha, U. Hübner, E. Il'ichev, and A. V. Ustinov, "Frequency division multiplexing readout and simultaneous manipulation of an array of flux qubits," *Applied Physics Letters*, vol. 101, no. 4, p. 042 604, 2012. DOI: 10.1063/1.4739454. eprint: https://doi.org/10.1063/1.4739454. [Online]. Available: https://doi.org/10.1063/1.4739454.

[61] D Bothner, M Knufinke, H Hattermann, R Wölbing, B Ferdinand, P Weiss, S Bernon, J Fortágh, D Koelle, and R Kleiner, "Inductively coupled superconducting half wavelength resonators as persistent current traps for ultracold atoms," *New Journal of Physics*, vol. 15, no. 9, p. 093 024, 2013, ISSN: 1367-2630. DOI: 10.1088/1367-2630/15/9/093024. [Online]. Available: http://dx.doi.org/10.1088/1367-2630/15/9/093024.

[62] M. Göppl, A. Fragner, M. Baur, R. Bianchetti, S. Filipp, J. M. Fink, P. J. Leek, G. Puebla, L. Steffen, and A. Wallraff, "Coplanar waveguide resonators for circuit quantum electrodynamics," *Journal of Applied Physics*, vol. 104, no. 11, p. 113 904, 2008, ISSN: 1089-7550. DOI: 10.1063/1.3010859. [Online]. Available: http://dx.doi.org/10.1063/1.3010859.

[63] Ansys, *Advanced meshing techniques*. [Online]. Available: http://www.ece.uprm.edu/~rafaelr/inel6068/HFSS/3570_Advanced_Meshing_Techniques.pdf.

[64] A. Inc., *Ansys hfss shell element*. [Online]. Available: http://www.peraglobal.com/upload/contents/2017/06/20170609112427_69306.pdf.

[65] *Pardiso*. [Online]. Available: https://pardiso-project.org/.

[66] A. Hryciw, *Lor 5b / az 1512 bilayer procedure*. [Online]. Available: https://confluence.nanofab.ualberta.ca/pages/viewpage.action?pageId=16812125.

[67] C. Quintana, A Megrant, Z Chen, A Dunsworth, B Chiaro, R Barends, B Campbell, Y. Chen, I.-C. Hoi, E Jeffrey, *et al.*, "Characterization and reduction of microfabrication-induced decoherence in superconducting quantum circuits," *Applied Physics Letters*, vol. 105, no. 6, p. 062 601, 2014.

[68] X. Zhang, L. Du, Y. Zhu, and C. Liu, "Investigation of adhesion properties between su-8 photoresist and stainless steel substrate," *Micro & Nano Letters*, vol. 6, no. 6, pp. 397–401, 2011.

[69] W. Kern, "The evolution of silicon wafer cleaning technology," *Journal of the Electrochemical Society*, vol. 137, no. 6, p. 1887, 1990.

[70] M. Itano, F. W. Kern, M. Miyashita, and T. Ohmi, "Particle removal from silicon wafer surface in wet cleaning process," *IEEE Transactions on semiconductor manufacturing*, vol. 6, no. 3, pp. 258–267, 1993.

[71] Y. Lin, C. Peng, and K. Chiang, "Parametric design and reliability analysis of wire interconnect technology wafer level packaging," *J. Electron. Packag.*, vol. 124, no. 3, pp. 234–239, 2002.

[72] W. Van Driel, J. Janssen, R. Van Silfhout, M. Van Gils, G. Zhang, and L. Ernst, "On wire failures in micro-electronic packages," in *5th International Conference on Thermal and Mechanical Simulation and Experiments in Micro-electronics and Microsystems, 2004. EuroSimE 2004. Proceedings of the*, IEEE, 2004, pp. 53–57.

[73] B. D. Hauer, T. J. Clark, P. H. Kim, C. Doolin, and J. P. Davis, "Dueling dynamical backaction in a cryogenic optomechanical cavity," *Physical Review A*, vol. 99, no. 5, p. 053 803, 2019.

[74] A. A. Clerk, F. Marquardt, and K Jacobs, "Back-action evasion and squeezing of a mechanical resonator using a cavity detector," *New Journal of Physics*, vol. 10, no. 9, p. 095 010, 2008.

[75] I Wilson-Rae, N Nooshi, J. Dobrindt, T. J. Kippenberg, and W Zwerger, "Cavity-assisted backaction cooling of mechanical resonators," *New Journal of Physics*, vol. 10, no. 9, p. 095 007, 2008.

[76] M. Mohammad, C. Guthy, S Evoy, S. Dew, and M Stepanova, "Nanomachining and clamping point optimization of silicon carbon nitride resonators using low voltage electron beam lithography and cold development," *Journal of Vacuum Science & Technology B, Nanotechnology and Microelectronics: Materials, Processing, Measurement, and Phenomena*, vol. 28, no. 6, C6P36–C6P41, 2010.

[77] A Bruno, G De Lange, S Asaad, K. Van Der Enden, N. Langford, and L DiCarlo, "Reducing intrinsic loss in superconducting resonators by surface treatment and deep etching of silicon substrates," *Applied Physics Letters*, vol. 106, no. 18, p. 182 601, 2015.

[78] J. A. del Alamo and J. Joh, "Gan hemt reliability," *Microelectronics reliability*, vol. 49, no. 9-11, pp. 1200–1206, 2009.

[79] L Shen, S Heikman, B Moran, R Coffie, N.-Q. Zhang, D Buttari, I. Smorchkova, S Keller, S. DenBaars, and U. Mishra, "Algan/aln/gan high-power microwave hemt," *IEEE Electron Device Letters*, vol. 22, no. 10, pp. 457–459, 2001.

[80] S. Fan, P. R. Villeneuve, J. D. Joannopoulos, and H. A. Haus, "Channel drop tunneling through localized states," *Phys. Rev. Lett.*, vol. 80, pp. 960–963, 5 1998. DOI: 10.1103/PhysRevLett.80.960. [Online]. Available: https://link.aps.org/doi/10.1103/PhysRevLett.80.960.

[81] S. Fan, W. Suh, and J. D. Joannopoulos, "Temporal coupled-mode theory for the fano resonance in optical resonators," *J. Opt. Soc. Am. A*, vol. 20, no. 3, pp. 569–572, 2003. DOI: 10.1364/JOSAA.20.000569. [Online]. Available: http://www.osapublishing.org/josaa/abstract.cfm?URI=josaa-20-3-569.

[82] E. Kamenetskii, A. Sadreev, and A. Miroshnichenko, *Fano Resonances in Optics and Microwaves: Physics and Applications*. Springer International Publishing, 2018.

[83] A Dunsworth, A Megrant, C Quintana, Z. Chen, R Barends, B Burkett, B Foxen, Y. Chen, B Chiaro, A Fowler, *et al.*, "Characterization and reduction of capacitive loss induced by sub-micron josephson junction fabrication in superconducting qubits," *Applied Physics Letters*, vol. 111, no. 2, p. 022 601, 2017.

[84] M. S. Khalil, F. Wellstood, and K. D. Osborn, "Loss dependence on geometry and applied power in superconducting coplanar resonators," *IEEE Transactions on Applied Superconductivity*, vol. 21, no. 3, pp. 879–882, 2010.

[85] J. F. Cochran and D. E. Mapother, "Superconducting transition in aluminum," *Phys. Rev.*, vol. 111, pp. 132–142, 1 1958. DOI: 10.1103/PhysRev.111.132. [Online]. Available: https://link.aps.org/doi/10.1103/PhysRev.111.132.

[86] C. T. Earnest, J. H. Béjanin, T. G. McConkey, E. A. Peters, A. Korinek, H. Yuan, and M. Mariantoni, "Substrate surface engineering for high-quality silicon/aluminum superconducting resonators," *Superconductor Science and Technology*, vol. 31, no. 12, p. 125 013, 2018.

[87] M. Castellanos-Beltran and K. Lehnert, "Widely tunable parametric amplifier based on a superconducting quantum interference device array resonator," *Applied Physics Letters*, vol. 91, no. 8, p. 083 509, 2007.

[88] J. J. Viennot, X. Ma, and K. W. Lehnert, "Phonon-number-sensitive electromechanics," *Phys. Rev. Lett.*, vol. 121, p. 183 601, 18 2018. DOI: 10.1103/PhysRevLett.121.183601. [Online]. Available: https://link.aps.org/doi/10.1103/PhysRevLett.121.183601.

[89] L. Frunzio, A. Wallraff, D. Schuster, J. Majer, and R. Schoelkopf, "Fabrication and characterization of superconducting circuit qed devices for quantum computation," *IEEE Transactions on Applied Superconductivity*, vol. 15, no. 2, pp. 860–863, 2005. DOI: 10.1109/TASC.2005.850084.

[90] D. Bothner, S. Yanai, A. Iniguez-Rabago, M. Yuan, Y. M. Blanter, and G. A. Steele, "Cavity electromechanics with parametric mechanical driving," *Nature communications*, vol. 11, no. 1, pp. 1–9, 2020.

[91] I. M. Pop, T Fournier, T Crozes, F. Lecocq, I. Matei, B. Pannetier, O. Buisson, and W. Guichard, "Fabrication of stable and reproducible submicron tunnel junctions," *Journal of Vacuum Science & Technology B, Nanotechnology and Microelectronics: Materials, Processing, Measurement, and Phenomena*, vol. 30, no. 1, p. 010 607, 2012.

[92] P. Koppinen, L. Väistö, and I. Maasilta, "Complete stabilization and improvement of the characteristics of tunnel junctions by thermal annealing," *Applied physics letters*, vol. 90, no. 5, p. 053 503, 2007.